The Hashemite Kingdom of Jordan
Scientific Research Support Fund
The Hashemite University

JJEES

Jordan Journal of Earth and Environmental Sciences

Volume (11) Number (4)

JJEES is an International Peer-Reviewed Research Journal

ISSN 1995-6681 jjees.hu.edu.jo December 2020

Jordan Journal of Earth and Environmental Sciences (JJEES)

JJEES is an International Peer-Reviewed Research Journal, Issued by Deanship of Scientific Research, The Hashemite University, in corporation with, the Jordanian Scientific Research Support Fund, the Ministry of Higher Education and Scientific Research.

Submission address:

Manuscripts should be submitted electronically to the following e-mail:

jjees@hu.edu.jo

For more information and previous issues:

www.jjees.hu.edu.jo

Hashemite Kingdom of Jordan

Scientific Research Support Fund

Hashemite University

Jordan Journal of Earth and Environmental Sciences

JJEES

An International Peer-Reviewed Scientific Journal

Financed by the Scientific Research Support Fund

Volume 11 Number (4)

http:// jjees.hu.edu.jo/

ISSN 1995-6681

Cover page photo: Khazneh (Petra Treasury) caved in Late Cambian Umm Ishrin Formation, photographed by Traveltalk

JJEES
Jordan Journal of Earth and Environmental Sciences

PAGES	PAPERS
234 - 240	Effects of Heavy-Metal Pollution on Soil Microbial Community, Plants, and Human Health *Kheira Dahnoun and Fatima Djadouni*
241 - 247	Strain Analysis of Dana Conglomerates in Ad Dhira Area- Dead Sea *Mohammad Al-Adamat and Abdullah Diabat*
247 - 252	An Analysis of Rainfall and Discharge Relationship at the River Kilange Catchment, Adamawa State, Nigeria *Dzarma Sayd, Ezekiel Yonnana, Aishatu Mubi*
253 - 259	Geotechnical Evaluation of South Jordan Basaltic Rocks for Engineering Uses *Suhail Sharadqah, Reyad A. Al Dwairi, Mazen Amaireh, Hani Nawafleh, Omar Khashman, Aiman E. Al-Rawajfeh, Soraya M. Perez*
260 -271	Assessing the Impact of Zaatari Syrian Refugee Campin Central North Jordan on the Groundwater Quality *Sura Al-Harahsheh, Ahmed A. Al-Taani, Hani Al-Amoush, Akram Shdeifat, Atef Al-Mashagbah, Marwan Al-Raggad, Raya Al- Omoush, Hassan Al-Kazalah, Maher Hraishat, Refaat Bani-Khalaf, Khaled Almasaeid*
272 - 281	Mineralogical and Geochemical Characterization of Jarash Kaolinitic Clay, Northern Jordan *Talal Al-Momani, Mohammad Alqudah,"Mohammed-Ezz-Aldien" Dwairi*
282 - 290	Factors Affecting the Rate of Absorption of Sulfur Dioxide into Fly Ash Suspensions *Ahmad Al-Haj-Ali*
290 - 301	Geological Mapping and Gemstones prospecting in Deformed Precambrian Rocks, East of Okemesi Fold Belt, Southwestern Nigeria *Olusiji Samuel Ayodele and Isaac Ominyi Ajigo*

JJEES

JJEES (2020) 11 (3): 234-240
ISSN 1995-6681

Jordan Journal of Earth and Environmental Sciences

Effects of Heavy-Metal Pollution on Soil Microbial Community, Plants, and Human Health

Kheira Dahnoun* and Fatima Djadouni

Mascara University, Faculty of Natural Sciences and Life, Department of Biology, Research Laboratory in Geoenvironment and Spatial Development, 29000 Mascara, Algeria.

Received 29 September 2019; Accepted 4 July 2020

Abstract

Heavy metals are among the most important sources of contamination in soil, and are considered among the most dangerous matters due to their toxicity, persistence, and resistance to biological degradation. They may cause serious health problems for many forms of life. Heavy metals exhibit toxic effects towards soil biota by affecting key microbial processes and decreasing the number and activity of soil microorganisms. Crops grown on contaminated soils can potentially lead to the uptake and accumulation of trace metals in the edible plant parts. The uptake of heavy metals by plants and their subsequent accumulation along the food chain pose potential threats to animal and human health.

Keywords: Heavy metals, environment, soil, plants, microorganisms, human health.

1. Introduction

In the recent years, the world has witnessed various kinds of pollution which threatens human life and over time makes many environments inhabitable (Panigrahi et al., 2019). Rapid growth of industrialization and urban population have affected the quality of soil (Bulgariu and Gavrilescu, 2015). Heavy metals are among the most important soil contaminants (Tangahu et al., 2011) due to their toxicity, persistence, resistance to biological degradation and long-term accumulation in the food chain; thus, causing serious health problems for many forms of life (Bulgariu and Gavrilescu, 2015).

Metals are present naturally at various levels in the earth's crust. The burning of fossil fuels, mining of metalliferous ores, wastes of municipal areas, and excessive use of pesticides and fertilizers lead to an accelerated release of metals and metalloids into various components of ecosystems (Kumar et al., 2016). Heavy metals are defined as metals and metalloids having densities greater than > 5 g cm-3 (Oves et al., 2016).

Soil contamination by heavy metals is one of the most formidable threats throughout the industrialized world. Heavy-metal pollution not only results in adverse effects on various parameters relating to plant quality and yield but also causes changes in the size, composition, and activity of the microbial community (Singh et al., 2011). The consumption of plants grown in contaminated areas, as well as the ingestion or inhalation of contaminated particles are two principal factors contributing to human exposure to metals (Zhuang et al., 2009). Also, the cultivation of crops for human or livestock consumption on contaminated soil can potentially lead to the uptake and accumulation of trace metals in the edible plant parts with a resulting risk to human and animal health (Zhuang et al., 2009).

Heavy metals do not all pose the same risks because of their effects on organisms, chemical, physicochemical and biological properties. Their toxicity is variable and their impact on the environment varies widely. Therefore, the objective of this paper is to discuss the effects of heavy metals on the soil, plants and human health.

2. Heavy Metals' Origins

Heavy metals (HM) are naturally present in earth crust and rocks in the form of sulphides and oxide ores such as sulphides of lead, iron, mercury, cadmium, arsenic or cobalt (Verma and Kaur, 2016).

HM in the environment can vary across different regions resulting in spatial variations of background concentrations. The distribution of metals in the environment is governed by the properties of the metal and influences of environmental factors (Morais et al., 2012). HM and their compounds are characterized by relatively high stability, solubility in atmospheric precipitation, and the ability to be absorbed by soil and plants. They are accumulated in organisms, and are toxic in any state for humans and animals with a wide spectrum and variety of harmful effects (Dzyadevych and Jaffrezic-Renault, 2014). HM occur naturally in the soil environment from the pedogenetic processes of the weathering of parent materials at levels that are trace (<1000 mg kg^{-1}) and are rarely toxic (Wuana and Okieimen, 2011).

Natural sources of HM such as volcanic emissions, transport of continental dusts, and weathering of metal-enriched rocks due to long exposure to air, greatly add higher amounts of HM to soils (Oves et al., 2016). However, the major source of contamination is of anthropogenic origin (Table 1); such human activities responsible for the increase of metal flows are: the exploitation of mines and smelters,

* Corresponding author e-mail: kheira.dahnoun@univ-mascara.dz

the application of metal-based pesticides and metal-enriched sewage sludge in agriculture, the combustion of fossil fuel, metallurgical industries, and electronics, and military training and weapons (Oves et al., 2016; Villanneau et al., 2008).

Table 1. Anthropogenic sources and usage of heavy metals, through which they can be introduced into the environment (Bradl, 2005).

Metal	Sources
Arsenic (As)	Additive to animal feed, wood preservative, ceramics, pesticides, electronic components, metallurgy, textile, pigments.
Beryllium (Be)	Electrical insulators in power transistors, moderator or neutron deflectors in nuclear reactors.
Cadmium (Cd)	Ni/Cd batteries, pigments, anti-corrosive metal coatings, plastic stabilizers, alloys, coal combustion.
Cobalt (Co)	Metallurgy, ceramics, glasses, paints.
Chromium (Cr)	Manufacturing of ferro-alloys, plating, pigments, textile, passivation of corrosion of cooling circuits, wood treatment.
Copper (Cu)	Good conductor of heat and electricity, water pipes, roofing, kitchenware, chemicals and pharmaceutical equipment, pigments, alloys.
Iron (Fe)	Cast iron, wrought iron, steel, alloys, construction, transportation, machine manufacturing.
Mercury (Hg)	Extracting of metals by amalgamation, electrical and measuring apparatus, fungicides, catalysts, pharmaceuticals, dental fillings, scientific instruments.
Nickel (Ni)	As an alloy in the stell industry,arc-welding, rods, pigments for paints and ceramics, surgical and dental prostheses, computer components, catalysts.
Lead (Pb)	Antiknock agents, lead-acid batteries, pigments, glassware, ceramics, plastic, in alloys, sheets, cable sheathings, solder, pipes or tubing.
Titanium (Ti)	For white pigments (TiO2), as a UV-filtering agents (sun cream), nucleation Agent for glass ceramics, as Ti alloy in aeronautics.
Zinc (Zn)	Zinc alloys (bronze, brass), anti-corrosion coating, batteries, cans, in medicines and chemicals, rubber industry, paints, soldering and welding fluxes.

High concentrations of heavy metals have deleterious effects on the environment (Mustapha and Halimoon, 2015). They cannot be destroyed biologically, but can be accumulated in living organisms, and their toxicity can last for a long time in nature. Some HM, such as mercury, can even be transformed from relevant low toxic species into more toxic forms in a certain environment (Alkorta et al., 2004) and cause various diseases and disorders even at relatively lower concentrations (Tangahu et al., 2011).

3. Heavy Metals effects

3.1 Aquatic Environment

In natural aquatic ecosystems, metals occur in low concentrations, normally at the nanogram to microgram per liter level. Recently, the occurrence of metal contaminant, especially the heavy metals in excess of natural loads, has become a problem raising increasing concerns (Biney et al., 1994).

Anthropogenic inputs, geochemical structure, and the mining of metals create potential sources of heavy-metal pollution in the aquatic environment. Heavy metals are natural constituents of rocks and soils and can enter the environment because of weathering and erosion (Yahya et al., 2018). The agricultural sector also contributes to contamination through some wastes containing metals. For example, Cu from piggery wastes has been correlated to contamination of sediments and molluscs (Shazili et al., 2006).

Through toxicity and accumulation in the environment, HM discharged into the marine environment can impact species diversity as well as entire marine ecosystems (Gu et al., 2015). Among animal species, fishes are the inhabitants that cannot escape from the detrimental effects of these pollutants. Directly acting or synergistically acting metals such as Fe, Zn, Pb, Cd, Cu, and Mn are common toxic pollutants for fish (Joseph et al., 2010).

In biological systems, HM have been reported to affect cellular organelles and components such as cell membrane, mitochondrial, lysosome, endoplasmic reticulum, nuclei, and some enzymes involved in metabolism, detoxification, and damage repair at the cellular level (Yahya et al., 2018).

3.2 Soil Microbial Dynamic

Metals play an integral role in the life processes of microorganisms. Some metals, such as Ca, Co, Cr, Cu, Fe, K, Mg, Mn, Na, Ni, and Zn are required nutrients and are essential. Others have no biological role (Ag, Al, Cd, Au, Pb, and Hg) and are nonessential (Bruins et al., 2000). However, heavy metals' excess causes morphological and physiological changes, and affects the reproduction of microorganism (Scott-Fordsmand, 1997).

The effects of HM on microorganisms have been studied at several levels of experimental complexity. Such studies have determined the concentrations of HM that reduce or completely inhibit the growth of microbes in synthetic media and, to a lesser extent, in samples from natural environments (Babich and Stotzky, 1983) that affect the respiratory activity and the enzymatic machinery of soil organisms (Moreno et al., 2003; Singh and Kalamdhad, 2011). The mode of action of heavy metals varies from one enzyme to another, and the effects on enzymes depend on the type of heavy metal and their concentration (Moreno et al., 2003). Moreover,

members of the same species in the microbial community would show considerable differences in their sensitivity to metal toxicity (Gillera et al., 1998). Metals either act on the cell membrane or interfere with cytoplasmic or nuclear functions after entry into the cell (Madoni, 2000) (Figure 1).

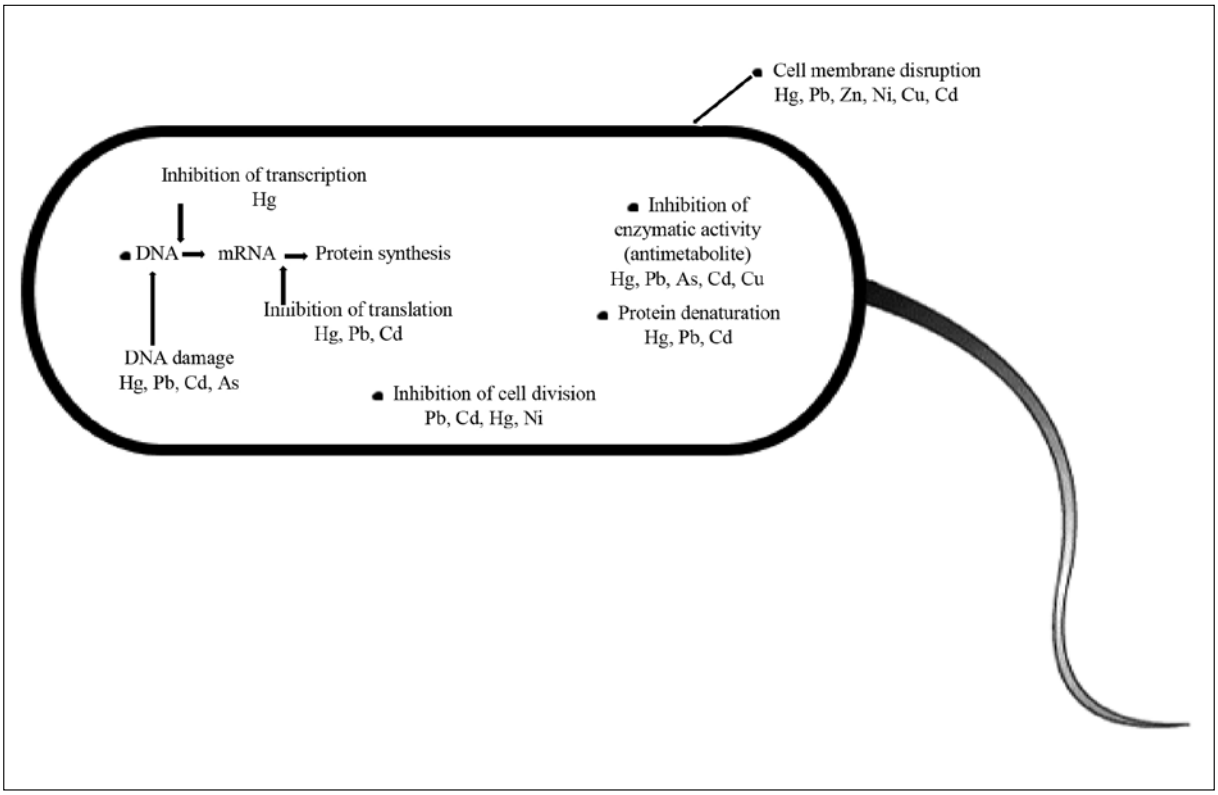

Figure 1. Various toxic influences of metals on the microbial cell. Adapted from Timberley et al. (2015).

For example, Ni is proposed to affect cell surface membranes, DNA replication, transcription, and translation, as well as other metabolic activities, including photosynthesis, nitrogen fixation, respiration, and fermentation (Babich and Stotzky, 1983). Excess of Ni causes a perturbation of protein function and is toxic for eukaryotic cells and bacteria (Lusi et al., 2017). Similarly, Cd toxicity can be identified by a number of cellular effects that include growth inhibition, enzyme inactivation, proteins and DNA oxidation, nucleotide conformation changes, and ultrastructural changes that can cause cell-membrane damage and destroy the transport of nutrients (Scott-Fordsmand, 1997). Furthermore, it is reported that copper oxide sorption on biomass is strong and rapid, which in turn caused a rapid loss of membrane integrity (Wang et al., 2010).

At the level of the fauna, these effects can be manifested by a loss of weight, an inhibition of the growth, an appearance of behavioural or physiological disorders at all reproduction stages. At the level of the ecosystem, heavy metals can generate loss of diversity, loss of biological activity (decomposition, mineralization, aeration of the soil) and change in the structure of the specific community (Forneris, 2002).

3.3 Plants

In many parts of the world, agricultural soils are slightly to moderately contaminated by heavy-metal toxicity and have become a critical environmental concern due to their potential adverse ecological effects. Such toxic elements are considered as soil pollutants due to their widespread occurrence, and their acute and chronic toxic effect on plants grown of such soils (Yadav, 2010).

HM are available to plants through mining activities (smelting, river dredging, mine spoils and tailings, and metal industries), industries (plastics, textiles, microelectronics, wood preservatives, and refineries), atmospheric deposition (urban refuse disposal, pyrometallurgical industries, automobile exhausts, and fossil fuel combustion), excessive use of agrochemicals (fertilizers and pesticides) and waste disposal (sewage sludge and leachate when the former is used as landfill) (Prasad and Strzalka, 1999).

Some heavy metals are required for normal growth and metabolism of plants (Table 2), but if large amounts are accumulated in the plants, they will adversely affect the absorption and transport of essential elements, disturb the metabolism, and have an impact on growth and reproduction (Cheng, 2003). HM accumulation in plants depends upon plant species and the different growth stages (Cheng, 2003); the efficiency of different plants to absorb metals is evaluated by either plant uptake or soil to plant transfer factors of the metals (Chaudhary et al., 2018). After prolonged metal exposure, sensitive plants develop visible symptoms of toxicity such as chlorosis, necrotic lesions as well as disorders and growth inhibition (Dietz et al., 1999; Peralta et al., 2001).

Table 2. Range of a few environmentally important heavy metals in plants (Nagajyoti et al., 2010).

Elements	Land plants (ug g-1 dray wt)
As	0.02-7
Cd	0.1-2.4
Hg	0.005-0.02
Pb	1-13
Sb	0.02-0.06
Co	0.05-0.5
Cr	0.2-1
Cu	4.15
Fe	140
Mn	15-100
Mo	1-10
Ni	1
Sr	0.30
Zn	8-100

Photosynthesis is considered as one of the most sensitive metabolic processes to lead to toxicity. The Pb-induced reduction in the photosynthesis may be due to stomatal closure, damage to chloroplast ultrastructural organization, alteration in the metabolites of photosynthesis, replacement of ions like Mg, Mn, by Pb in the chloroplast and inhibited synthesis or degradation of the photosynthetic pigments (Islam et al., 2008). High levels of Pb also cause the inhibition of enzyme activities, water imbalance, alterations in membrane permeability, and disturb mineral nutrition (Yadav, 2010).

An excessive supply of Zn affects both root and shoot growth. Shoots become stunted and chlorotic. Further, the epidermis of roots may become lignified (Balsberg Påhlsson, 1989).

Cr has no essential role in plant metabolism, and is poorly translocated within plants. This is likely due to chromium (III) oxide binding to cell walls, leading to increased concentrations of Cr in the roots. Deleterious effects, including restricted root growth, biomass reduction, and distortion of leaf appearance, have been recorded in plants grown in media with excess of Cr (III) and Cr (VI) (Hamilton et al., 2018).

Generally, visible symptoms of copper toxicity include having small chlorotic leaves and early leaf fall. Furthermore, plant growth is stunted and the initiation of roots and the development of lateral roots become poor. The reduced root development may result in a lowered water and nutrient uptake, leading to disturbances in the metabolism and growth retardations (Balsberg Påhlsson, 1989).

The toxic effects of higher concentration of Ni are observed at multiple levels. These include the inhibition of mitotic activities, reduction in plant growth, plant water relation and photosynthesis, inhibition of enzymatic activities as well as nitrogen metabolism, interference with the uptake of other essential metal ions, and induction of oxidative stress (Yusuf et al., 2011). The decrease in water uptake is used as an indicator of the progression of Ni^{2+} toxicity in plants (Yadav, 2010).

Analysis with scanning electron microscopy shows that plant exposure to Hg resulted in loss of cell shape, decrease in intercellular spaces, and vascular abnormality in leaves of Boston fern (Nephrolepis exaltata) and Indian mustard (Brassica juncea). Mercury treatment was found to reduce the amount of chlorophyll, and resulted in breakdown of thylakoid. Furthermore, Hg stress inhibited the activity of NADPH: protochlorophyllide oxidoreductase, which is responsible for the biosynthesis of chlorophyll (Chen and Yang, 2012).

HM affects the cell division of plants. The effects are different, and depend on the concentration. The genotoxicity influences the synthesis, and the duplication of DNA and chromosomes both directly or indirectly, and induces chromosomal aberration (Cheng, 2003).

3.4 Human Health

People may be exposed to heavy metals over the course of their lifetime. HM in the environment can affect human health through various absorption pathways such as direct ingestion, consumption of foods, beverages, dermal contact, inhalation of soil dust particulates, airborne particles, and vaporized metals (Mudgal et al., 2010; Singh et al., 2011). Chronic intakes of HM have damaging effects on human beings as well as other life forms (Liu et al., 2013).

The absorption, accumulation and distribution of HM in different food crops such as rice, wheat, barley, maize and potato, oil seed crops and forage crops have been documented. Mostly, edible parts of plants are the major source of heavy-metal intake for humans through consumption, which have long-term detrimental effects on human health (Sharma and Agrawal, 2005).

HM pose hazards to human health because these are persistent in nature and have accumulation tendency in biological systems (Sharma and Agrawal, 2005). They can disturb important biochemical processes. Toxicity level depends on the type of metal, its biological role, and the type of organisms that are exposed to it (Mohod and Dhote, 2013).

Cd is a heavy metal posing severe risks to human health. Up to this day, it could not be shown that Cd has any physiological function within the human body (Suwazono et al., 2006). Cd is efficiently retained in the organism in which it accumulates throughout life (Bernard and Lauwerys, 1986). For chronic dietary exposure, the kidneys constitute the target organ. Cadmium-induced renal damage is characterized by proximal tubular absorptive dysfunction (Järup and Åkesson, 2009). The first sign of renal effects is tubular damage, characterized by increased urinary excretion of low-molecular-weight proteins or intracellular tubular enzymes. More important, in succession to the tubular effects, Cd may affect the glomerular function (Suwazono et al., 2006).

Cd interferes with calcium metabolism, leading to a reduction in calcium levels and thus reducing the density and strength of bones, often causing the weakened bones to break (Huff et al., 2007). The Itai-itai disease is a bone

disease causing fractures and severe pain. It was common after World War II in Fuchu, Toyama prefecture, Japan (Nordberg, 2009). The main features of the Itai-itai disease are pseudo fractures of the bones, osteomalacia with eventual osteoporosis, and renal dysfunction (Bernard and Lauwerys, 1986). Anemia and gastrointestinal and renal dysfunction were other less prominent findings. Elevated levels of Cd in urine were found, and in 1968, the disease was declared by the Japanese Government to be a disease related to environmental pollution (Nordberg, 2009). Acute Cd exposure via inhalation results in pulmonary edema and respiratory tract irritation (Liu et al., 2009), recent studies have also reported increasing cancer risks at low-level environmental exposure (Järup and Åkesson, 2009).

Chronic arsenic toxicity is mostly manifested in weight loss, capricious appetite, conjunctive and mucosal erythematic lesions including mouth ulceration, and reduced milk yields (Raikwar et al., 2008). The cardiovascular, gastrointestinal and urinary systems were some of the other systems most affected in humans (Kapaj et al., 2007). Similar to a protoplastic poison, it affects primarily the sulphydryl group of cells causing malfunctioning of cell respiration, cell enzymes, and mitosis (Jaishankar et al., 2014). It does cause gene amplification and chromosomal damage at lower doses, and can enhance mutagenesis by other agents, apparently by inhibiting DNA repair (Abernathy et al., 1999). The International Agency for Research on Cancer has listed arsenics as a human carcinogen since 1980. It is associated with cancers of skin and internal organs, as well as with vascular diseases (Kapaj et al., 2007).

Ni is normally present in human tissues under conditions of high exposure; these levels may increase significantly (Cempel and Nikel, 2006). The adverse health effects of Ni depend on the route of exposure (inhalation, oral, dermal), and can be classified according to systemic, immunologic, neurologic, reproductive, developmental, or carcinogenic effects (Das and Büchner, 2007). It is responsible for allergic skin reactions, and has been reported to be one of the most common causes of allergic contact dermatitis (Cempel and Nikel, 2006). The toxic effects of Ni result from its ability to replace other metal ions in enzymes, proteins or bind to cellular compounds, and among animals, micro-organisms and plants (Iyaka, 2011), it plays an important role in the suppression or silencing of genes and binds to DNA in different positions (Mishra et al., 2010).

4. Conclusion

This review is an attempt to discuss the effects of some heavy metals on soil, plants and human health. Heavy metals cannot be biodegraded, so they accumulate in living organisms. They inhibit the growth of microbes that affect the respiratory and enzymatic activity of soils, growth as well as the reproduction of plants. The uptake of heavy metals by plants and their subsequent accumulation along the food chain pose potential threats to animal and human health. Soils contaminated with heavy metals constitute a serious threat to ecosystems and consequently to human health.

References

Abernathy, C. O., Liu, Y. P., Longfellow, D., Aposhian, H. V., Beck, B., Fowler, B., Goyer, R., Menzer, R., Rossman, T., Thompson, C., Waalkes, M. (1999). Arsenic: Health Effects, Mechanisms of Actions, and Research Issues. Environ Health Perspectives 107 (7): 593–597.

Alkorta, I., Hernandez-Allica, J., Becerril, J. M., Amezaga, I., Albizu, I., Garbisu, C. (2004). Review recent findings on the phytoremediation of soils contaminated with environmentally toxic heavy metals and metalloids such as zinc, cadmium, lead, and arsenic. Reviews in Environmental Science and Bio/ Technology 3: 71–90.

Babich, H., and Stotzky, G. (1983). Toxicity of Nickel to Microbes: Environmental Aspects. Advances in Applied Microbiology 29: 195-265.

Balsberg Påhlsson, A.M. (1989). A literature review Toxicity of heavy metals (Zn, Cu, Cd, Pb) to vascular plants. Water, Air, and Soil Pollution 47(3–4): 287–319.

Bernard, A., and Lauwerys, R. (1896). Effects of Cadmium Exposure in Humans. Cadmium 80(5): 135-177.

Biney, C., Amuzu, A. T., Calamari, D., Kaba, N., Mbome, I. L., Naeve, H., Ochumba, P. B. O., Osibanjo, O., Radegonde, V., Saad, M. A. H. (1994). Review of heavy metals in the African aquatic environment. Ecotoxicology and Environmental Safety 28 (2): 134-159.

Bradl, H. B. (2005). Chapter 1 Sources and Origins of Heavy Metals. In Bradl, H. B. (Ed.), Heavy Metals in the Environment: Origin, Interaction and Remediation. Interface Science and Technology 6: 1-27. Doi.org/10.1016/S1573-4285 (05)80020-1.

Bruins, M. R., Kapil, S., Oehme, F. W. (2000). REVIEW Microbial Resistance to Metals in the Environment. Ecotoxicology and Environmental Safety 45 (3): 198-207.

Bulgariu, L., and Gavrilescu, M. (2015). Bioremediation of Heavy Metals by Microalgae. Handbook of Marine Microalgae 30:457-469.

Cempel, M., and Nikel, G. 2006. Nickel: A Review of Its Sources and Environmental Toxicology. Polish Journal of Environmental Studies 15: 375-382.

Chaudhary, K., Agarwal, S., Khan, S. (2018). Role of Phytochelatins (PCs), Metallothioneins (MTs), and Heavy Metal ATPase (HMA) Genes in Heavy Metal Tolerance. Mycoremediation and Environmental Sustainability 2: 39-60. DOI: 10.1007/978-3-319-77386-5_2.

Chen, J., and Yang, Z. M. (2012). Mercury toxicity, molecular response and tolerance in higher plants. Biology of Metals 25(5): 847–857. DOI: 10.1007/s10534-012-9560-8

Cheng, S. (2003). Effects of Heavy Metals on Plants and Resistance Mechanisms. Environmental Science and Pollution Research 10(4): 256–264.

Das, K. K., and Büchner, V. (2007). Effect of Nickel Exposure on Peripheral Tissues: Role of Oxidative Stress in Toxicity and Possible Protection by Ascorbic Acid. Reviews on Environmental Health 22(2): 157-173.

Dietz, K. J., Kramer, U., Baier, M. (1999). Free Radicals and Reactive Oxygen Species as Mediators of Heavy Metal Toxicity in Plants. Heavy Metal Stress in Plants 4: 73-97.

Dzyadevych, S., and Jaffrezic-Renault, N. (2014). Conductometric biosensors. Biological Identification 6: 153-193.

Forneris, J. (2002). Impacts des polluants métalliques sur les micro-organismes du sol. University Paris Val de Marne.

Gillera, K. E, Witterb, E., Mcgrathc, S. P. (1998). Toxicity of heavy metals to microorganisms and microbial processes in agricultural soils: a review. Soil Biology and Biochemistry 30(10–11): 1389-1414.

Gu, Y. G., Lin, Q., Wang, X. H, Du, F. Y., Yu, Z. L., Huang, H. H. (2015). Heavy metal concentrations in wild fishes captured from the South China Sea and associated health risks. Marine Pollution Bulletin 96(1–2): 508-512.

Hamilton, E. M., Young, S. D., Bailey, E. H., Watts, M. J. (2018). Chromium speciation in foodstuffs: a review. Food Chemistry 250: 105-112.

Huff, J., Lunn. R. M., Waalkes, M. P., Tomatis. L., Infante, P. F. (2007). Cadmium-induced Cancers in Animals and in Humans. International Journal of Occupational and Environmental Health 13(2): 202-212.

Islam, E., Liu, D., Li, T., Yang, X., Jin, X., Mahmood, Q., Tian, S., Li, J. (2008). Effect of Pb toxicity on leaf growth, physiology and ultrastructure in the two ecotypes of Elsholtzia argyi. Journal of Hazardous Materials 154(1–3): 914-926.

Iyaka, Y. A. (2011). Nickel in soils: A review of its distribution and impacts. Scientific research and essays 6(33): 6774-6777.

Jaishankar, M., Tseten, T., Anbalagan, N., Mathew, B. B., Beeregowda, K. N. (2014). Toxicity, mechanism and health effects of some heavy metals. Interdisciplinary toxicology 7(2): 60–72. DOI: 10.2478/intox-2014-0009.

Järup, L., and Åkesson, A. (2009). Current status of cadmium as an environmental health problem. Toxicology and Applied Pharmacology 238(3): 201-208.

Joseph, B., Raj, J. S., Edwin, B., Sankarganesh, P., Jeevitha, M. V., Ajisha, S.U., Rajan, S. S. (2010). Toxic effect of heavy metals on aquatic environment. International Journal of Biological and Chemical Sciences 4(4): 939-952. DOI: 10.4314/ijbcs.v4i4.62976.

Kapaj, S., Peterson, H., Liber, K., Bhattacharya, P. (2007). Human Health Effects from Chronic Arsenic Poisoning–A Review. Toxic/Hazardous Substances and Environmental Engineering 41(10): 2399-2428.

Kumar, R., Mishra, R. K., Mishra, V., Qidwai, A., Pandey, A., Shukla, S. K., Pandey, M., Pathak, A., Dikchit, A. (2016). Detoxification and Tolerance of Heavy Metals in Plants. Plant Metal Interaction 13: 335-359.

Liu, J., Qu, W., Kadiiska, M. B. (2009). Role of oxidative stress in cadmium toxicity and carcinogenesis. Toxicology and Applied Pharmacology 238(3): 209-214.

Liu, X., Song, Q., Tang, Y., Li, W., Xu, J., Wu, J., Wang, F., Brookes, P. C. (2013). Human health risk assessment of heavy metals in soil–vegetable system: A multi-medium analysis. Science of the Total Environment 463–464: 530-540.

Lusi, E. A., Patrissi, T., Guarascio, P. (2017). Nickel-resistant bacteria isolated in human microbiome. New Microbes and New Infections 19: 67-70.

Madoni, P. (2000). The acute toxicity of nickel to freshwater ciliates. Environmental Pollution 109(1): 53-59.

Mishra, S., Dwivedi, S. P., Singh, R. B. (2010). A Review on Epigenetic Effect of Heavy Metal Carcinogens on Human Health. The Open Nutraceuticals Journal 3(1): 188-193.

Mohod, C. V., and Dhote, J. (2013). Review of Heavy Metals in Drinking Water and Their Effect on Human Health. International Journal of Innovative Research in Science, Engineering and Technology 2(7): 2992-2996.

Morais, S., Costa, F. G., Pereira, M. L. (2012). Heavy Metals and Human Health. Environmental Health. Emerging Issues and Practice 10: 227-247.

Moreno, J. L., García, C., Hernández, T. (2003). Toxic effect of cadmium and nickel on soil enzymes and the influence of adding sewage sludge. European Journal of Soil Science 54: 377-386.

Mudgal, V., Madaan, N., Mudgal, A., Singh, R. B., Mishra, S. (2010). Effect of Toxic Metals on Human Health. The Open Nutraceuticals Journal 3: 94-99.

Mustapha, M. U., and Halimoon, N. (2015). Screening and isolation of heavy metal tolerant bacteria in industrial effluent. Procedia Environmental Sciences 30: 33-37.

Nagajyoti, P. C., Lee, K. D., Sreekanth, T. V. M. (2010). Heavy metals, occurrence and toxicity for plants: a review. Environmental Chemistry Letters 8(3): 199-216.

Nordberg, G. F. (2009). Historical perspectives on cadmium toxicology. Toxicology and Applied Pharmacology 238(3): 192-200.

Oves, M., Saghir Khan, M., Huda Qari, A., Nadeen Felemban, M., and Almeelbi, T., 2016. Heavy Metals: Biological Importance and Detoxification Strategies. Journal of Bioremediation and Biodegradation 7(2): 1-15.

Panigrahi, S., Velraj, P., Rao, T. S. (2019). Functional Microbial Diversity in Contaminated Environment and Application in Bioremediation. Microbial Diversity in the Genomic Era 21: 359-385.

Peralta, R., Gardea-Torresdey, J. L., Tiemann, K. J., Gomez, E., Arteaga, S., Rascon, E., Parsons, J. G. (2001). Uptake and Effects of Five Heavy Metals on Seed Germination and Plant Growth in Alfalfa (Medicago sativa L.). Bulletin of Environmental Contamination and Toxicology 66(6): 727-734.

Prasad, M.N.V., and Strzalka, K. (1999). Impact of Heavy Metals on Photosynthesis. Heavy Metal Stress in Plants 6: 117-138.

Raikwar, M.K., Kumar, P., Singh, M. Singh, A. (2008). Toxic effect of heavy metals in livestock health. Veterinary World 1(1): 28-30.

Scott-Fordsmand, J. J. (1997). Toxicity of Nickel to Soil Organisms in Denmark. In: Ware, G. W., Nigg, H.N., Bevenue, A. (Eds.), Reviews of Environmental Contamination and Toxicology: Continuation of Residue Reviews, Springer, New York, 1-34. https://doi.org/10.1007/978-1-4612-2264-4_1.

Sharma, R. K., and Agrawal, M. 2005. Biological effects of heavy metals: An overview. Journal of Environmental Biology 26: 301-313.

Shazili, N. A. M., Yunus, K., Ahmad, A. S., Abdullah, N., Abd Rashid, M. K. (2006). Heavy metal pollution status in the Malaysian aquatic environment. Aquatic Ecosystem Health and Management 9(2): 137-145.

Singh, J., and Kalamdhad, AS. (2011). Effects of Heavy Metals on Soil, Plants, Human Health and Aquatic Life. International Journal of Research in Chemistry and Environment 1 (2): 15-21.

Singh, R., Gautam, N., Mishra, A., Gupta, R. (2011). Heavy metals and living systems: An overview. Indian Journal of Pharmacology 43(3): 246-53.

Suwazono, Y., Sand, S., Vahter, M., Falk Filipsson, A., Skerfving, S., Lidfeldt, J., Åkesson, A. (2006). Benchmark Dose for Cadmium-Induced Renal Effects in Humans. Environmental Health Perspectives 114(7): 1072-1076.

Tangahu, B. V., Sheikh Abdullah, S. R., Basri, H., Idris, M., Anuar, N., Mukhlisin, M. (2011). A Review on Heavy Metals (As, Pb, and Hg) Uptake by Plants through Phytoremediation. International Journal of Chemical Engineering ID 939161, 31 Pp. doi.org/10.1155/2011/939161.

Timberley, M., R., Ian, L. P., T., Terry, G. J. (2015). Chapter 18 - Microorganisms and Metal Pollutants. Environmental Microbiology (Third edition) 2015, Pages 415-439. Doi. org/10.1016/B978-0-12-394626-3.00018-1

Verma, N., and Kaur, G. (2016). Trends on Biosensing Systems for Heavy Metal Detection. Comprehensive Analytical

Chemistry 75(2): 33-71.

Villanneau, E., Perry-Giraud, C., Saby, N., Jolivet, C., Marot, F., Maton, D., Floch-Barneaud, A., Antoni, V., Arrouays, D. (2008). Détection de valeurs anomaliques d'éléments traces métalliques dans les sols à l'aide du Réseau de Mesure de la Qualité des Sols. Etude et Gestion des Sols 15(3): 183-200.

Wang, X., Gai, L., Sun, X., Xie, H., Gao, M., Wang S. (2010). Effects of long-term addition of Cu (II) and Ni (II) on the biochemical properties of aerobic granules in sequencing batch reactors. Applied Microbiology and Biotechnology 86: 1967-1975.

Wuana, R. A., and Okieimen, F. E. (2011). Heavy Metals in Contaminated Soils: A Review of Sources, Chemistry, Risks and Best Available Strategies for Remediation. International Scholarly Research Notices Ecology 2011. Article ID: 402647. https://doi.org/10.5402/2011/402647

Yadav, S. K. (2010). Review Heavy metals toxicity in plants: An overview on the role of glutathione and phytochelatins in heavy metal stress tolerance of plants. South African Journal of Botany 76(2): 167-179.

Yahya, Al. N., Mohamed, S. K., Mohamed, A. G. (2018). Environmental Pollution by Heavy Metals in the Aquatic Ecosystems of Egypt. Open Access Journal of Toxicology 3(1): 1-9.

Yusuf, M., Fariduddin, Q., Hayat, S., Ahmad, A. (2011). Nickel: An Overview of Uptake, Essentiality and Toxicity in Plants. Bulletin of Environmental Contamination and Toxicology 86(1): 1-17.

Zhuang, P., McBride, M.B., Xia, H., Li, N., Li, Z. (2009). Health risk from heavy metals via consumption of food crops in the vicinity of Dabaoshan mine, South China. Science of the Total Environment 407(5): 1551-1561.

JJEES

Jordan Journal of Earth and Environmental Sciences

JJEES (2020) 11 (4): 241-247
ISSN 1995-6681

Strain Analysis of Dana Conglomerates in Ad Dhira Area- Dead Sea

Mohammad Al-Adamat and Abdullah Diabat*

Al al- Bayt University, Institute of earth and environmental sciences, Department of applied earth and environmental sciences

Received 24 January 2020; Accepted 20 April 2020

Abstract

This research is aimed at calculating the strain ellipses to investigate the intensity of deformation in different stations of Dana Conglomerate Formation (DCF). The investigated area lies to the eastern margin of the Dead Sea, in the Ad Dhira area. The outcropping rocks in the investigated area range from the Upper Cretaceous to the Quaternary age. The DCF was deposited in tectonically unstable basins during an extensional tectonic phase. Its deposition is associated with early rift tectonics and also was affected by Neogene movements. The DC is used in this study as a strain indicator using Fry method. The performed strain analysis in 2D showed a high deformation for most of the oriented photographed samples, where the shape of the ellipse is a flattened type, while a few showed a low deformation, where the shape of the ellipse is of the semi-circle type and the R- ratios range from 1.123 to 2.248.

Keywords: Dead Sea, Ad Dira area, strain analysis, Fry method.

1. Introduction

Strain as a concept in geology is any change in length or shape of the rocks that resultin deformation. Mostly defined for ductile deformation, however, it is also used in areas of faulting (Fossen, 2016). In this study, the state of strain observed in the rocks is known as the finite strain; this results from a succession of very small strain increments over a period of time (Marshak and Mitra, 1988). It is graphically represented by strain ellipsoid that is the result of the strain from a unit sphere.

Strain analysis (SA) is a significant aspect of structural geology (Vollmer, 2019), which deals with the quantification of geological deformation (Lisle, 1985). It is an essential method for a perfect understanding of the finite deformations of the lithosphere (Yamaji, 2008). It offers an opportunity to discover the state of strain in rock and to map out strain variations in a region, an outcrop, or a sample (Fossen, 2016) Moreover, the SA gives insight into both the distribution of strain and the mechanism of development of ductile structures in the earth's crust (Kumar et al., 2014). It is a tool for unraveling tectonic histories (Mulchrone, 2013).

The investigated area lies to the east of the Dead Sea Basin (DSB) which is part of the most conspicuous structural feature in the Middle East that is the Dead Sea Transform Fault (DSTF). The DSTF is an active left-lateral fault zone, with approximately 1100 km of length (Weber et al., 2009). It constitutes the northern part of the Syrian-African rift system, which spans 6000 km from Turkey to Mozambique (Ben-Avraham et al., 2012). It forms the tectonic boundary between the Arabian plate to the East and the Sinai subplate to the West (Lefevre et al., 2018). Moreover, the motion along the DSTF is transferred from the opening of the Red Sea in the south to the Taurus- Zagros collision zone in Turkey and Iran to the north (Ben-Avraham et al., 2005) (Figure1).

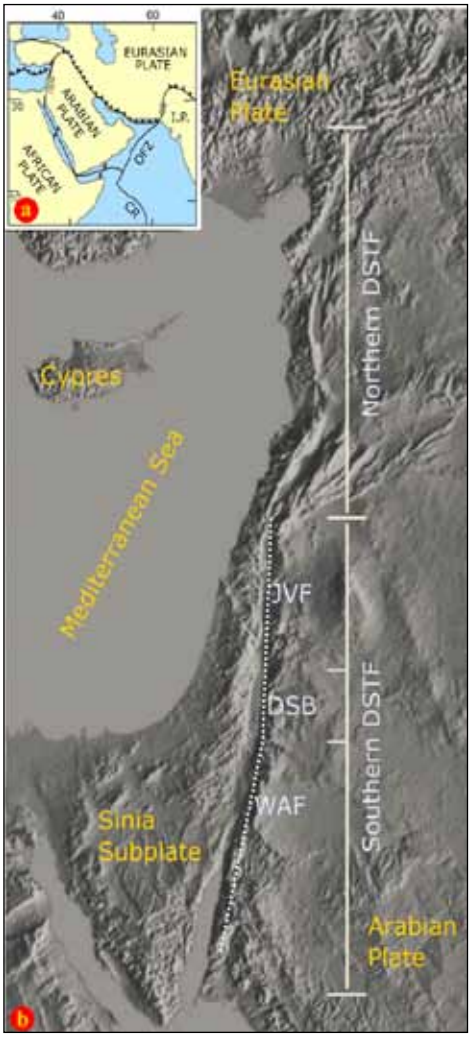

Figure 1. a) Tectonic setting of the area of the DSTF and b) Digital terrain model (DTM) showing the divisions of the DSTF into the northern and southern sections (Modified from Lazar, 2019)

* Corresponding author e-mail: adiabat@aabu.edu.jo

The area under investigation is located at the eastern margin of the Dead Sea, in the Ad Dhira area (Figure 1). The Dana Conglomerates Formation (DCF) as a unit was deposited in tectonically unstable basins during an extensional tectonic phase. The deposition of the formation was associated with early rift tectonics, and the beds are affected by Neogene movements (Powell, 1988).

Geographically, it extends from (31° 12' 26.96" to 31° 16' 19.07") N and (35° 30' 58.29" to 35° 35' 24.24") E. It covers an area of 35 Km^2 (Figure 2).

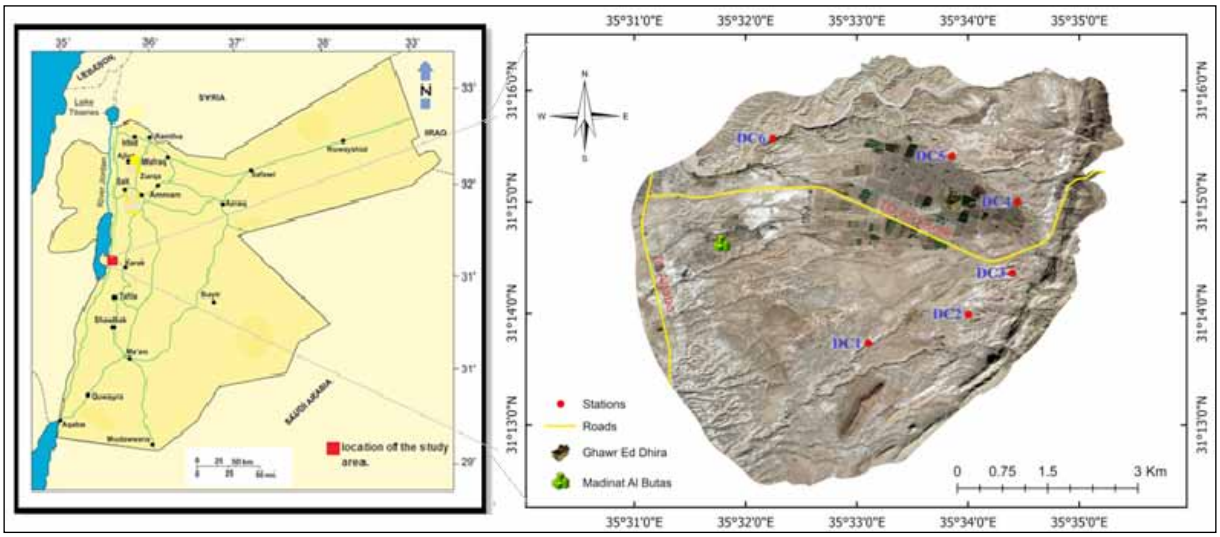

Figure 2. Location map and Satellite image of the investigated area.

The investigated area varies in elevation from 383m below sea level (b.s.l) along the western part to 233 m above sea level (a.s.l) in the eastern part (Figure 3). It is of a low relief adjacent to the Lisan peninsula comprising alluvial fans, lake deposits and lacustrine fans deposited by stream following from the mountains to the Dead Sea depression (Powell, 1988). Moreover, the area is characterized by the presence of valleys and hills.

The main aim of this study has been to apply a suitable method of strain analysis in Dana Conglomerates as there are no such researches except the work of Al- Diabat (1999 and 2002), in which he used quartz in sandstone and oolites in limestone as strain indicators. The achievement of the above objective would contribute to increasing knowledge about the intensity of deformation in six measurement stations of the investigated area (Figure 4).

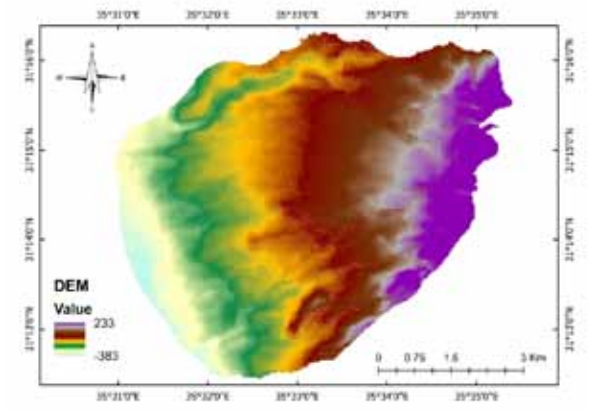

Figure 3. Digital elevation map of the investigated area.

2. Geological Setting

2.1 Stratigraphy

The investigated area presents sediment sequences ranging from the Upper Cretaceous to the Quaternary age (Figure 4).

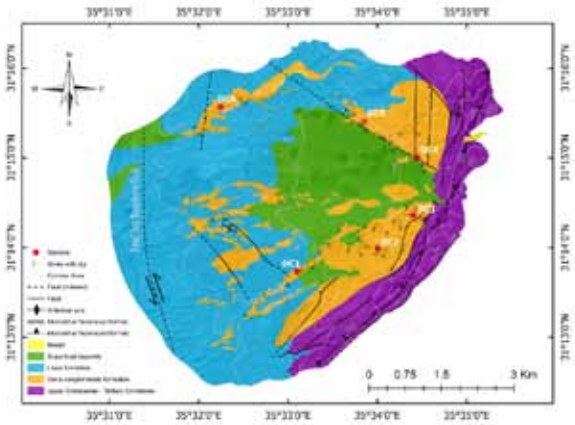

Figure 4. Geological map of the investigated area (Modified after Powell, 1988), with the established field stations.

2.1.1. Dana Conglomerate Formation (DCF)

The deposition of the DCF was associated with early rift tectonics and the beds are also affected by Neogene movements (Powell, 1988). Moreover, this formation has been subdivided by Powell (1988) into informal lower- and upper-members equivalent to the subdivision of Bender (1974) who also referred to this unit as the Syntectonical Conglomerate. These members are described as follows:

The lower member which is comprised of thick beds of pebble to boulder conglomerate composed of well-rounded, poorly graded, clast of chert, chalk and chalky limestone derived from the Umm Rijam Formation. The Texture is mostly clast-supported, but matrix-supported areas are also present. Furthermore, synsedimentary normal faults

with centimeter throws are common in some of the thicker conglomerate beds (Powell, 1988; Khalil, 1992).

The upper member is composed of thick beds of clast-supported, well rounded, poorly sorted, pebble-boulder conglomerate with a calcarenite/ siliclastic matrix. It has not yielded any fauna, but it is overlain by Pleistocene basalts and gravel with middle Pleistocene flint implements in the Dana area (Bender, 1974), so the age of this unit cannot be established more accurately than the Miocene to Middle Pleistocene; a major synchronous depositional phase in response to the synchronous tectonic activity along the rift margins (Powell, 1988).

2.2. Tectonic Setting

The DSTF is a prominent shear zone in the region (Maercklin et al., 2005). It has been active since Early Miocene owing to its activity. Along the DSTF, many morphotectonic features were formed such as fault scarps, offset of stream courses, alluvial fans, pressure ridges, linear valleys, and sag ponds (Garfunkel, 1981; Galli, 1999; Al-Taj,2000; Klinger et al., 2000; Niemi et al., 2001; Atallah and Al–Taj, 2004). The Ad Dhira area is situated on the eastern side of the Dead Sea to the East of the Lisan Peninsula. It is bounded by the Ad Dhira monocline and splay fault to the east, to the west by the DSTF and in the northeast by the Siwaqa Fault (Figure 5).

Figure 5. A satellite image showing the tectonic setting of Ad Dhira area and the main geological structures of the investigated area. Inset image shows the Dead Sea region.

The Ad Dhira fault is a major NE-SW trending splay fault that branches off the main Dead Sea structure in the area of Wadi Assal few kilometers south of the study area. The southern part of the Wadi Ad Dhira structure shows an overall displacement of 500 m with a down throw to the NW. Moreover, along the fault trace, the beds are often crushed or shattered by small faults. This Fault disappears and passes into a major monoclinal flexure with minor faults (Powell, 1988). Rhomb- shaped faulted blocks are bounded by N-S and NW-SE trending faults and are well preserved in the strata belonging to the Dana Conglomerate Formation in the Ad Dhira Plain (Khalil, 1992). Most of the folds in the investigated area are directly related to flexuring adjacent to the associated faults; these include the Ad Dhira fault-monocline (Powell, 1988). This major flexure extends from Wadi Assal in the south to the Siwaqa fault in the north. It forms an arc-like structure trending NE in the south, N in the middle, and NNW in the northern part (Figure 5).

3. Methodology

3.1 Strain Markers

The most paramount principle in the strain analysis (SA) is finding the appropriate markers that assist geologists for strain studies. The key to the SA lies in getting objects with known initial packing arrangement or features which enable final angles or lengths to be measured. Strain markers are objects showing the state of strain in a deformed medium, i.e. objects or lines of known undeformed shape, length and/or orientation. They reveal how much the rock has been strained, and give information about the nature of the deformation (Fossen, 2016). Furthermore, some strain markers are comprised of individual objects with a specific shape (e.g., fossils, and sedimentary clast outlines), and other strain markers may contain groups of objects with particular orientation patterns (e.g., preferred orientation patterns of muscovites in a sample of slate) (Lisle, 2010). Conglomerates are usually used for the SA, and their regular occurrence in the geological succession makes them promising strain-marker horizons (Treagus and Treagus, 2002). However, according to Ramsay and Huber (1983); Lisle (2010); and Mulchrone (2013), strain markers can be grouped into three general categories as follows:

a) Geometric: Objects or collections of objects with known pre-strain geometries.
b) Ellipses: Objects whose shapes can be approximated by ellipses.
c) Points: Groups of objects whose special arrangement defines a fabric.

3.2 Fry Method

The Fry method is a quicker and visually more impressive method for finding a two-dimensional strain (Fossen, 2016). It was developed by Norman Fry (Fry, 1979), and it is considerd a significant and widely-used method for analyzing point distribution data (Vollmer, 2019). This technique is based on the hypothesis that an initially uniform anti-clustered distribution of points will change after deformation into a nonuniform distribution. The distance between points become decreased in the contractional field and increased in the extensional field of strain (Marshak and Mitra, 1988). This method depends on a plot of the position of every particle center with respect to a particle put at the origin. The origin is, then, sequentially placed on each center, and the relative position of every other center is plotted (Genier and Epard, 2007). This produces a graphical point distribution; it

is called the "Fry plot" that immediately shows the ellipse in form of a characteristic central vacancy and/ or a high point density ring in the vicinity of the central vacancy (Kumar et al., 2014). The practicability and accuracy of measuring strain in this method is greatly dependent on the type and degree of ordering of centers and the number of centers taken into consideration (Fry, 1979).

Owing to its applicability to a wide range of situations and procedural simplicity, this technique is adopted by many contemporary studies around the world (e.g. Genier and Epard 2007; Longet al.; 2011; Eichelberger and McQuarrie, 2014; Kassem and Hamimi, 2018). It is most easily dealt with using one of the numerous available computer programs (Fossen, 2016). In the present research, the Fry method is used through Ellipsfit software because it is more appropriately used compared to other methods for strain markers that are found in the area of investigation.

3.3 Strain Data Analysis

Photographs of oriented sections in an outcrop of Dana Conglomerate Formation were used as strain indicators. In the present research, strain analysis was conducted using the Fry method through EllipseFit software (Vollmer, 2019). The Ellipse Fit software is an integrated program for geological fabric and strain analysis. It is used for determining two- and three-dimensional strain from oriented photographs of outcrop surfaces, hand samples and thin sections using various objects including center points, lines, ellipses polygons, and shapes. The software involves procedures for complete fabric and strain analyses, including digitizing, image processing, calculation of two-dimensional sectional ellipses, and the combination of sections to get three-dimensional ellipsoid (Vollmer, 2019).

4. Results

Within the area of investigation, it was difficult to locate three perpendicular sectional blocks of rock to determine the Ellipsoid in 3D. In order to apply the Fry method in 3D, a cutting technique in the field is required to prepare the oriented samples in three dimensions. This technique was impractical given the financial restraints in support of this research. Therefore, oriented photographs of Dana Conglomerate Formation (DC) outcrops, which have strain markers, were taken in all field stations. These photographs were used for determining the Ellipse in 2D. The results of strain analysis in all stations are arranged in Table (1).

Table 1. Results of strain analysis of all stations

Station		P	X	Z	R	ϕ	RMS
DC1	a	220	71.474	63.643	1.123	17.77°	0.0735
	c	500	43.593	19.391	2.248	175.26°	0.0451
DC2		320	47.894	27.951	1.714	158.00°	0.0468
DC3	a	230	72.118	38.488	1.874	50.76°	0.0409
	c	210	71.355	57.103	1.250	164.59°	0.2054
	e	310	49.242	24.710	1.993	0.74°	0.0963
DC4	a	500	48.597	27.940	1.739	151.85°	0.0321
	c	380	69.334	42.004	1.651	149.63°	0.0840
	e	600	44.045	34.320	1.283	10.11°	0.0857
DC5		218	57.607	36.956	1.559	32.77°	0.0606
DC6	a	565	45.673	20.825	2.193	163.54°	0.0695
	c	260	40.908	18.967	2.157	176.65°	0.0373

(St.: stations, P: points, X:maximum elongation axis, Z:minimum elongation axis, R:ellipse ratio, ϕ:Orientation of ellipse long axis clockwise from X axis, and RMS: root mean square).

Moreover, after the application of the steps in the field of strain analysis, the following are the outcomes of each station:

4.1. Field Station DC1

In this station, two oriented photographs were taken. The result of strain analysis shows that the first photograph, ellipse (E),is characterized by maximum elongation axis (X) = 71.474, minimum elongation axis (Z) = 63.643 and ellipse ratio (R) = 1.123. The shape of the ellipse is semicircular, and that suggests a low degree of deformation, which can be observed by the slight difference between the length of the X and Z (Figure7 a and b). On the other hand, the second photograph E is characterized by the X = 43.593, Z=19.391, and The R = 2.248. The shape of the ellipse is a flattened type, and in this case, it shows a greater degree of deformation and a big difference between the length of the X and Z (Figure 6 c and d).

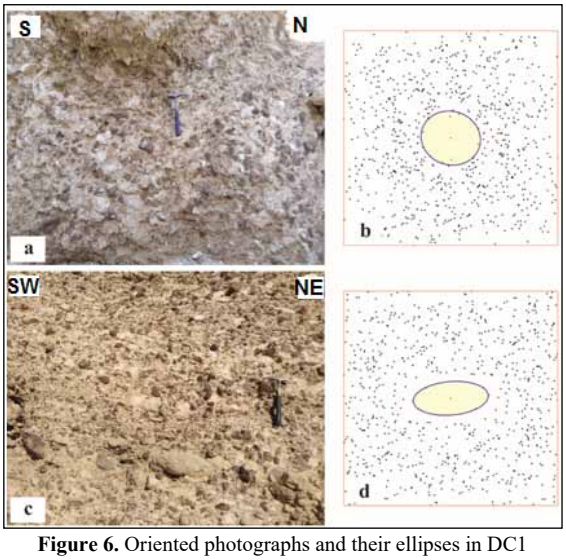

Figure 6. Oriented photographs and their ellipses in DC1

4.2. Field Station DC2

In DC2, only one oriented photograph has been taken. The result of strain analysis shows that photograph E is characterized by the X = 47.894,

Z=27.951, and the R = 1.714. The shape of this ellipse is a flattened type; thus, this shape indicates that a great degree of deformation; also the difference between the X and Z is high as it is observed (Figure 7 a and b).

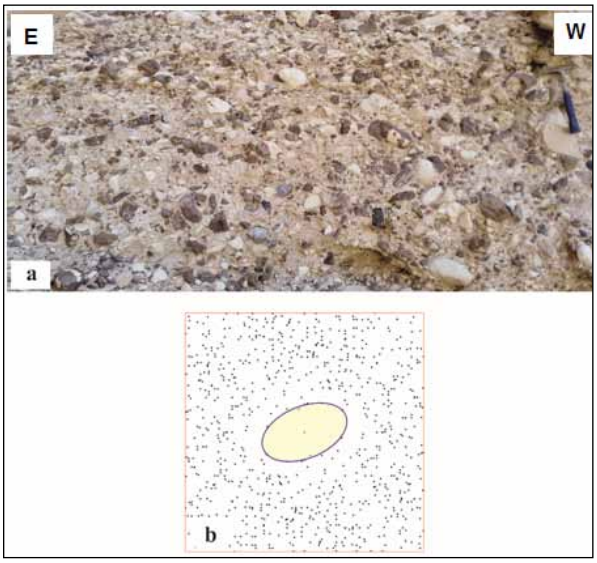

Figure 7. Oriented photograph and its ellipse in DC2.

4.3 Field Station DC3:

Three oriented photographs were taken in this station. The result of strain analysis shows that the first photograph E is characterized by the X= 72.118, Z=38.488, and R= 1.874. The ellipse is a flattened, and it suggests a great degree of deformation (Figure9 a and b). The second photograph E is characterized by the X = 71.355, Z=57.103, and R=1.250. The shape of the ellipse is almost circular, and that shows a low degree of deformation (Figure9c and d), while the third one E is characterized by the X= 49.242. Z= 24.710, and R= 1.993. Ellipse is flattened, and it indicates a great degree of deformation here (Figure 8e and f).

4.4 Field Station DC4

In this station, three oriented photographs were taken. The result of strain analysis shows that the first photograph E is characterized by the X= 48.597, Z= 27.940, and R= 1.739 (Figure 10a and b). The second photograph E is characterized by the X = 69.334, Z= 42.004, and R= 1. 651 (Figure 10c and d). The shape of the ellipses in both of the first and second photographs is a flattened type which suggests a great degree of deformation and an observed difference between the length of the X and Z. The third one E is characterized by the X= 44.045, Z= 34.320, and R= 1.283. The shape of the ellipse is almost circular, and that shows a low degree of deformation, which can be observed by the small difference between the length of the X and Z (Figure 9 e and f).

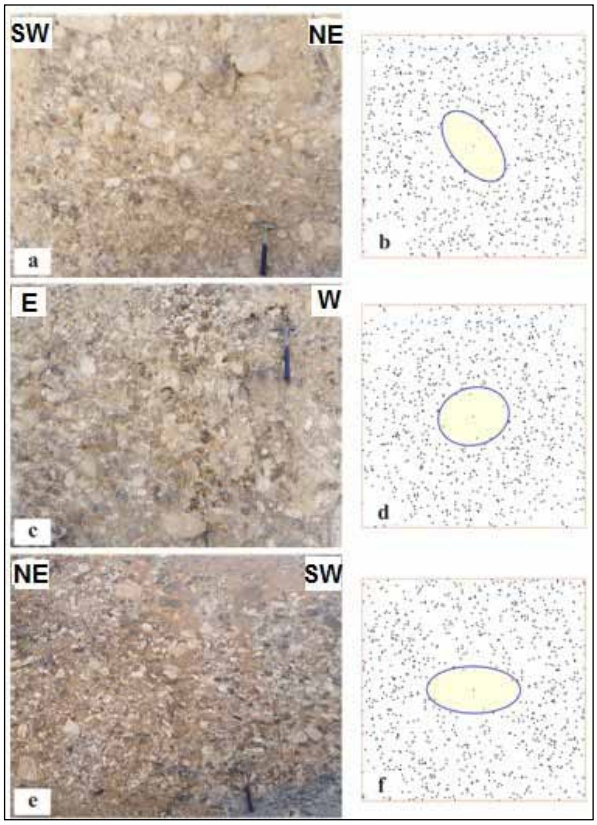

Figure 8. Oriented photographs and their ellipses in DC3.

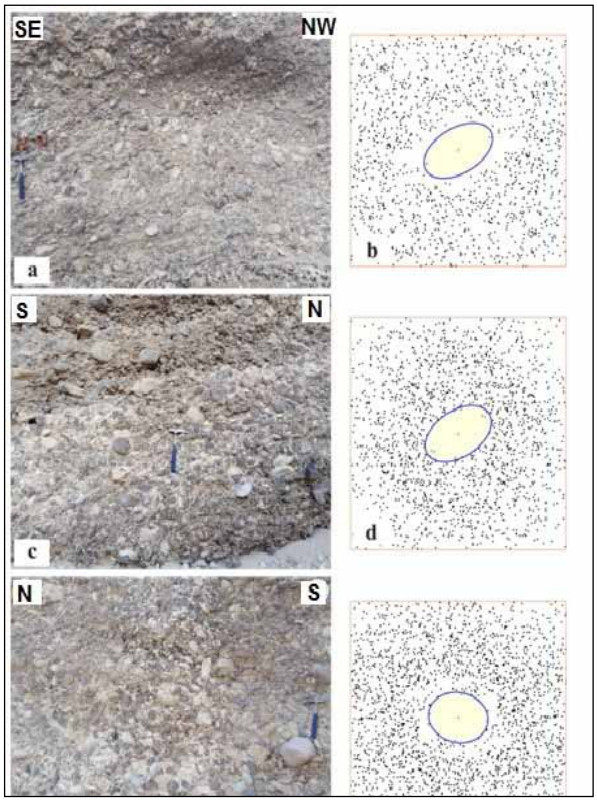

Figure 9. Figure9. Oriented photographs and their ellipses in DC4.

4.5 Field Station DC5

In DC2, only one oriented photograph has been taken. The result of strain analysis shows that the photograph E is characterized by the X =57.607, Z=36.956, and The R =1.559. The shape of this ellipse is a flattened type; thus, this shape indicates that there was a great degree of deformation here (Figure 10 a and b).

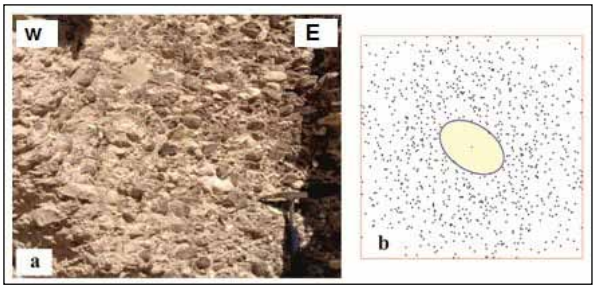

Figure 10. Oriented photograph and its ellipse in DC5.

4.6 Field Station DC6

Two oriented photographs were taken in this station. The result of strain analysis shows that the first photograph E is characterized by the X= 45.673, Z= 20.825, and R= 2.193. The second photograph E is characterized by the X = 40.908, Z= 18.967, and R= 2.157. For both photographs, the ellipses are a flattened type, and this suggests a great degree of deformation (Figure 11).

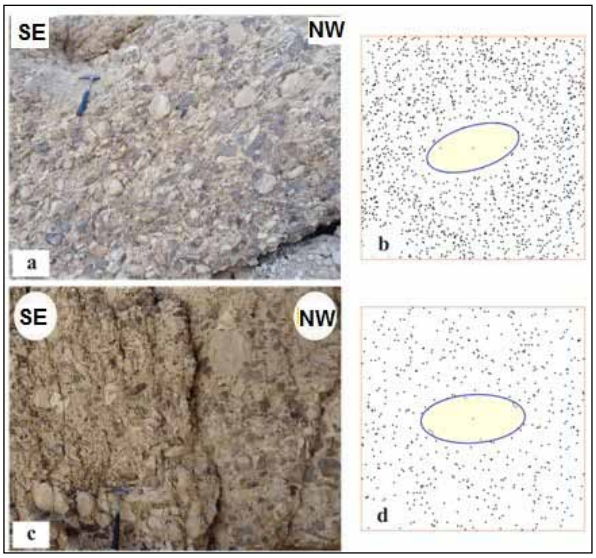

Figure 11. Oriented photographs and their ellipses in DC6.

5. Discussion and Conclusions

The outcropping rocks in the investigated area range from the Upper Cretaceous to the Quaternary. The DC was deposited in tectonically unstable basins during an extensional tectonic phase. Its deposition was associated with early rift tectonics and was also affected by Neogene movements. This is inferred from the observation of meso-scale extensional, transtensional and syndepositional structures in most stations of the study area e.g., faults mainly normal and strike-slip, negative flower structures, grabens and horsts, step- normal faults, sigmoidal en echelon joints, plumose joints, and tension gashes (see Al- Adamat, 2020).

In the current research, Fry method was applied for strain analysis in 2D for oriented photographs that have been taken in the field stations. Results of strain analysis for most oriented photographs showed that there is a high deformation where the shape of the ellipse is a flattened type (Figs. 7 d, 8, 9b and f, 10 b and d, 11, and 12). On the other hand, few oriented photographs showed a low deformation where the shape of the ellipse is of the semi-circle type (Figs. 7 b, 9 d, and 10 f).There are several orientations in flattening axes. This means that there is rotation in the area along major faults between the stations, and even local rotation between the same sampling area of the same station along small structures.

The Fry method was successfully used in Dana conglomerates as strain indicators in 2D strain analysis. The R-ratios in the investigated stations range from 1.123 to 2.248 which can be considered as a relative deformational scale in the study area at least in the investigated stations. This is due to local variations in the strain intensity from one place to another in a small specific area, which is related to the local geological structures that affected the sample sectional area.

The findings of this research have an important impression for future practice i.e. to carry out a study to determine the principal strain axes and the shape of strain ellipsoids in 3D using both Fry method and Rf/φ method, and to compare the relationship between stress and strain in order to accurately understand the dynamics of the investigated area.

References

Al- Adamat, M. (2020). Structural setting of Dana Conglomerate in Ed Dhira Area-Dead Sea, Unpublished MSc thesis, Al al-Bayt University, Mafraq, Jordan.

Al-Diabat, A. A. (1999). Paleostress and strain analysis of the Cretaceous rocks in the eastern margin of the Dead Sea Transform Fault, Unpublished Doctoral dissertation, Baghdad University, Iraq.

Al-Diabat, A. A. (2002). Strain analysis of the Cretaceous rocks at the eastern margin of the Dead Sea Transform Fault.Dirasat, series B: Pure Sciences29(2): 159- 173.

Al-Taj, M. (2000). Active faulting along the Jordan Valley segment of the Jordan -Dead Sea Transform, Unpublished Doctoral dissertation, The University of Jordan, Amman, Jordan.

Atallah, M., and Al-Taj M. (2004). Active surface ruptures of the Dead Sea Transform in Wadi Araba, Jordan. Dirasat, series B: Pure Sciences 31(1): 59– 81.

Ben-Avraham, Z., Lazar, M., Schattner, U., Marco, S. (2005). The Dead Sea Fault and its Effect on Civilization. In Wenzel, F. (Ed.), Perspectives in Modern Seismology (pp.145-163). Springer -Verlag, Heidelberg.

Ben-Avraham, Z., Lazar, M., Garfunkel, Z., Reshef, M., Ginzburg, A., Rotstein, Y., Shulman, H. (2012). Structural styles along the Dead Sea Fault. In: Roberts, D.G., and Balley, A.W. (Eds.), Phanerozoic Regional Geology of the World (1sted.), pp. 612- 633). Elsevier.

Bender, F. (1974). Geology of Jordan. Contributions to the Regional Geology of Earth, vol. 7. Gebrüder Borntraeger, Berlin (Supplement pp. 196).

Eichelberger, N., and Mcquarrie, N. (2014). Three-dimensional (3-D) finite strain at the central Andean orocline and implications for grain-scale shortening in orogens.Geological

Society of America Bulletin 127: 87–112.

Fossen, H. (2016). Structural geology (2nd ed.). Cambridge Univ. Press: Cambridge.

Fry, N. (1979). Random point distributions and strain measurement in rocks. Tectonophysics 60: 89-105.

Galli, P. (1999). Active tectonics along the Wadi Araba- Jordan Valley transform fault. Journal of Geophysical Research 104(B2): 2777-2796.

Garfunkel, Z. (1981). Internal structure of the Dead Sea leaky transform (rift) in relation to plate kinematics. Tectonophysics 80: 81-108.

Genier, F., and Epard, J. L. (2007). The Fry method applied to an augen orthogneiss: Problems and results. Journal of Structural Geology 29: 209-224.

Kassem, O. M. K., and Hamimi, Z. (2018). Finite Strain Analysis of the Wadi Fatima Shear Zone in Western Arabia, Saudi Arabia. Geotectonics 52(2): 251-265.

Khalil, B. (1992). The Geology of Ar Rabba Area, scale 1: 50,000, sheet no .3152- I. Natural Resources Authority, Amman, Jordan.

Klinger, Y., Avouac, J. P., Dorbath, L., Abu Karaki, N. A., Tisnerat, N. (2000). Seismic behavior of the Dead Sea fault along Araba Valley, Jordan. Geophysical Journal International 142: 769-782.

Kumar, R., Srivastava, D. C., Ojha, A. K. (2014). A comparison of the methods for objective strain estimation from the Fry plots. Journal of Structural Geology 63: 76-90.

Lazar, M. (2019). Tectonic Segmentation of the Dead Sea Fault System: A Review of Geophysical Evidence. In Duarte, J.C. (Ed.),Transform Plate Boundaries and Fracture Zones (1st ed., pp. 417- 436). Elsevier.

Lefevre, M., Klinger, Y., Al-Qaryouti, M., Béon, M. L., Moumani, K. (2018). Slip deficit and temporal clustering along the Dead Sea fault from paleoseismological investigations. Scientific Reports 8(1). 4511. DOI: 10.1038/s41598-018-22627-9 PMID: 29540726 PMCID: PMC5851983.

Lisle, R. J. (1985). Geological strain analysis: A manual for the Rf/O method. Pergamon: New York.

Lisle, R. J. (2010). Strain analysis from point fabric patterns: An objective variant of the Fry method. Journal of Structural Geology 32: 975-981.

Long, S., McQuarrie, N., Tobgay, T., Hawthorne, J. (2011). Quantifying internal strain and deformation temperature in the eastern Himalaya, Bhutan: Implications for the evolution of strain in thrust sheets. Journal of Structural Geology 33: 579-608.

Maercklin, N., Bedrosian, P. A., Haberland, C., Ritter, O., Ryberg, T., Weber, M., Weckmann, U. (2005). Characterizing a large shear zone with seismic and magnetotelluric methods: The case of the Dead Sea Transform. Geophysical research letters, 32, L15303

Marshak S., and Mitra G. (Eds.) (1988). Basic methods of structural geology. New Jersey: Prentice Hall.

Mulchrone, K. F. (2013). Fitting the void: data boundaries, point distributions and strain analysis. Journal of Structural Geology 46: 22-33.

Niemi, T. M., Zhang, H., Atallah, M., Harrison, J. B. J. (2001). Late Pleistocene and Holocene slip rate of the northern Wadi Araba fault, Dead Sea Transform, Jordan. Journal of seismology 5: 449-474.

Powell, John H. (1988). The Geology of the Karak Area, scale 1: 50,000, sheet no. 3152- III. Natural Resources Authority, Amman, Jordan.

Ramsay, J. G., and Huber, M. I. (1983). The techniques of modern structural geology: Vol. 1, strain analysis. Academic press: London.

Treagus, S. H., and Treagus, J. E. (2002). Studies of strain and rheology of conglomerates. Journal of Structural Geology24: 1541-1567.

Vollmer, F. W. (2019). Calculation of the best-fit homogeneous strain from a displacement using displacement stretch plot and strain probe theory. Geological Society of America. Abstracts with Programs, 51(5). Doi: 10.1130/abs/2019AM-340051.

Weber, M., Abu-Ayyash, K., Abueladas, A., Agnon, Z., Alasonati-Tašárová, Al-Zubi, H. A., Babeyko,Y. Bartov, K. Bauer, M., Becken, P.A., Bedrosian, Z., Ben- Avraham, G., Bock, M., Bohnhoff, J., Bribach, P., Dulski, J., Ebbing, R., El-Kelani, A., Förster, H.-J., Förster, U., Frieslander, Z., Garfunkel, H.J., Goetze, V., Haak, C., Haberland, M., Hassouneh, S., Helwig, A., Hofstetter, A., Hoffmann-Rothe, K.H., Jäckel, C., Janssen, D., Jaser, D., Kesten, M., Khatib, R., Kind, O., Koch, I., Koulakov, G., Laske, N., Maercklin, R., Masarweh, A., Masri, A., Matar, J., Mechie, N., Meqbel, B., Plessen, P., Möller, A., Mohsen, R., Oberhänsli, S., Oreshin, A., Petrunin, I., Qabbani, I., Rabba, O., Ritter, R.L., Romer, G., Rümpker, M., Rybakov, T., Ryberg, J., Saul, F., Scherbaum, S., Schmidt, A., Schulze, S.V., Sobolev, M., Stiller, D., Stromeyer, K., Tarawneh, C., Trela, U., Weckmann, U., Wetzel, K., Wylegalla. (2009). Anatomy of the Dead Sea Transform from lithospheric to microscopic scale. Reviews of Geophysics 47(2) (RG2002). https://doi.org/10.1029/2008RG000264.

Yamaji, A. (2008). Theories of strain analysis from shape fabrics: A perspective using hyperbolic geometry. Journal of Structural Geology 30: 1451-1465.

JJEES

JJEES (2020) 11 (4): 248-252
ISSN 1995-6681

Jordan Journal of Earth and Environmental Sciences

An Analysis of Rainfall and Discharge Relationship at the River Kilange Catchment, Adamawa State, Nigeria

Dzarma Sayd[1], Ezekiel Yonnana[*1], Aishatu Mubi[2]

[1]Adamawa State University, Department of Geography, Nigeria
[2]Modibbo Adama University of Technology Yola, Department of Geography, Nigeria

Received 17 November 2019; Accepted 9 May 2020

Abstract

Rivers constitute the most important natural water reservoirs from which man derives maximum benefits for economic development. It is therefore not surprising to find most ancient civilizations in the world located around major rivers like the Euphrates, the Tigris and the Nile. This study was undertaken to find out the trends and variability of rainfall and discharge at the River Kilange catchment in Adamawa State, Nigeria. Rainfall and discharge time series data with 27 years observations (1987 to 2013) have been analyzed using the Pearson's Product Moment Correlation. It was found that mean monthly rainfall and discharge were moderately and positively correlated (r = 0.534, P=0.001). Graphical representation of the data in the study area, however, shows a decreasing trend in the annual mean rainfall, but an increasing trend in the river discharge. Improper land management may have been responsible for the strange phenomenon. It is therefore recommended that appropriate land-use management strategies be put in place to curtail further environmental degradation in the River Kilange catchment.

Keywords: Discharge, Kilange, paired samples test, Pearson's Correlation, rainfall.

1. Introduction

The global environmental change phenomenon is becoming more glaring, but there is no clear distinction between the roles played by climatic and anthropogenic factors. Most river catchments in different parts of the world experience a multitude of environmental and water resource-management problems that can be better studied at the river catchment scale. The relationship between rainfall and river discharge are so complicated, and understanding how they interact requires some local studies. This is so, because factors influencing hydrological processes on the earth surface not only vary from time to time, but also over space. As rain falls on the ground it flows through several ways to reach to stream channels, (Suleiman, 2014). The proportion of rainfall that does not evaporate or percolate into the ground flows over the soil surface as surface runoff, whilst the remainder infiltrates through the soil and flows beneath the surface to a stream as sub-surface flow (Nicandrou, 2010). The portion of surface runoff, sub-surface flow, and underground flow, that eventually enters the stream channel and flows, is therein referred to as stream flow or river discharge and that is the focus of this study.

In the Sudan Savannah region of Nigeria where the River Kilange catchment is located, there are two distinct seasons in a year, the dry season and the wet or rainy season. The dry season period is characterised by seasonal water scarcity for both agricultural and domestic use for the population in the study area. Similarly, rainfall received during the wet season often occurs in extreme events, which are usually accompanied by devastating floods, soil erosion, and sedimentation of water courses. This study, therefore, investigates the changing trends in rainfall and river discharge at the River Kilange catchment with the view to understand the environmental problems associated with water resources management in the area.

` In many parts of the world, particularly the developing countries, gauging networks in river catchments are in decline as a result of the lack of financial and human resources, (Margaretha, 2009). In Nigeria, one of the major problems of hydrological studies and water resources planning and management is that of generating adequate hydrological data for use by water resource managers and researchers, (Ezemonye and Emeribe, 2013). The situation has made many researchers in the country abandon hydrological studies in favor of other aspects of the study (Oruonye, 2016). The difficulty encountered in generating or accessing data has made hydrological research very difficult in the country. To overcome this problem of inadequate meteorological and hydrological data, suitable methods of study have to be developed for the river catchments concerned, such as the River Kilange.

In the River Kilange catchment, the only functional gauging station is at Malabu, a settlement located at about 45 kilometres upstream of the River Benue. Long-term stage height data for this station were accessed at the Upper Benue River basin Development Authority, Yola. River discharge data are, however, very sketchy, with only periodic records. Similarly, there is no functional meteorological station in the study catchment. This study, therefore, utilised the rainfall data which is readily available on the Internet.

* Corresponding author e-mail: ezekiel97@adsu.edu.ng

2. The Study Area

The River Kilange catchment covers an area of 4955 km^2 encompassing parts of Fufore, Girei, Gombi, Hong, Maiha, Mubi-North, Mubi-South and Song Local Government Areas of Adamawa state Nigeria. It is located between latitudes 9° 23′ 26'' N to 10° 19′ 00'' N and longitudes 12° 15′ 00' E to 13° 17′ 25'', (Figure 1).

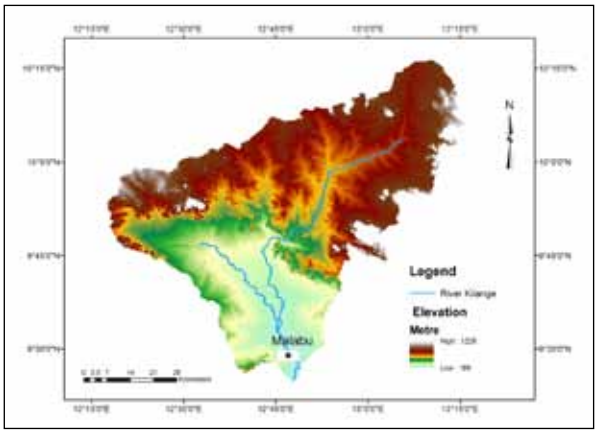

Figure 1. River Kilange Catchment Elevation and Location of the Malabu Gauging Station

Source: Arc-GIS 10 Analysis,

The River Kilange catchment area is underlain by granitic crystalline rocks of the Pre-Cambrian Basement Complex. Overlying the older Basement Complex are the sedimentary and volcanic rocks of a relatively younger age ranging from the upper Cretaceous to Quaternary periods (Bawden, 1972; Frischmann Pell and Partners-PFP-Nigeria, 1981). Elevation in the River Kilange catchment ranges from 169 Metres to 1228 metres above mean sea level as shown in Figure 1. The highest points are confined to the peaks of hills in headwater areas, while the low plains bordering the flood plains of the River Benue into which the River Kilange discharges its water constitute the lowest levels. The major drainage feature in the study area is the River Kilange, which originates from the hills bordering the northern extreme of the catchment. Major tributaries of River Kilange are the Rivers Loko and Song draining the western portion, whereas the eastern part is drained by numerous minor tributaries, prominent among which are Mayo-Nguli and Giraba. The central part of the study catchment is drained by River Sangannare. The River Kilange drains into the River Benue at an outlet near Wuro-Bokki, a settlement located some 45 kilometres upstream of the bridge at Jimeta (Frischmann, Pell &Partners-PFP Nigeria, 1981). The River Kilange catchment lies in the Sub-Sudan climatic zone. The months from May to October constitute the rainy season, while the months from November to April constitute the dry season period. Mean annual rainfall in the study area is about 900 mm based on the Climate Forecast System Reanalysis-CFSR data for the years 1987 to 2013 as shown in Figure 2.

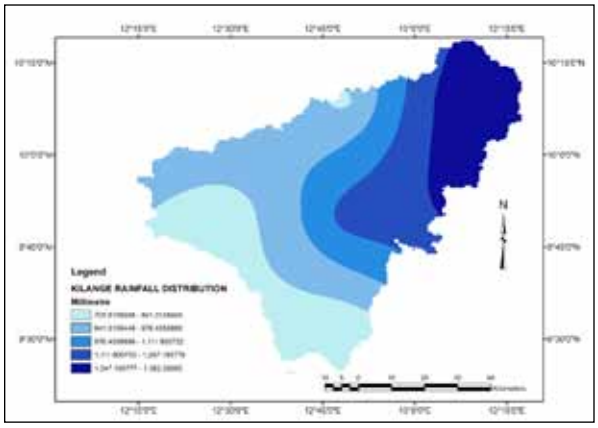

Figure 2. Rainfall Distribution in the River Kilange Catchment

Source: CFSR spell out the acronym

Temperature in the study area is characterized by little diurnal, monthly, and seasonal variations. The hottest month in the year is April, with temperatures rising to 37 °C and 39.6 °C in the northern and southern extremes of the study area respectively (Adebayo and Dayya, 2004). December and January constitute the coldest months as temperatures drop to 15.3 °C and 18.3 °C in the northern and southern extremes of the study area respectively. The dominant soil types in the River Kilange catchment are sandy loam to sandy clay with or without concretionary iron pan. The weakly developed soils of erosion and non-leached ferruginous tropical soils dominate the northern part of the Kilange catchment. These occur as shallow skeletal soils on the upper slopes with deeper colluvial soils in the valleys. The middle portion of the Kilange catchment is dominated by rock outcrops, raw mineral soils, and weakly developed soils of erosion. These are shallow, skeletal soils over granite, basalt, sandstone and ironstone. The southern segment of the Kilange catchment is comprised of sandy loam and clay loam with varying degrees of concretion (Bawden, 1972). Adamawa State and River Kilange catchment inclusive is located within the Sudan Savannah belt of Nigeria (Adefioye, 2013). The natural vegetation of River Kilange catchment is very lightly wooded and is characterized by sparse, relatively short 5-10 metre semi-deciduous trees with shrubs and grasses constituting the dominant cover. The upland areas are characterized by shrub savannah (Frischmann Pell and Partners-PFP-Nigeria, 1981). Near the towns, the native species of trees are gradually being replaced by some exotic species. Agriculture is the major occupation of people in the study area. Two basic patterns of rain-fed agriculture are practiced in the area in relation to the two fundamental soil types, the residual upland pediment soils and alluvial floodplain soils. Maize, guinea corn, cowpea, millet, groundnuts, and cassava are the main crops grown on the upland soils. The alluvial floodplain soils are more fertile than the upland soils and are, therefore more productive and in addition are better supplied with and better able to retain moisture. For these reasons, the floodplains are relatively more extensively cultivated and to a certain extent on a more permanent basis in respect to individual plots. The apparent pattern of cultivation observable in the floodplain areas is that, rice, sugar cane, and banana are planted in the poorly-drained areas, while maize, guinea corn, cassava and a variety of mixed vegetables including onions and okra are

restricted to the better drained sites, (Frischmann Pell and Partners-PFP-Nigeria, 1981).

3. Materials and Methods

There is no conventional weather station in the River Kilange catchment. This study, therefore, used the Climate Forecast System Reanalysis - CFSR daily time series rainfall data of a twenty-seven year period (1987 to 2013) available over the Internet. The monthly mean of the CFSR rainfall was calculated by summing the daily rainfall values for each month of the year and divided by the number of days in that month. Similarly, mean annual rainfall was calculated by summing the monthly mean rainfall for each year divided by the number of months. The CFSR rainfall datasets were for a twenty-seven year period (1987 to 2013). These rainfall datasets were processed in Microsoft Excel Spreadsheet to obtain the mean annual values for the twenty-seven years study period.

The other datasets used in the analysis, are: river stage, stream discharge and the conventional rainfall data which were, therefore, streamlined to the same time period. The Malabu CFSR rainfall station was selected because of its proximity to the Malabu section of the River Kilange, where the river stage and field measurement data were taken for this study.

For a precise estimation of the river flow, the rating curve shall be established and verified based on hydrometric measurements conducted several times per year (Krajewski et al., 2019). Some available records on stream discharge measured through direct methods using flow metre were obtained from the Upper Benue River Basin Development Authority, Yola. Additional flow velocity and flow cross-sectional area were directly measured in the field, and the data were used to validate the historical records. The discharge values were used with recorded gauge height data to develop rating curves. A rating curve was established by simultaneously plotting the values of the water level and river discharge in Microsoft Excel Spreadsheet. This follows the method of Tarpanelli et al. (2013), who suggest that a curve be fitted through the measured hydraulic variables. After plotting the stage versus discharge, a smooth curve was drawn through the plotted points (Figure 3).

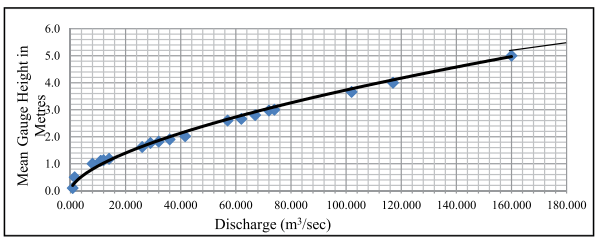

Figure 3. Stage-Discharge Rating Curve for the River Kilange at Malabu

By using the prediction curve, one can simply take the gauge reading and estimate the river discharge (Gnacadja, 2013). The water level records are shown on the 'y' axis, while discharge is on the 'x' axis, and the relationship curve is used to determine the discharge for any given value of water level.

4. Results and Discussion

The mean annual discharge and rainfall time series were analyzed to better understand their relationships and to evaluate the consistency of the data used. The Malabu weather station at which rainfall data were derived through non-conventional measurement methods (Climate Forecast System Reanalysis-CFSR) can be considered fit for meteorological and hydrological analysis. The web-based weather data can be used for analyses, particularly in data-scarce river catchments (Dile and Srinivasan, 2014; Fuka et al., 2013). The CFSR rainfall data for Malabu weather station was used to analyze rainfall-discharge relationship in this study.

Analysis of mean monthly rainfall and discharge at the Malabu section of River Kilange revealed that rainfall is the primary determinant of river discharge in the study area. Although the river is characteristically perennial, the highest values of both rainfall and discharge occur in the months of August and September respectively as shown in Figure 4. The river discharge, though scanty, persists at the Malabu reach of the River Kilange even in the dry season months (January to March and December) when no rainfall is recorded as shown in Figure 4. The dry season discharge is attributed to underground seepage.

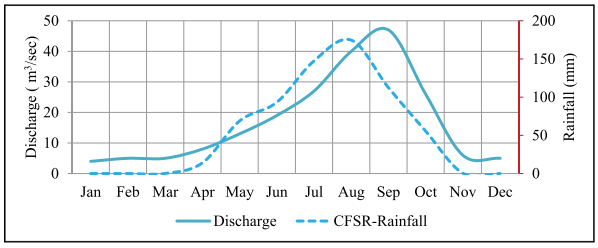

Figure 4. Annual Trend of Rainfall and Discharge at River Kilange Catchment (1987-2013).

The observed seasonal variation in both rainfall and discharge can serve as important information for water resource planning and environmental management in the study area. Annual water scarcity can be predictable since there are distinct dry season months (January to March and November to December). Efforts can, therefore, be made to provide mitigation measures that can reduce the negative impacts of the seasonal water shortages that affect both domestic and agricultural undertakings. Similarly, extreme weather events such as flooding and erosion, which occur in the months of August and September very often, can be predicted based on the depth of rainfall observed. Proactive measures can, therefore, be put in place to reduce the consequences of erosion and flooding that occur at the peak of the rainy season.

Pearson's Product Moment Correlation was used to analyze the relationship between mean annual rainfall and discharge at the River Kilange catchment. The significance of correlation becomes evident when P-value is lower than α (=0.05), and insignificance of correlation becomes evident when P-value is higher than α (=0.05). The result of the correlation analysis was moderate and positive ($r = 0.534$ $P = 0.004$). The correlation is also significant since the P-value (0.004) is less than (0.05). This rainfall-discharge relation

is typical of most tropical rivers, where the influence of ice or snow on the transformation of rainfall to stream flow is negligible or non-existent. Since the correlation analysis between rainfall and discharge, does not exhibit perfect relationship, it can be discerned that other underlying factors apart from rainfall play significant roles in influencing river discharge in the River Kilange catchment. Krajewski et al. (2019) made similar observations, when they affirm that, the distinction between the exact factor driving changes in water resources (land use or climate change), which occur simultaneously in watersheds, are not possible to distinguish with the few variables analyzed. Although it is outside the scope of this study to examine these factors, anthropogenic activities, particularly landuse changes, can partly account for the increase in the river discharge. Therefore, this study suggests that additional causative variables be investigated in the subsequent studies.

Graphical representation of mean annual rainfall and discharge at the River Kilange catchment revealed that there is a steady increase in river discharge during the study period (1987 to 2013) as shown in Figure 5.

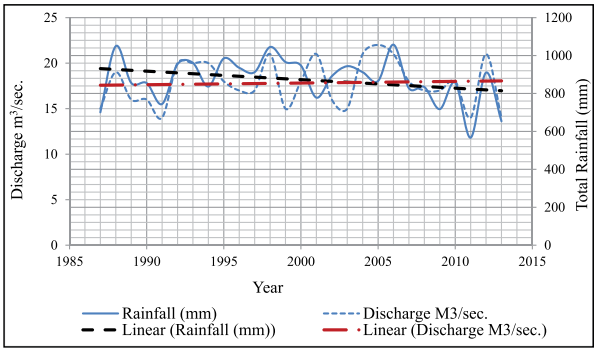

Figure 5. Time Series on Rainfall and Discharge at River Kilange (1987 -2013).

Source: Upper Benue River Basin Authority-UBRBDA, 2018.

The time series of long-term data (1987-2013) have shown that the distributions of rainfall and river discharge have become uneven from the year 2005. The disparity continued steadily to the end of the study period. This finding reveals that a strange environmental phenomenon has started to manifest itself in the Sudan Savanna zone of Nigeria. This strange environmental phenomenon is called the 'Sahelian paradox' because, it was first observed in the Sahel Savannah ecological zone of West Africa, (Amogu et al., 2010). The "Sahelian paradox" is an environmental phenomenon characterized by a steady increase in stream flow without commensurate increase in rainfall. Although the "Sahelian paradox" phenomenon is associated with increase in the total volume of discharge in streams and small rivers, it is characterized by a shorter duration of stream flow (Amogu et al., 2010).

5. Conclusions

The two basic data used in this study are the Climate Forecast System Reanalysis-CFSR rainfall and river discharge estimated from gauge height (water level) records at the Malabu section of the River Kilange. These datasets were used for meteorological and hydrological analyses in the data-scarce River Kilange catchment. The findings of this study indicate that there is close affinity between rainfall and discharge in the River Kilange catchment. Analyses of the long-term data (1987-2013) revealed that rainfall is the primary determinant of discharge in the study catchment. It was however observed that, while the mean annual rainfall showed downward trend, an upward trend was observed in the mean annual discharge over the study period. The changing patterns in rainfall and river discharge can be an indication that water resources are decreasing in the River Kilange catchment. The observed increase in river discharge without commensurate increase in rainfall implies that the catchment loses considerable proportion of rainfall that would have percolated into the ground.

There is thus, the need to provide mitigation measures to reduce the quantity of water lost through excessive stream flow in the study catchment. The impacts of disastrous environmental phenomena such as erosion and flooding can as well be controlled through certain landuse strategies. Earth dams can be constructed to impound excess water during the high flow periods to be used when water is scarce in the dry season. Embankments can also be constructed at appropriate locations to reduce the rate of erosion and flooding during extreme rainfall events. These steps and similar landuse strategies, when put in place, can help considerably in sustaining the environmental resources in the area.

References

Adebayo, A.A., and Dayya, S.V. (2004). Geology, Relief and Drainage: In: Adebayo, A.A. (Ed.), Mubi Region-A Geographical Synthesis, Paraclete Publishers, Yola.

Adefioye, S.A. (2013). Analysis of Land Use/Land Cover Pattern along the River Benue Channel in Adamawa State, Nigeria. Academic Journal of Interdisciplinary Studies 2(5): 95-107. Doi:10.5901/ajis.2012.v2n5p95.

Amogu, O., Luc, D., Kadidiatou, S., Breton, E.L., Mamadou, I., Ali, A., Vischel, T., Jean-Claude, B., Moussa, I.B., Gautier, E., Boubkraoui, S., Philippe, B. (2010). Increasing River Flows in the Sahel? Water 2: 170-199. DOI: 10.3390/w2020170.

Bawden, M.G. (1972). Physiography, Geology, Geomorphology and Hydrology. In: Tuley, P. (Ed.), Land Resources of North East Nigeria. The Environment: Land Resource Study No.9. Surrey, England. Land Resources Division/Overseas Development.

Dile, Y.D., and Srinivasan, R. (2014). Evaluation of CFSR Climate Data for Hydrologic Prediction in Data-scarce Watersheds: An Application in the Blue Nile River Basin. Journal of the American Water Resources Association 50(5): 1226-1241. Doi: 10.1111/jawr.12182.

Ezemonye, M.N., and Emeribe, C.N. (2013). Appraisal of the Hydrological Potential of Ungauged Basin Using Morphometric Parameters. Ethiopian Journal of Environmental Studies and Management 6(4). Doi: 10.4314/ejesm.v6i4.5.

Frischmann Pell and Partners-PFP Nigeria (1981). Kilange River Basin Feasibility Study, Volume IV, Upper Benue River Basin Development Authority, Federal Government of Nigeria.

Fuka, R.D., Walter, M.T., Alister, C.M., Degaetano, A.T., Steenhuis, T.S., Easton, Z.M. (2013). Using the Climate Forecast System Reanalysis as Weather Input Data for Watershed Models, Wiley Online Library.

Gnacadja, L. (2013). Land Degradation: The Hidden Face of Water Scarcity, Harvard.

Krajewski, A., Sikorska-Senoner, A.E., Ranzi, R., Banasik,

K. (2019). Long-Term Changes of Hydrological Variables in a Small Lowland Watershed in Central Poland. Water 11(3), 564; https://doi.org/10.3390/w11030564.

Margaretha, L. M. (2009). Understanding Hydrological Processes in an Ungauged Catchment in Sub-Saharan Africa, Ph.D Thesis, Delft University of Technology, the Netherlands.

Nicandrou, A. (2010). Hydrological Assessment and Modelling of the River Fani Catchment, Albania, Ph.D. Thesis, University of South Wales.

Oruonye, E. D. (2016). Morphometry and Flood in Small Drainage Basin: Case Study of Mayogwoi River Basin in Jalingo, Taraba State Nigeria. Journal of Geography, Environment and Earth Science International 5(1): 1-12.

Suleiman, Y. M. (2014). Surface Runoff Responses to Rainfall Variability over the Bida Basin, Nigeria. Journal of Environmental and Earth Sciences 4(3): 67-74.

Tarpanelli, A., Barbetta, S., Brocca, L., Moramarco, T. (2013). River Discharge Estimation by Using Altimetry Data and Simplified Flood Routing Modeling. Remote Sensing 5(9): 4145-4162.

Upper Benue River Basin Development Authority-UBRBA, (2018). Yola, Adamawa State, Nigeria.

JJEES

JJEES (2020) 11 (4): 253-259
ISSN 1995-6681

Jordan Journal of Earth and Environmental Sciences

Geotechnical Evaluation of South Jordan Basaltic Rocks for Engineering Uses

Suhail Sharadqah[1], Reyad A. Al Dwairi[1*], Mazen Amaireh[1], Hani Nawafleh[2], Omar Khashman[3], Aiman E. Al-Rawajfeh[1],Soraya M. Perez[1]

[1]*Tafila Technical University, Faculty of Engineering, Natural Resources and Chemical Engineering Department, Jordan.*
[2]*Al-Hussein Bin Talal University, Faculty of Engineering, Mining and Minerals Engineering Department, Ma'an, Jordan.*
[3]*Al-Hussein Bin Talal University, Faculty of Engineering, Environmental Engineering Department, Ma'an, Jordan.*

Received 30 July 2019; Accepted 26 May 2020

Abstract

Jordanian basaltic rocks (JB) are highly distributed and available in huge quantities in northeastern, central, and southern Jordan. The objective of this study is to determine the geotechnical properties and those relevant to engineering of JB from southern Jordan, which is related to the Tertiary- Quaternary continental basaltic flows and to conduct a comparison of the results with the standard specifications. Ten random samples of southern Jordan basalt (SJB), were collected representing ten locations.

The laboratory investigation included measurements of point load strength, splitting tensile strength (MPa), Los Angeles, abrasion value (%), slake durability, abrasion, porosity, and saturation degree. In addition, the chemical and mineralogical composition of the basalt was identified utilizing X-ray fluorescence (XRF), and X Ray Diffraction respectively.

The X- Rays show that the studied basalt is mainly composed of clinopyroxene, plagioclase and feldspar; also, olivine is available in significant amounts. Iron oxides (magnetite and ilmenite), iron-titanium oxides (Titanium-augite, sphene) and spinel are present in relatively minor amounts

In terms of the SiO_2 contents, the samples from the SJB range from about 41.08% to 46.2%, while the Al_2O_3% values range from about 11.95% to 14.25%. The Fe_2O_3% values range from 2.3% to 5.22 % and FeO% from about 0.12 % to 0.16 %. MnO% values range from 0.12 % to 0.16%, MgO% from 8.71 % to 10.1%, CaO%, from 9.95 % to 12.05%, Na_2O% from 2.18% to 3.9%, K_2O% from 0.1% to 1.16%, and TiO_2% from 2.35 % to 2.9%. In general, SiO_2 contents are relatively low (< 50%); accordingly, the potential for alkali silica reaction (ASR) is very low.

The results of properties related to engineering indicate that SJB has compressive strength values ranging from 96 to 154 Mpa. Los Angles Abrasion ranges between 3.68% and 4.85%, and splitting tensile strength (MPa) is between 2.345 and 3.291 Mpa. Slake durability (Id1) ranges between 99.14 and 99.42, while slake durability (Id2) falls between (99.05 and 99.34).. The rest of the results were as follows: Voids (0.0112 to 0.029); porosity (1.11 to 2.82)%; water content% (0.16- 0.34)%; saturation % (28 to 55)%, while average dry specific gravity was 2.82.

The results show that the basalt of the southern Jordan area (SJB) complies with the international standards, and the standards used for classifying the decorative and building stones. Therefore, this study recommends the use of SJB as a promising raw material to produce building aggregates.

Keywords: Basalt, South Jordan, Geotechnical, Building stones, Engineering properties.

1. Introduction

Basalt is one of the most common igneous rocks in the world. It is a crystalline basic igneous volcanic black rock which is sometimes glassy. Basalt is widespread in seafloor crust, oceanic islands, continental volcanoes, and flood plateau lavas. It is primarily recognized by its dark color. Mineralogically, it is composed of the following main primary rock forming minerals: Plagioclase, Feldspar, Pyroxene, and Olivine.

Basalt-based materials are environmentally friendly and not hazardous and can be utilized in many industrial applications. The applications are based on the basic quality properties such as high abrasion resistance, compressive strength, and chemical resistance.

Basaltic rocks are used extensively as engineering materials including aggregates for Portland cement concrete and asphaltic concrete, and rock fill for dams and breakwaters. It can be utilized also as material for railroad ballast and highway base courses (Goodman, 1993).

The main objective of the present study is to assess the general suitability of the basalt as a coarse aggregate for concrete mixes and/or as a cut stone for industrial uses.

The quality properties of the basaltic rocks vary from

* Corresponding author e-mail: reyadn@hotmail.com

place to another depending on their origin and weathering state and more significantly on the geological occurrence.

The basaltic rocks in Jordan (JB) are distributed in three main regions based on their mode of occurrence: NE-Jordanian, within the Jordan rift and in central Jordan (Bender, 1974; Al Malabeh, 1993). The age of JB is mainly of Tertiary-Quaternary (Bender, 1974).

During Cenozoic times, basaltic lava poured from vertical fissures and local vents along the Jordan rift, and mountain ridges in central and northeastern Jordan (Fediuk and Al-Fugha, 1999).

Al Dwairi (2007) studied the zeolites associated with these eruptions and classified them into three areas: North east, Central and south Jordan. South Jordan basalt (SJB) is located within the basaltic eruptions along the arched eastern rim of Jordan graben south of Jordan (Bender, 1974). The south Jordan volcanic eruptions belong to volcanic eruptions in northeastern Jordan (Harrat Ash Shaam) (Ibrahim, 1987 and Ibrahim et al., 2003). In southern Jordan, the basaltic rocks are distributed as isolated eruptions associated with volcanic cones. Basalt in southern Jordan is found representatively in ten areas, the most important are Tell Burma, Jabel uneiza and wadi Hisa (MEMR, 2015).

The SJB eruptions occur either as local flows or as individual volcanic bodies, i.e. cones, plugs, sills, and dikes (MEMR, 2015). The studied area is located within the Tafila District as isolated basalt effusions, tectonically controlled by the Arabian plate movement, which moved northwards along the Dead Sea Transform fault (Barberi et al., 1979).

Many researches dealt with basalt frequently focusing on the geneses, geology, mineralogy, petrology, and the distribution of basalts flows in Jordan (Bender, 1974; Ibrahiem, 1987; Al-Malabeh, 1993; Al Dwairi and Shardqah, 2014; Al Dwairi, 2019). Also, many researches rendered special care to the natural zeolite which is normally related to basaltic eruptions in Jordan (Al Dwairi, 2007; Al Dwairi, 2009; Al Dwairi, et al., 2009; Sharadqah and Al Dwairi, 2010; Al Dwairi and Al-Rawajfeh, 2012; Al Dwairi et al., 2014; Al Dwairi et al., 2015; Khoury et al., 2015; Al Dwairi, 2017). However, only little work and few studies have paid attention to the engineering and geotechnical characteristics of Jordanian basalts (Abu-Mahfouz et al., 2016; Al Dwairi et al., 2018).

This research deals with the investigation of the engineering and geotechnical properties of SJB which will be evaluated to determine their engineering applications. Therefore, this study was carried out to investigate and evaluate the main physical and mechanical properties of south Jordan basalt and its suitability as a construction material.

2. Study Area

The study area is located in southern Jordan, and included ten locations as presented by the geological map in Figure 1

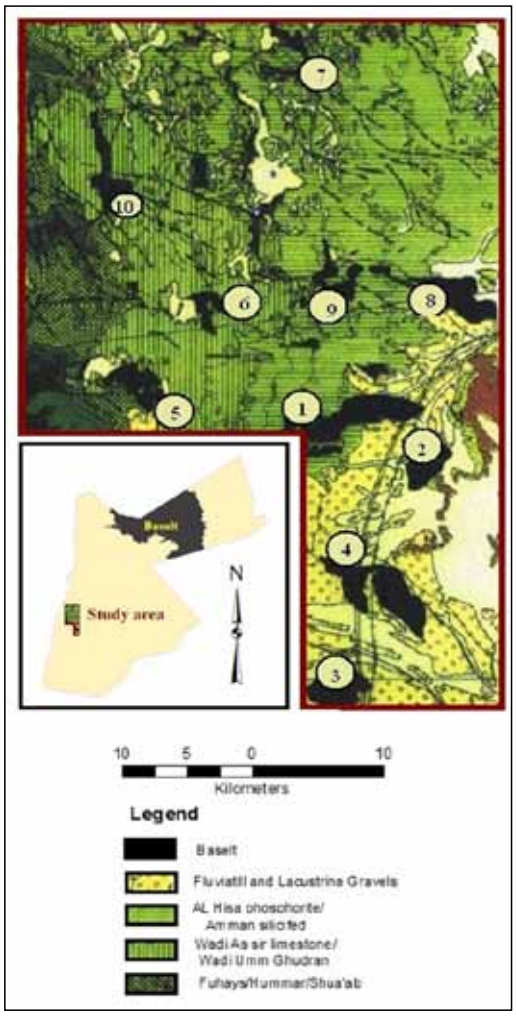

Figure 1. Location map of the southern Jordan basaltic tuff (moderfied after Mehyar and Madanat, 2015).

3. Materials and Methods

3.1. Material Source

To carry out the research, ten basaltic samples were selected from southern Jordan. From each selected site, more than 100kg fresh bulk samples have been collected; the coordinates of the sampling sites are given by Table 1.

Table 1. Coordinates of the sampling sites.

Sample #	Location	Sample Name	Longitude(N)	Latitude(E)	Elevation(m)
1	Tall Juhira	SJB 1	30° 38'47"	35°49'37"	1355
2	Tall Burma	SJB 2	30° 37'23"	35°49'43"	1077
3	Uneiza	SJB 3	30°29'42"	35°47'30"	1144
4	Tall Amir	SJB 4	30°33'05"	35°47'58"	1049
5	Al Taata	SJB 5	30°42'34"	35°42'03"	1462
6	Al Harer	SJB 6	30°52'09"	35° 41'56"	1579
7	Al Alia	SJB 7	30°55'09"	35°48' 19"	1058
8	Jurf El Daraweesh	SJB 8	30°42'16"	35°53'09"	1281
9	Huliat El Gran	SJB 9	30° 43'07"	35° 53'34"	1336
10	Al Hala 1	SJB 10	30° 46'19"	35° 38'33"	1525

3.2. Methods and Tests

The suitability for usage as materials for engineering purposes depends principally on the physical and mechanical properties of the basalt; although for some applications, mineralogical or chemical properties are also required. The British Geological Survey, 1994. The American Society for Testing and Materials (ASTM), and the International Society of Rock Mechanics (ISRM), have devised a wide range of tests to assess materials and their value and potential and performance. These properties include specific gravity, density, water content, void ratio, absorption, degree of saturation, Los Angeles Abrasion, slake durability indices, point load index, and ultrasonic velocity. Following is a brief description of some of these properties tested in this study.

The mineralogy of basaltic rocks (SJB), was identified using X Ray Diffraction according to Al Dwairi, 2007, while the chemical composition of SJB was determined using X - Ray Fluorescence (XRF) available at the laboratory of the Mining Engineering Department, at Al-Hussin Bin Talal University (Jordan).

The physical characteristics of basaltic rocks (SJB) were determined in the laboratory. The rock specimens were prepared from rock block samples collected from the investigated representative sites.

The mechanical characteristics include Point load test (PLT), splitting tensile strength, the Los Angeles Abrasion Test. Slake Durability tests were also carried out according to the ASTM or AASHTO standards.

The physical characteristics of SJB, including Void ratio (e), porosity (n), water content, and water saturation, were evaluated utilizing ISRM, X.1979, Specific Gravity ASTM D 854, and Bulk Density Crawford, 2013.

The porosity (n) is defined as the proportion of void volume to total volume (equ. 1), and the void ratio (e) is the proportion of void volume related to that of solid volume (equ. 2). Porosity and void ratios were evaluated by estimating the bulk dry density and the specific gravity of the ground material. The saturation degree refers to the proportion of pores filled by water according to equation 3. The unit weight values are given by equation 4.

$$\boldsymbol{Porosity\ (n)} = \frac{Vp}{Vt} \textit{Equation 1}$$

Where:

Vp: is the volume of space

Vt: is the total volume

$$\boldsymbol{VoidRario(e)} = \frac{Vp}{Vs} \text{Equation 2}$$

Where:

Vp: is the volume of space

Vs: is the volume of solids

$$\boldsymbol{Sturation\ Degree\ (S)} = \frac{Vw}{Vv} \boldsymbol{X\ 100\%}\ \textit{Equation 3}$$

Where:

Vw: is the volume of water

Vv: is the volume of voids

$$\boldsymbol{\gamma\ dry} = \frac{\gamma\ wet}{1+w} \textit{Equation 4}$$

Where:

γ: is the unit weight

w: is the water content in the rock sample (dry weight bases)

Point Load Test (Is50):

To determine the mechanical strength of the rock, a point-load strength test was performed according to the recommendations of the ASTM D5731 – 16, for blocks of irregular geometry. The value for Is (50) (Point load strength index for 50 mm diameter core) is determined with the equivalent core diameter of the specimens. Early studies (Broch and Franklin, 1972), and Miller, 1965, were conducted on hard strong rocks, and found that the relationship between UCS and the point load strength could be expressed as follows.

$$\boldsymbol{USC = K(Is50) = 24.5\ (Is50)} \textbf{Equation 5}$$

Where:

UCS: Unconfined Compressive Strength (Mpa)

K: conversion factor

Is50: point load strength corrected to a diameter of 50mm

A recent study by Sharo and Tawaha, 2019 conducted on thirty samples of Jordan basalt investigated the relationship between the uniaxial compressive strength (UCS) and the point load index (PLI, indicated for K= 23.52

$$\boldsymbol{UCS = 23.52\ (Is\ 50)} \textbf{Equation 6}$$

In general, the results agreed well with earlier studies. The obtained measurements of (Is 50), were converted to UCS utilizing equation 5.

Splitting Tensile Test was conducted according to ASTM D3967-016, by extracted core samples, 50 mm diameter and 25mm length. The splitting tensile strength (σt) of each sample was calculated by equation 7 for each sample.

$$\delta t = \frac{2P}{\pi LD}$$ **Equation 7**

Where:

σt = splitting tensile strength, MPa

P = maximum applied load indicated by the testing machine in

L = length of the core sample, in (mm)

D = Sample diameter in (mm)

Slake Durability Test (SDT): the test was performed in accordance with ASTM D4644; two cycle testes have been elaborated; each for ten minutes and at a speed of thirty revolutions/minute in a water bath. The percentage of dry mass, which remained in the drum of the original mass after one cycle, is reported as Id1, and the percentage of dry mass, which remained in the drum after two cycles, is reported as Id2.

Los Angeles Abrasion test: the test was carried out according to AASHTO 96 T. For each basaltic source, the samples were prepared for A- grade, while considering the sample weight of 5kg. The prepared samples were subjected to 500 hundred revolutions at a speed of 30 revolutions/ minute. The reported value of Los Angles Abrasion is the result of equation 8.

$$Av = \frac{m1-m2}{m1x100\%}$$ **Equation 8**

Where:

Av: is Abrasion Value

m1: original sample mass (g)

m2: final sample mass (g)

4. Materials and Methods

4.1. Mineralogical and Chemical Composition

The mineralogical investigation indicates that the studied basaltic rocks were mainly composed of clinopyroxene, plagioclase and feldspar; also, olivine is available in significant amounts. Iron oxides (magnetite and ilmenite), iron-titanium oxides (Titanium-augite, sphene) and spinel were present in relatively minor amounts as indicated in the XRD results (Figure 2).

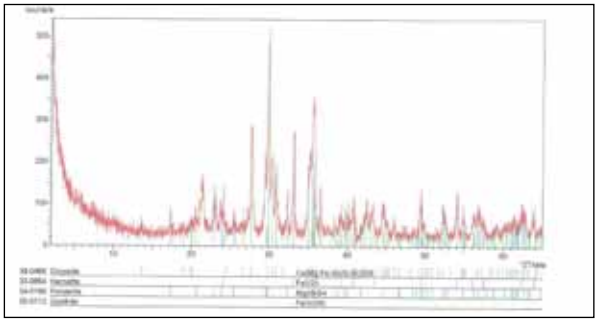

Figure 2. X ray diffraction pattern example for SJB.

The mineralogical investigation indicates that the studied basaltic rocks were mainly composed of clinopyroxene, plagioclase and feldspar; also, olivine is available in significant amounts. Iron oxides (magnetite and ilmenite), iron-titanium oxides (Titanium-augite, sphene) and spinel were present in relatively minor amounts as indicated in the XRD results (Figure 2).

Table 2. Chemical composition of the samples from SJB

Sample Name	SiO_2%	Al_2O_3%	Fe_2O_3%	FeO%	MnO%	MgO%	CaO%	Na_2O%	K_2O%	TiO2%
SJB 1	43.5	13.98	3.50	7.67	0.13	8.75	10.30	2.75	0.98	2.40
SJB 2	44.15	14.25	4.10	8.34	0.14	8.90	9.95	2.60	1.08	2.57
SJB 3	42.35	13.70	2.30	9.20	0.12	8.71	10.60	3.10	0.95	2.90
SJB 4	42.80	14.00	5.22	8.50	0.16	9.21	11.53	2.30	0.90	2.60
SJB 5	45.20	13.01	3.89	7.98	0.15	10.10	10.50	3.20	1.15	2.75
SJB 6	41.08	13.00	3.20	8.20	0.15	9.57	11.09	2.18	0.85	2.58
SJB 7	42.07	14.15	4.60	6.85	0.14	8.90	11.90	3.50	1.05	2.59
SJB 8	43.61	11.95	4.00	6.95	0.15	8.95	12.05	3.90	1.16	2.35
SJB 9	41.24	12.77	3.80	7.23	0.14	9.21	11.80	2.90	0.96	2.45
SJB 10	46.20	13.77	4.45	8.45	0.14	9.05	10.87	2.85	0.10	2.40
Average (%)	43.22	13.458	3.906	7.937	0.142	9.135	11.059	2.928	0.918	2.559

According to Le Bas et al. (1986), diagram (Figure 3), the composition of the samples reflects Ultra Basic – Basic (Basanite and Basalt)

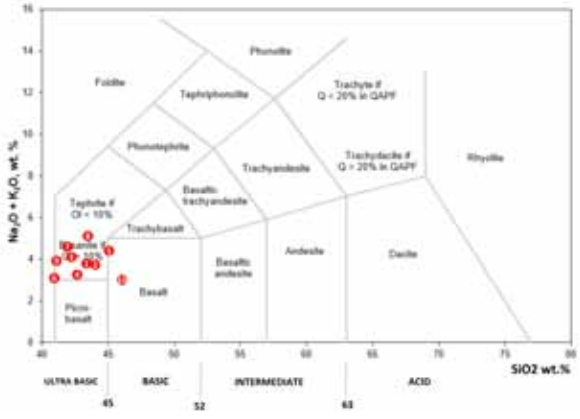

Figure 3. Classification of the Basalt according to Le Bas et al. (1986).

Katayama et al. (1989) pointed out that where the silica content of bulk composition exceeds 50%, basalt may have a potential for alkali silica reaction (ASR). According to the chemical analysis, all the samples have less than 50% SiO_2; accordingly, their potential for alkali silica reaction (ASR) is very low.

4.2. Geotechnical Characteristics

The results of geotechnical properties of the collected samples are listed in Table 3. The values reported in the tables are the averages of several replicate tests, compressive strength values

Unconfined compressive strength (UCS) ranges from 96 to 154 Mpa, with an average of 125.6 Mpa, Using the classification system proposed by Deere and Miller (1966), the examined basalt rocks of the studied areas can be considered as a (C) classification having a medium strength rock (55-110) Mpa.

Slake Durability was reported after the first cycle (Id1) between 99.14 and 99.42, and for the second cycle (Id2) between (99.05 and 99.34). Following Gamble (1971), the classification index for durability after the first cycle (Id1) was more than 99 % and after the second Sycle (Id2), it was more than 98 %, which indicates a very durable basalt.

Los Angeles Abrasion Value (%): The Los Angeles abrasion values (after 500 cycles) range between 3.68% and 4.85% with an average of 4.03%, which indicates a high resistance to abrasion According to IS: 2386 (Part 4), the aggregate impact value should not exceed 45% for aggregate used for concrete other than for wearing surface, while the aggregate impact value should not exceed 35% for concrete used for wearing surfaces such as runways, roads, pavements, floors etc.

Splitting Tensile Strength (MPa): The results of Splitting Tensile Strength (MPa) range between 2.345 and 3.291 Mpa, with an average of 2.94 Mpa.

Table 3. Average of geotechnical characteristics of the basalt samples

Location #	Unconfined compressive strength (MPa)	Splitting Tensile Strength (MPa)	Los Angeles Abrasion Value (%)*	Slake durability	
				I_{d1}	I_{d2}
JB 1	143	2.345	3.73	99.31	99.26
JB 2	135	3.127	3.68	99.28	99.17
JB 3	117	2.813	3.84	99.30	99.23
JB 4	136	2.919	3.97	99.19	99.05
JB 5	128	3.158	4.2	99.14	99.11
JB 6	154	3.291	4.27	99.16	99.10
JB 7	96	2.871	4.85	99.42	99.31
JB 8	124	3.189	3.68	99.41	99.34
JB 9	116	2.910	3.87	99.39	99.33
JB 10	107	2.781	4.18	99.17	99.10
Average	125.6	2.94	4.03	99.28	99.2

4.3 Physical Characteristics

The analysis of the physical characteristics of the basaltic samples shown in Table 4 revealed the following results:

Bulk density range was (2.73- 2.92) g/cm^3, with an average of 2.82 g/cm. Based on the IAEG 1982 criteria, the basalt rock samples from two locations (SB-8 &SB-9) were classified as class -4, high density (2.5-2.75) g/cm. As for the samples from the other locations, they are classified as class -4 very high density (Over 2.75) g/cm^3.

Specific Gravity: The Specified gravity values reported for the samples were within the range (2.76-2.98) g/cm^3, with an average of 2.86 g/cm.

Porosity (%) was found within the range of (1.11-2.82) %, with the average 1.6 %. According to the IAEG 1982 criteria, the basaltic rocks from ten locations were located within Class -4 (Low Porosity).

Water content (%) falls within the range of (0.16 to 0.34) %, with an average of 0.24 %. Saturation (%) was reported within the range of (28-55) %, with an average of 39.1%.

Table 4. Average of geotechnical characteristics of the basalt samples

Location #	Specific Gravity	Bulk Density	Void ratio	Porosity (n)	Water content	Saturation
	(g/cm^3)	(g/cm^3)	(e)	%	%	%
JB 1	2.98	2.92	0.017	1.67	0.22	35
JB 2	2.86	2.83	0.0119	1.18	0.17	37
JB 3	2.92	2.86	0.02	1.96	0.21	28
JB 4	2.86	2.85	0.0145	1.43	0.16	29
JB 5	2.87	2.82	0.0164	1.61	0.32	51
JB 6	2.92	2.84	0.029	2.82	0.34	31
JB 7	2.86	2.84	0.0146	1.44	0.27	48
JB 8	2.76	2.73	0.0112	1.11	0.16	36
JB 9	2.79	2.75	0.0156	1.54	0.25	41
JB 10	2.80	2.77	0.0130	1.28	0.28	55

Generally, the values are comparable to those of late tertiary and early quaternary basalt which is the case in this study (Abu-Mahfouz et al., 2016, Mehyar and Madanat 2015). It is notable that results of all samples have the same pattern of variability for all locations and for all tests. A similar wide range of measurement values for different samples from the same location has been reported in (González de Vallejo et al., 2008).

The Porosity is mainly due to vesicles; however, the relatively high saturation may indicate some secondary porosity. Secondary porosity tends to connect parts of these vesicles, which is enabling water to move and fill the vesicles. Figure 4 shows a reverse relationship between saturation degree and UCS, where the R^2 is more than 35%.

Saturation degree also seems to have some relation with the geographical distribution. In the sites toward the east were the desertic conditions are more severe and the precipitation is more limited, the saturation degree tends to be low. In contrast, in the western basaltic flow exposures, the saturation degree is mostly higher. All these relations support the hypothesis that the variation in the physical and geotechnical index properties between different basalt locations in the study area may be attributed to the weathering processes rather than to the basalt geneses. Despite all that has been discussed above, the basalt from all locations in the study area still a high similarity from the geotechnical point of view. Basalts of the study area is of a high quality for common usage, such as aggregates.

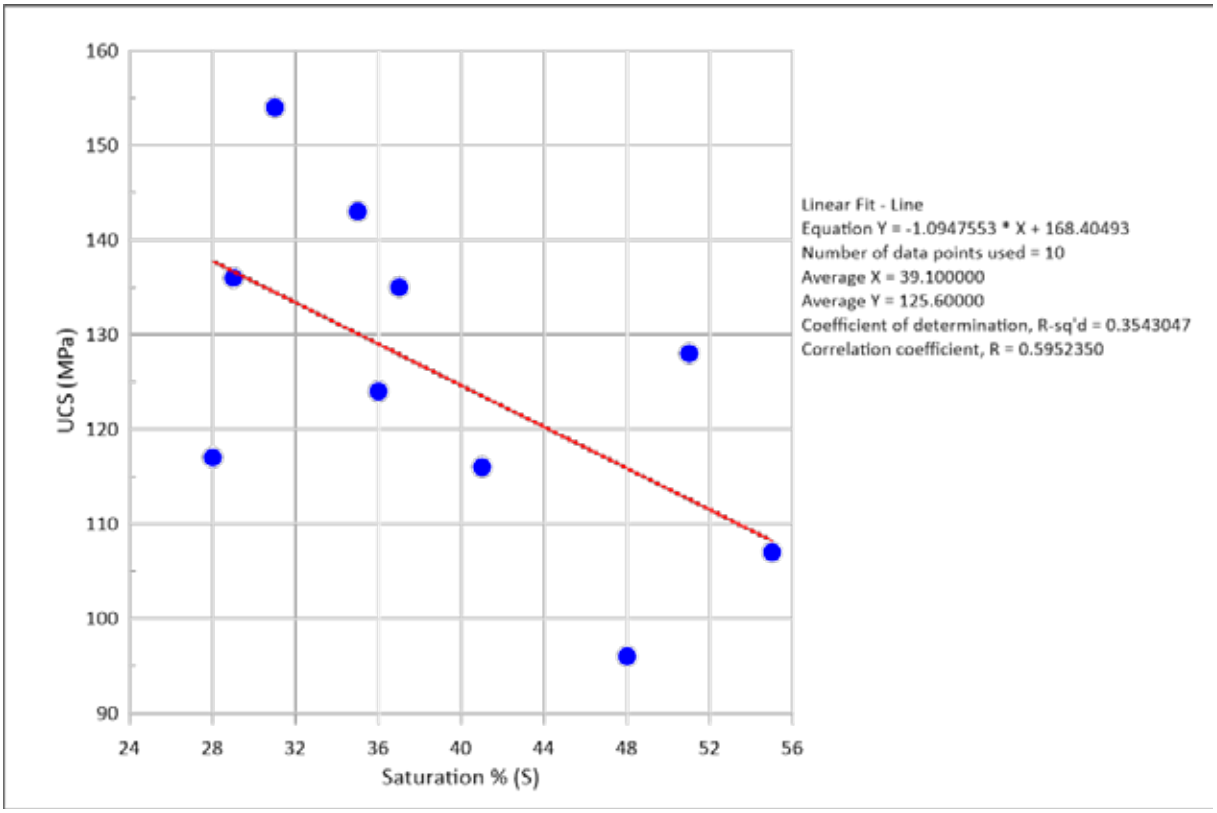

Figure 4. Relationship between the UCS and Saturation degree.

5. Conclusions

Based on the comprehensive analysis of the test results and the chemical analysis, the potential of the Basalt of South Jordan for alkali silica reaction (ASR) is very low. Moreover, based on the review of all the mechanical and physical tests of the samples from the ten locations, the results show that the SJB meets the requirements and specifications of the ASTM or AASHTO standards specified for construction materials; accordingly, SJB can be used as a promising construction material.

References

AASHTO, American Association of State Highway and Transportation.

Abu-Mahfouz, I., Al-Malabeh, A., Rababeh, S. (2016). Geo-engineering evaluation of Harrat Irbid Basaltic Rocks, Irbid District—North Jordan. Arab Journal of Geoscience 9: 28-40. https://doi.org/10.1007/s12517-016-2428-4

Al Dwairi, R. (2017). Modeling of Chromium (VI) Adsorption from Aqueous Solutions Using Jordanian Zeolitic Tuff. Water Science and Technology 75: 2064-2071.

Al Dwairi, R. (2019). Mineralogical and Geochemical Characterization of Jordanian Olivine and Its Ability to Capture CO2 by Mineralization Process Indonesian Journal on Geoscience 6: 175-183.

Al Dwairi, R. (2009). The use of expendable local zeolite deposits for NH4 removal in municipal wastewater. Jordan Journal of Civil Engineering 3: 256–264.

Al Dwairi, R. (2007). Characterization of the Jordanian zeolitic tuff and its potential use in Khirbet es Samra wastewater treatment plant. Unpublished PhD Thesis, The University of Jordan, Amman, Jordan 185 P.

Al Dwairi, R. and Al-Rawajfeh, A. (2012). Recent Patents of Natural Zeolites Applications in Environment, Agriculture and Pharmaceutical Industry. Recent Patents on Chemical Engineering 5: 20-27.

Al Dwairi, R., Ibrahim, K., Khoury, H. (2014). Potential use of faujasite–phillipsite and phillipsite–chabazite tuff in purification of treated effluent from domestic wastewater treatment plants. Environmental Earth Sciences 71: 5071-5078.

Al Dwairi, R., Khoury, H., and Ibrahim, K. (2009). Mineralogy and Authigenesis of Zeolitic Tuff from Tall-Juhira and Tall Amir, South Jordan. Jordan Journal of Earth and Environmental Sciences 2: 81- 88.

Al Dwairi, R., Omar W., Al-Harahsheh, S. (2015). Kinetic modelling for heavy metal adsorption using Jordanian low-cost natural zeolite (fixed bed column study). Journal of Water Reuse and Desalination 5(2): 231-238.

Al Dwairi, R.and Sharadqah, I. (2014). Mineralogy, geochemistry and volcanology of volcanic tuff rocks from Jabal Hulait Al_Gran, South of Jordan (New Occurrence). Jordan Journal of Civil Engineering 8: 187-198.

Al Dwairi, R., Al Saqarat, B., Shaqour, F., Sarireh, M. (2018). Characterization of Jordanian Volcanic Tuff and its potential use as lightweight aggregate. Jordan Journal of Earth and Environmental Sciences 9: 127-133.

Al Malabeh, A. (1993). The Volcanology, Mineralogy, and Geochemistry of Selected Pyroclastic Cones from NE Jordan and Their Evaluation for Possible Industrial Applications. PhD Thesis, Universitat Erlangen. 300 p.

ASTM C 330-89, "Standard Specification for Lightweight Aggregates for Structural Concrete", Annual Book of ASTM Standards, 4.02: 193- 195.

Barberi, F., Capaldi, P., Gasperini, G., Marineli, G., Santacroce, T., Scndone, R., Treuil, M., Varet, J. (1979). Recent basaltic volcanism of Jordan and its implications on the geodynamic history of the Dead Sea Shear Zone. International Symposium Geodynamic Evolution Afro-Arabian Rift System, Rome, 667-682.

Bender, F. (1974). Geology of Jordan. Contributions to the Regional Geology of Earth 7. Gebrüder Borntraeger, Berlin (Supplement pp. 196).

Broch, E. and Franklin, J.A. (1972). The Point-Load Strength Test. International Journal of Rock Mechanics and Mining Sciences 9: 669-697. https://doi.org/10.1016/0148-9062(72)90030-7.

Crawford, K. (2013). Determination of Bulk Density of Rock Core Using Slandered Industry Methods Dissertations, Master's Theses and Master's Reports - Open. Michigan Technological University. P 192.

Deere, D. and Miller, R. (1966). Engineering classification and index properties for intact rock. Tech. Report No AFWL - TR-65-116, Air Force Weapons Lab., Kirtland Air Base, New Mexico.

Fediuk, F. and Alfugha, H. (1999). Dead Sea Region: Fault-controlled chemistry of Cenozoic Volcanics. Geolines 9: 29–34.

Gamble, J. C. (1971). Durability-Plasticity Classification of Shales and Other Argillaceous Rocks, Th. D. Thesis, University of Illinois at Urbana-Champaign.

González de Vallejo, LI., Hijazo, T., Ferrer, M. (2008). Engineering geological properties of the volcanic rocks and soils of the Canary Islands. Soils and Rocks 31: 3–13.

Goodman, RE. (1993). Engineering Geology Rock in Engineering Construction. Wiley, New York.

Ibrahim, K. M. (1987). Geochemistry and petrology for some of the basaltic outcrops in central Jordan. M. Sc. Thesis, University of Jordan, Amman, 164.

Ibrahim, K. M., Tarawneh, K., Rabba', I. (2003). Phases of activity and geochemistry of basaltic dike systems in northeast Jordan parallel to the Red Sea. Journal of Asian Earth Science 21: 467-472.

Katayama, T., St John, DA., Futagawa, T. (1989). The petrographic comparison of some volcanic rocks from Japan and New Zealand - potential reactivity related to interstitial glass and silica minerals. In: Okada, K, Nishibayashi, S, Kawamura, M (Eds.), Proceedings of the 8th International Conference on Alkali-aggregate Reaction in Concrete (ICAAR), Kyoto, Japan. CRC Press, Boca Raton/FL: 537–542.

Khoury, H. N., Ibrahim, H., Al Dwairi, M., Torrente, R. (2015). Wide spread zeolitization of the Neogene – Quaternary volcanic tuff in Jordan. Journal of African Earth Sciences 101: 420–429.

Le Bas, M.J., Lemaitre, R.W., Streckeisen, A., Zanettin, B. (1986). A Chemical Classification of Volcanic-Rocks Based on the Total Alkali Silica Diagram. Journal of Petrology 27(3): 745-750. https://doi.org/10.1093/petrology/27.3.745.

Mehyar, N. and Madanat, M. (2015). Mineral Status and Future Opportunity: Basalt. Ministry of Energy and Mineral Resources. Amman, Jordan, Pp 11.

Miller, R.P. (1965). Engineering classification and index properties for intact rock, Ph.D. Thesis, University of Illinois. Reported in Richard Goodman, introduction to rock mechanics.

Ministry of Energy and Mineral Resources (MEMR) (2015). Basalt, Mineral Status and Future Opportunity

Sharadqah, S., and Al Dwairi, R., (2010). Control of Odorants Emissions from Poultry Manure Using Jordanian Natural Zeolites. Jordan Journal of Civil Engineering 4: 378-388.

JJEES

JJEES (2020) 11 (4) 260-271
ISSN 1995-6681

Jordan Journal of Earth and Environmental Sciences

Assessing the Impact of Zaatari Syrian Refugee Campin Central North Jordan on the Groundwater Quality

Sura Al-Harahsheh[1], Ahmed A. Al-Taani[2,3],*, Hani Al-Amoush[1], Akram Shdeifat[4], Atef Al-Mashagbah[5], Marwan Al-Raggad[6], Raya Al- Omoush[4], Hassan Al-Kazalah[4], Maher Hraishat[7], Refaat Bani-Khalaf[7] , Khaled Almasaeid[8]

[1]1Al Al-Bayt University, Institute of Earth and Environmental Sciences, Department of Earth and Environmental Sciences, Jordan.
2Yarmouk University, Faculty of Science, Department of Earth and Environmental Sciences, Jordan.
3Zayed University, College of Natural and Health Sciences, Department of Life and Environmental Sciences, United Arab Emirates.
4Al al-Bayt University, Water, Environment and Arid Regions Research Center, Jordan.
5Al al-Bayt University, Institute of Earth and Environmental Sciences, Department of Geographic Information System and Remote Sensing, Jordan.
6University of Jordan, Water, Energy and Environment Center, Jordan.
7Ministry of Water and Irrigation, Jordan. 8 The Higher Council for Science and Technology, Badia Research program, Jordan.

Received 4 March 2020; Accepted 29 May 2020

Abstract

Zaatari Refugee Camp is the largest Syrian camp in Jordan with about 80,000 inhabitants. It was established in 2012 following the Syrian conflict. This refugee camp has been a constant source of concern to public authorities and local communities because it was built in the Amman-Zarqa Basin, a major groundwater aquifer system in Jordan, with a large number of wells. Thirty groundwater wells located in this refugee camp and its surrounding area were sampled and investigated for Total dissolved solids, pH, total hardness, Ca^{2+}, Mg^{2+}, HCO_3^-, K^+, Na^+, Cl^-, NO_3^-, SO_4^{2-}, Fe, Mn, Ni, Cu, Pb, Zn, Cd, Cr and E. coli. Groundwater wells were clustered (based on water quality data), statistically analyzed and compared with previous data (before establishing the camp), for better characterization of changes in water quality. The majority of water quality parameters showed values within the permissible limits based on Jordan standards for drinking water, with few exceptions. While weathering of rocks is the primary process governing water chemistry, uncontrolled and intensive pumping, dissolution of aquifer materials and leaching soluble salts following irregular rainfall events are contributing factors to water quality. Interestingly, groundwater samples collected from wells located in the camp and the nearest area showed a relatively better water quality, compared to other wells. This finding challenges the public opinion that groundwater wells in the vicinity of the camp would probably be of low quality. Also, this indicated that groundwater wells in this camp are probably better managed and controlled compared to others. It was also found that most water quality variables exhibited similar patterns, with lower values observed in the pre-2012 data. Although elevated levels of water quality parameters coincided with establishing the camp, no imminent threats of pollution to these groundwater resources have been observed.

Keywords: Zaatari Refugee Camp, groundwater quality, Jordan, Amman Zarqa Basin

1. Introduction

Jordan has experienced a dramatic population growth over the last seven years due to the influx of Syrian refugees. The growing number of population along with the urban expansion and economic development, have put major pressures on Jordan's existing water resources, especially in the northern region (Irbid, Zarqa, Mafraq). Before the Syrian conflict, the per capita share of water in Jordan ranged between 140 and 145 m^3 compared to the international standard of 1000 m^3 (UNHCR, 2018). According to MWI (2013), the rapid increase in the number of Syrian refugees exerted high pressure on public water supply systems, where in certain areas, the number of served persons almost doubled.

With its very limited surface water resources, Jordan relies heavily on groundwater resources to fulfill the growing demand for water (Al-Rawabdeh et al., 2014). In addition to a rapid decline in groundwater levels, excessive withdrawal of the groundwater reserve along with the unregulated expansions of domestic and industrial areas, have exacerbated water quality problems, where groundwater pollution has increasingly become an imminent threat to the water supplies (Al-Taani, 2013; 2014; 2018b). Evidence of water quality deterioration has been frequently reported (Al-Rawabdeh et al., 2013; Al-Taani et al., 2012).

Following the Syrian conflict, about 1.4 million Syrians have been displaced to Jordan (UNHCR, 2018), of which about 80,000 persons are housed in the Zaatari Refugee Camp (ZRC). The ZRC is the largest Syrian refugee camp in Jordan, located in the northeastern region, close to Jordan's northern border with Syria (Al-Harahsheh et al., 2015). The ZRC was built in the Amman-Zarqa Basin (AZB) which is a major source of groundwater in Jordan (Al-Taani et al., 2018a). A large number of new groundwater wells have been drilled

* Corresponding author e-mail: taaniun@hotmail.com

within ZRC and its surrounding area to meet the growing demands of water for refugees and the host communities. Due to groundwater abstraction, a5-m decrease in water table has been observed in one of the observation wells in ZRC during the period 2000-2012(UNEP/UNDP, 2015). In addition, water samples from wells in close proximity to ZRC showed elevated levels of E. Coli and Total Cell Count with time since 2011(UNEP/UNDP, 2015).

Groundwater aquifers of northeastern Jordan (in AZB), where ZRC was established, are of critical economic and social significance to the region, as they are the primary source of irrigation and drinking water. AZB contains about a quarter of all groundwater wells in Jordan (Margane et al., 2015). Also, this region is part of the recharge areas to groundwater aquifers, where changes in land use and human activities will ultimately affect groundwater quality.

With ever-increasing water demands, the management and protection of these groundwater resources are significant to maintain adequate water supply for the host communities and refugee camp. This study intends to determine and assess the groundwater quality conditions in wells located in ZRC and the surrounding areas. The ZRC has been a constant source of concern to public authorities and local communities because it was built in the Amman-Zarqa Basin, a major groundwater aquifer system in Jordan. This study also compares water quality data before ZRC was established to the results confirmed by the current study. This assessment is likely to unveil the natural and anthropogenic sources governing the aquifer water quality, including the potential impact of ZRC on these water reserves. This aids decision-makers and public authorities manage existing water supplies for sustainable use through the implementation of preventive measures and strategies for wellfield management.

2. Study Area

The ZRC is the largest Syrian refugee camp in Jordan with an area of about 5.5 km^2. It was opened in 2012, following the Syrian conflict and is currently hosting about 80,000 people. It is located in the northeastern region, close to Jordan's northern border with Syria (figure 1). The ZRC was built in AZB which is a major source of groundwater in Jordan (Al-Taani et al., 2018a). In response to the rapid increase in water demands, a large number of groundwater wells were dug within ZRC and its surrounding area. In 2016, three water wells were established within the ZRC border with a total daily capacity of 3800 m^3 (UNHCR, 2018). Also, a wastewater treatment plant with a total capacity of 3600 m^3/d was constructed. In addition, a piped water supply distribution system is currently under construction along with a piped sewerage network, linking the collection system to the wastewater treatment plant to meet the needs of the camp's population (UNHCR, 2018).

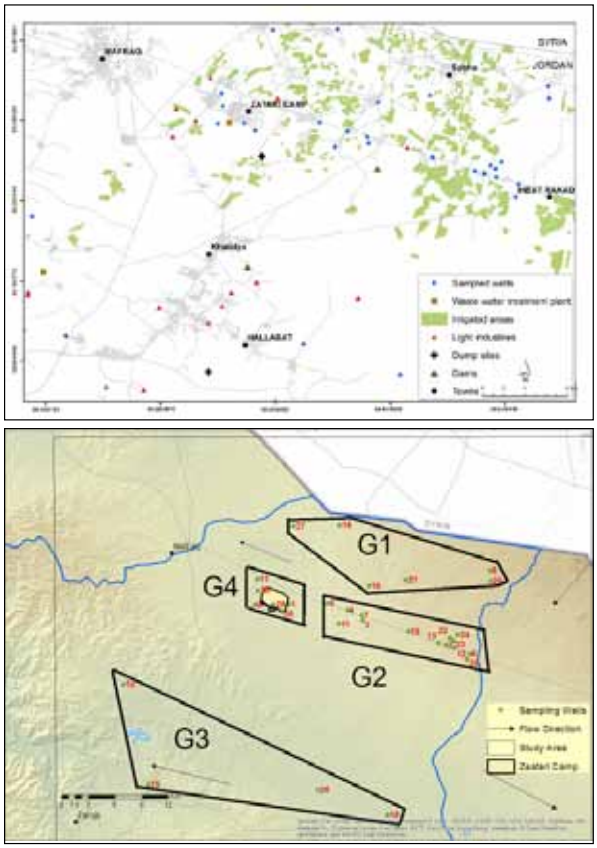

Figure 1. Location map of water sampling wells (upper) and their clusters (lower).

The AZB represents a transitional area between Jordan highlands in the west and the desert in the east. It is subdivided into two main catchments; Wadi Dhuliel sub-basin representing the arid conditions and flat land (where ZRC is located), and the Zarqa River sub-basin which represents the most populated mountainous area. The total catchment area is about 3918 km^2 (RSS, 2005), with 89% located in Jordan and 11% inside the Syrian territory.

The AZB is part of the Mediterranean climate, with an arid climate in the southeastern, eastern, and northeastern regions and rainy humid conditions in the west. Humidity and precipitation decrease rapidly towards the eastern deserts (USAID and WAJ, 1989), with an average annual precipitation of 300 mm (commonly occur as flash floods).

According to Bender (1974), the main geological formations outcropped in the study area can be summarized as follows:

Wadi Es-Sir Limestone Formation (WSL) (Turonian) crops out extensively in the northern, central and southern parts of the study area. The massive crystalline limestone is karstic and weathered in the top 20 m of the formation, below which is a general increase in the marl chalky limestone and thin marl beds occur.

Wadi umm Ghudran Formation (WG) (Coniacian - Santonin) lies uncomfortably above Wadi Es-Sir Limestone Formation. It consists of massive chalk white in addition to chalky limestone and some marls, the depositional environment is the mid to inner shelf (Smadi, 2000).

Amman Silicified Limestone Formation (ASL) and Al-Hisa Phosphorite Limestone Formation (AHP) (Santonian-Campanian). These formations are considered as one unit in the study area which consists of alternating micritic limestone with chert varying in thickness and alternating between phosphatic chert and phosphatic limestone. The depositional environment is marine shelf (Smadi, 2000).

The Basalt Plateau (Oligocene-Pleistocene) is composed of basalt, and crops out in the northeastern part of the basin. They are represented by Abed Olivine Basalt (AOB) and Fahda Vesicular Basalt (FA) Formations. Thin layers of clay and gravel of limestone and chert pebbles occur between the successive Scoriaceous basalt and volcanic plugs basalt flows.

The Younger Alluvium Formation (Alluvium mudflat "Amf", Alluvial "Al", Sand "S", and Pleistocene Gravel "Plg"), of a Quaternary age, consists of thin deposits overlying the basalt in the cemented outwash and the old river terraces. River- and superficial- gravels and silts are widespread. Figure 2a shows a geological map of the study area.

Figure 2b shows a simplified hydro-geological units map in the study area. The major groundwater aquifer in AZB is B2/A7 and Basalt systems aquifers. In many parts of the study area, water levels have declined to alarming levels, where farmers have drilled further deep to the next aquifers (A4, A1/2 and often Kurnub aquifers) to obtain enough water for irrigation (Margane et al., 2015 and MWI, 2013). With high salinity levels encountered in the Kurnub, irrigation water has to be desalinated, where the brine has been discharged into adjacent valleys. This has exacerbated the salinity problem in the B2/A7 aquifer as well (Margane et al., 2015 and MWI, 2013). Between 1995 and 2015, a decline in water levels of about 60 m was estimated, with an annual drop rate of 5 m in recent years (Margane et al., 2015 and MWI, 2013), coinciding with increasing water demands following the Syrian refugee influx. This has changed the groundwater quality and flow regime, where agricultural runoff from intensive agricultural lands, ended up in B2/A7 aquifer (Margane et al., 2015). Irrigation effluents (of Wadi Dhuleil-Hallabat and Badia areas) now flow towards the Yarmouk River, with a subsequent increase in salinity levels in this region (Mafraq) (Margane et al., 2015).

The basalt aquifer extends from the northern border of Jordan southwards to Al-Azraq and Wadi Dhuleil areas. The aquifer occupies a surface area of 1,100 km^2 in northeastern Jordan (Shahin, 2007). In some localities, large quantities of groundwater can be withdrawn, since it is characterized by a large thickness. The aquifer discharge increases the base flow in the basin of the Upper Yarmouk River, Wadi Dhuliel-Wadi Zarqa and Zarqa River. The transmissivity of Basalt aquifer system ranges from almost zero to 11300m^3d^{-1}, and the specific capacity of wells ranging from 0.07 to 3352$m^3h^{-1}m^{-1}$ (Shahin, 2007). The quality of water is classified as good with total of dissolved solids (TDS) ranging from 500 to 1000 ppm (Shahin, 2007). Muwaqqar Chalk Formation B3 (Paleocene) is composed of chalky to marly limestone and cherts that have been deposited in a shallow marine environment. Because of its composition, it acts as an aquitard that separates the upper aquifer systems (Basalt, B4/B5) from the underlying aquifer system (A7/B2) (MWI and BGR, 2019).Figure 2c shows a NW - SE Hydro-geological cross- section to understand the hydro-geological set-up in the study area.

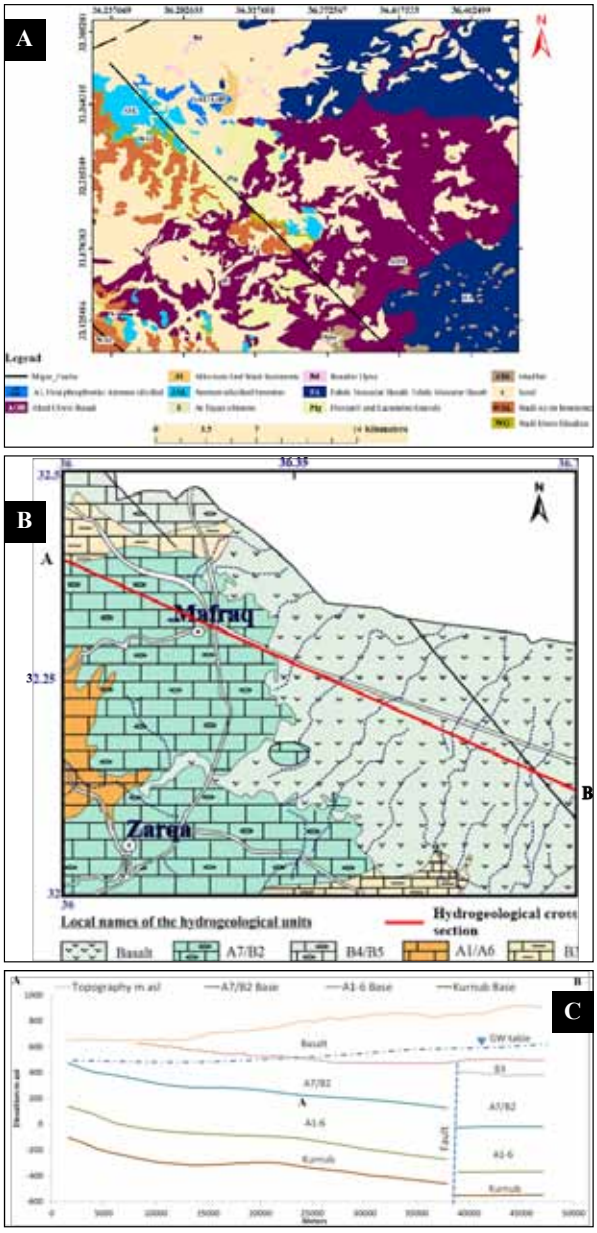

Figure 2. a- Geological map of the study area (After Smadi, 2000; Gharaibeh, 2003) b- Simplified Hydro-geological map of the study area (MWI and BGR, 2019) c. NW-SE Hydro-geological cross-section (For location See Figure 2b).

The soils in the study area are affected by rainfall and relieves. It is immature with silty loam to loamy texture (Al Mahamid, 2005). It is composed of a silty clay loam and clay loam (with a high calcareous content and weakly to moderately saline) with stony silty clay loam (with a content of calcareous material and weakly saline) (Al Mahamid, 2005).

3. Materials and Methods

One-hundred and twenty groundwater samples were collected from August to December of 2017 from thirty different wells located within the ZRC border and its surrounding region. The distribution of groundwater sampling wells is presented in figure1. These groundwater wells are owned by the government, and are largely dug in B2/A7 aquifer, except for wells 2, 3, 5, 8, and 26. After purging, the water samples were collected in one-liter pre-cleaned polyethylene containers (pre-acidified containers were used for trace-metal analysis). Following collection, the samples were kept in an icebox at 4°C and were transported to the water laboratory for subsequent chemical analyses. In addition to the dissolved trace metals, a variety of water quality parameters were analyzed for this assessment (Table 1). Total dissolved solids (TDS) and pH were measured in-situ using portable field meters. Total hardness (TH) and Ca^{2+} were measured with the EDTA titrimetric method and Mg^{2+} by calculations. $HCO_3^-$was determined by potentiometric titration. K^+ and Na^+ were determined by Flame photometer (Jenway Clinical PFP7). Cl^-, NO_3^-, and SO_4^{2-}were analyzed by Ion Chromatography (Dionex DX-120). Trace metals (Fe, Mn, Ni, Cu, Pb, Zn, Cd, and Cr) were measured with inductively coupled plasma ICP-OES (PerkinElmer). E. coli was measured by Colilert*-18 (IDEXX). Measurements and preparation were performed according to the standard methods (APHA 1998), and an ICP multi-element standard solution (from Merck Millipore) was used. All measurements were conducted at the Water, Environment and Arid Regions Research Center, Al al-Bayt University in Jordan.

The water quality data were checked for accuracy by computing the ion balance of major cations (Ca^{2+}, Mg^{2+}, Na^+, K^+) and anions (HCO_3^-, Cl^-, SO_4^{2-}, NO_3^-) in meq/l. The ionic mass balance was calculated by dividing the difference of the total cations and anions by the sum of cations and anions multiplied by 100. The average ion balance for water samples was -3.16%.

4. Results and Discussion

Results of water quality characteristics (physical, chemical, and biological) of the groundwater wells located within ZRC and its surrounding area are summarized in Table 1. The pH values ranged between 6.6 and 8.4 with an average value of 7.2. These values are generally consistent with open-system carbonate dissolution (Langmuir, 1971). The highest pH level was observed in well 1 which is located in ZRC, whereas the lowest was recorded in well 30 (located adjacent to ZRC). It is noteworthy that well 1, 28, and 29 are located within the border of ZRC (figure 1). These levels of pH values are within the range listed for waters suitable for drinking water (JS, 2008).

Table 1. Summary statistics of water quality parameters for the groundwater wells located in ZRC and its surrounding area (from 8-12/2017) (Alt. Altitude, W.D.: Well Depth, A.N.: Aquifer Name, Y: Yield, W.L.: Water Level, D.D.: Drawdown).

Well No.		pH	Na^+	K^+	Ca^{2+}	Mg^{2+}	Cl^-	NO_3^-	SO_4^{2-}	HCO_3^-	TDS	TH	E.Coli	Alt. (m)	W.D. (m)	A.N. (Aquifer Name)	Y. (m^3/h)	W.L. (m)	D.D. (m)
			mg/L																
1	Mean	8	131.8	4.8	38.5	41.7	154.3	11.1	60	209.9	530.3	247	<1	-	-	-	-	-	-
	Max	8	172.9	7.1	48.1	51	168.7	14.7	60.4	210	579	270							
	Min	8	94.5	3.1	29.5	31.6	135.4	7.9	59.2	209.9	488	230							
	STD	0	39.3	1.9	7.8	8	17.1	3.4	0.7	0.1	38.2	21							
2	Mean	7	121.4	9.6	50.3	46.7	278.7	25.9	86.4	109.3	758.5	318	<1	790	373	B2/A7	85	268	1
	Max	7	131	15.9	64.1	48.6	287.9	27.6	96.9	131.2	780	330							
	Min	7	108.3	5.7	36.1	41.3	265.4	24.2	78.8	78.7	745	290							
	STD	0	11.7	4.8	11.5	3.6	11.8	1.7	9.4	27.3	16.5	19							
3	Mean	7	88.7	3.1	27.7	13.2	74.7	6.6	44	183.7	378.5	123	<1	732	400	BA	87	212	4
	Max	8	102.6	4.2	34.7	17	84.4	8.2	51.7	209.9	391	140							
	Min	7	69.7	1.8	20	5.7	69.5	4.9	39.6	170.6	365	110							
	STD	0	17	1.2	6	6.5	8.4	1.7	6.7	22.7	10.8	15							
4	Mean	7	94.7	5.4	35.2	17.7	132.5	19.4	30.4	135.6	453	153	<1	706	305	BA	63	183	3
	Max	7	112.9	9.3	44.1	19.4	143.9	21.2	36.2	144.3	462	170							
	Min	7	71.2	2.3	24	14.6	124.1	16.5	27.2	131.2	443	140							
	STD	0	21.4	3.3	8.3	2.7	10.3	2.6	5.1	7.6	8	15							
5	Mean	7	81.8	2.7	24.2	12.1	60.7	15.9	32.1	170.6	328.3	100	<1	693	293	B2/A7	83	169	2
	Max	8	95.1	4.3	28.6	17	69.5	18.2	33.8	183.7	337	110							
	Min	7	64.7	1	16	7	50.5	12	31.3	157.4	321	90							
	STD	0	15.6	1.6	5.8	4.1	9.6	3.4	1.4	13.2	6.9	10							
6	Mean	7	111.8	6.1	59	54.5	295.3	28.8	98.4	98.4	842.3	365	<1	798	395	BA	44	277	5
	Max	7	129.9	6.4	64.1	55.4	307.7	29.1	100.4	118.1	870	370							
	Min	7	82.8	5.8	56.1	53.5	282.9	28.5	96.4	85.3	827	360							
	STD	0	25.4	0.4	4.4	1.3	17.5	0.4	2.8	17.4	24	7.1							
7	Mean	7	89	4.8	28.2	19.4	86.5	7	38.4	168.4	388.3	150	<1	726	450	B2/A7	67	208	23
	Max	7	107.4	8.1	32.6	29.2	89.3	7.7	39.5	183.7	394	200							
	Min	7	69.7	3	24	14.3	81.9	5.8	37.3	157.4	386	130							
	STD	0	18.9	2.8	4.8	6.7	4	1.1	1.1	13.7	3.9	34							
8	Mean	7	140.2	7.8	30.2	25.4	162.3	26.6	80.2	160.7	560.8	180	<1	920	580	B2/A7	55	402	6
	Max	8	162	10.4	40.1	34	188.6	31.1	91.4	183.6	656	240							
	Min	7	112.3	5.8	20	19.4	119.5	22.1	69.6	131.2	475	130							
	STD	0	22.8	2.2	9.7	6.1	37.4	4.5	10.9	22.4	79.4	47							
9	Mean	7	86.6	3.3	56.8	43.5	136.5	24.7	49.8	240.5	574.3	303	<1	642	382	A4	47	169	41
	Max	7	106.3	5.2	68.1	48.6	138.9	30.5	51.3	262.4	587	340							
	Min	7	59.7	2.4	50.9	37.7	134	16.4	48.2	196.8	558	280							
	STD	0	24.1	1.3	7.9	6	3.5	7.4	2.2	37.9	13	32							
10	Mean	7	110	3.4	41.1	33.9	171.8	31.8	44	113.7	374.3	128	<1	606	292	B2/A7	119	86	1
	Max	7	178.6	4.7	83.3	78.3	259.1	32.7	68.6	131.2	412	140							
	Min	7	71.2	1.8	20	15.8	84.4	30.8	19.4	91.8	337	115							
	STD	0	59.6	1.5	36.5	29.7	123.5	1.3	34.8	20.1	37.5	13							
11	Mean	7	88.9	3.7	22.2	13.9	73	14.5	30.4	159.1	331	113	<1	695	444	B2/A7	60	194	7
	Max	7	98.9	5.4	28.6	19.4	89.3	16.7	31.8	183.7	337	150							
	Min	7	83.6	2.2	16	4.5	60.2	13	29.6	131.2	326	90							
	STD	0	8.7	1.5	7.1	6.6	14.9	1.9	1.2	21.7	5.8	26							

12	Mean	7	109.4	7.4	53.8	42.1	246.1	23.7	79.9	105	710.8	290	<1	795	423	B2/A7	85	287	2
	Max	7	117.7	10.3	68.1	46.2	277.9	23.9	82	118.1	724	300							
	Min	7	100.2	5.9	46.8	36.5	227	23.4	78.4	91.8	697	280							
	STD	0	8.8	2.5	9.8	4.3	27.7	0.4	1.9	13.2	12.8	10							
13	Mean	8	114.4	7.6	47.3	40.3	245.7	23.3	79.5	135.6	763.3	277	<1	790	415	B2/A7	83	280	3
	Max	8	138.4	11.1	56.1	41.3	258.1	25.2	90.5	144.3	881	290							
	Min	7	77.8	5.7	40.1	38.4	233.3	21.3	71.7	118.1	693	270							
	STD	1	32.2	3.1	6.7	1.7	17.5	2.8	9.8	15.1	83.5	12							
14	Mean	7	148.1	6.1	35.8	36.8	232.4	25.2	62.7	144.3	747.3	233	<1	740	497	B2/A7	52	260	21
	Max	7	175.1	8.5	44.1	37.3	248.2	27.2	64.9	157.4	770	240							
	Min	7	96.9	4.8	28.1	36.5	223.3	23.1	60.1	131.2	720	220							
	STD	0	44.4	2.1	6.6	0.5	13.7	2.1	2.4	13.1	21.1	12							
15	Mean	7	211.5	7.5	43.2	56.1	395.4	34.3	73.1	154.2	1078.5	308	<1	580	315	B2/A7	77	77	21
	Max	7	240.5	11.6	64.1	65.6	441.7	36.6	76	170.6	1120	330							
	Min	7	162.6	4.7	20	30.4	362.3	32.7	70.2	131.2	1030	285							
	STD	0	42.6	3.3	24.2	17.2	41.3	2	4.1	19.7	37.1	23							
16	Mean	7	178.7	11.5	81.9	71.5	499.2	40	156.2	114.8	1274.8	490	<1	759	400	B2/A7	60	255	1
	Max	8	209.5	19.7	92.2	73.5	518.7	52.2	164.2	131.2	1295	500							
	Min	7	125	7.3	71.1	70.5	451.6	33.8	144.6	91.8	1246	480							
	STD	0	46.6	7.1	8.8	1.7	31.9	10.5	10.3	19.7	20.7	10							
17	Mean	7	90.1	2	56.8	38.4	141.4	20.7	50.8	255.8	622.3	300	<1	650	415	B2/A7	0	0	0
	Max	7	106.3	2.3	68.1	43.7	143.9	22.6	51.1	301.7	691	340							
	Min	7	70.2	1.7	50.9	34	138.9	17	50.4	209.9	582	270							
	STD	0	18.3	0.3	7.9	4.8	3.5	3.2	0.5	46.1	49.7	32							
18	Mean	7	74.7	3.6	17.1	12.7	39.7	12.8	22	131.2	272.5	95	<1	590	124	B2/A7	91	79	0
	Max	7	88.6	4.8	24.5	19.4	64.5	13.4	22.2	131.2	280	130							
	Min	7	62.2	3	12	7	14.9	11.8	21.7	131.2	263	80							
	STD	0	13.3	1	6.2	5.1	35.1	0.9	0.4	0	7.1	24							
19	Mean	7	165.4	10.5	52.3	50.3	352.8	24.6	110.1	121.5	936.3	338	<1	741	352	B2/A7	70	252	2
	Max	7	195.1	17.4	56.1	58.3	367.3	26.9	123.7	131.2	945	380							
	Min	7	112.9	7	48.1	43.3	327.6	22.2	101	118.1	919	300							
	STD	0	45.6	5.9	4.4	7.9	21.9	3.3	9.7	6.5	11.7	44							
20	Mean	7	226.5	11.3	91	88.8	541	29.3	144.8	96.2	1477	593	<1	911	624	B2/A7	23	417	8
	Max	7	261.1	16.1	93.4	106.9	610.4	30.3	163.7	105	1722	670							
	Min	7	194.3	8.8	88.2	72.9	486.4	28.4	128.6	91.8	1337	520							
	STD	0	33.5	4.1	2.3	17.8	63.3	1	18.1	7.6	172.5	79							
21	Mean	7	187.2	11.2	80.9	83.8	418.6	21.1	146.6	164	1222.8	507	<1	832	428	B2/A7	35	307	7
	Max	7	188.9	18.8	88.2	99.6	456.6	22.3	157.4	209.9	1309	550							
	Min	7	185.3	7.2	69.1	71.7	377.2	19.2	128.6	131.2	1132	460							
	STD	0	1.8	6.6	8.6	14.3	39.8	1.7	15.7	39.4	75.1	45							
22	Mean	7	94.1	5.6	24.2	14.9	81.9	13.1	23.5	192.4	349	122	<1	800	424	B2/A7	55	308	4
	Max	7	112.9	10.2	28.6	26.7	89.3	13.3	23.6	209.9	355	180							
	Min	7	69.2	3.2	16	5.7	74.4	12.9	23.4	170.6	346	90							
	STD	0	22.5	4	7.1	10.8	10.5	0.3	0.1	20	5.2	51							
23	Mean	7	92.9	5.6	24.2	15.7	81.9	10.9	22.7	192.4	345	125	<1	805	492	B2/A7	55	308	1
	Max	7	109.1	10.2	24.5	29.2	89.3	12.7	22.7	196.8	349	180							
	Min	7	73.7	3	24	7.3	74.4	9.1	22.6	183.7	342	90							
	STD	0	17.9	4	0.3	11.8	10.5	2.5	0.1	7.6	3.6	48							
24	Mean	7	84.4	5.3	19.5	16.9	59.6	9.2	21	179.3	311	118	<1-3.1	825	470	B2/A7	55	328	4
	Max	7	99.7	9.8	26.5	29.2	59.6	11.4	21	183.7	313	160							
	Min	7	67.7	2.8	16	8.2	59.6	6.9	20.9	170.6	309	95							
	STD	0	16	3.9	6.1	10.9	0	3.2	0.1	7.6	2	36							
25	Mean	8	96.4	6	48.9	61.4	245.7	25.7	77.3	105	744.3	318	<1	794	500	B2/A7	50	296	0
	Max	8	108.4	6.6	72.1	75.3	248.2	26.5	83.8	118.1	751	325							
	Min	7	77.3	5.3	30.6	52.2	243.2	24.9	70.7	91.8	732	310							
	STD	0	16.7	0.9	21.2	12.2	3.5	1.1	9.3	18.6	10.7	11							
26	Mean	7	138.6	7.3	39.8	26.2	212.2	13.2	69.1	147.6	697.5	223	<1	585	243	B2/A7	30	104	0
	Max	7	164.1	10.4	48.1	31.6	213.4	14.3	69.8	157.4	714	250							
	Min	7	92.8	4.1	20	22.7	210.9	12.5	68.3	131.2	688	210							
	STD	0	39.8	3.5	13.3	4.7	1.8	1	1.1	12.5	11.6	23							
27	Mean	7	177.9	8.6	61.1	51.1	459.9	34	114.3	154.2	1178	383	<1	695	454	B2/A7	37	277	0
	Max	7	234.3	12.9	72.1	60.8	516.2	36.8	131	183.7	1442	470							
	Min	7	108.4	5.5	40.1	36.5	357.3	30	93.3	118.1	828	250							
	STD	0	64	3.5	18.2	12.9	89	3.6	15.9	29.1	312.8	117							
28	Mean	8	86.4	4.2	30.2	44	114.2	5.6	51.9	259	418.8	263	<1	644	430	B2/A7	36	219	55
	Max	8	102.8	6.3	48.1	62	124.1	6.2	52	275.5	455	280							
	Min	7	67	3	10	26.7	104.2	4.9	51.8	236.1	383	230							
	STD	1	18.1	1.6	19.2	14.9	14.1	0.9	0.1	16.5	29.4	29							
29	Mean	8	88.3	3.7	42.5	32.9	98.7	8.4	48.8	236.2	449	230	<1	652	430	B2/A7	55	203	39
	Max	8	107.7	5.6	56.1	44	114.1	11.1	52.1	275.5	575	270							
	Min	7	64.8	2.9	35.6	24.3	77.8	5.7	42.8	209.9	335	200							
	STD	1	21.7	1.3	9.3	10.1	18.8	3.8	5.2	32.1	99	36							
30	Mean	7	86.7	3.3	51.8	41.6	161.3	17.2	57.3	221.4	598.8	297	<1	670	434	-	50	193	0
	Max	7	110.1	3.9	56.1	48.6	178.7	23	65.4	249.3	624	330							
	Min	7	58.2	2.7	46.8	36.5	143.9	8.6	49.2	157.4	575	280							
	STD	0	26.3	0.6	3.8	6.3	24.6	7.6	11.5	43	21.3	29							
Average	Mean	7	119.9	6.1	43.8	38.2	208.5	20.1	66.9	164.3	657.2	256	<1	729.9	406.3	-	58.9	228.2	9.0
	Max	8	261.1	19.7	93.4	106.9	610.4	52.2	164.2	301.7	1722	670							
	Min	7	58.2	1	10	4.5	14.9	4.9	19.4	78.7	263	80							
	STD	0	48.1	3.8	21.1	22.4	150.5	9.6	40.2	51.1	330	133							

Elevated levels of TDS in the groundwater samples were observed. The average TDS concentrations varied from 263 mg/L (well 18) to 1722 mg/L (well 20) with an overall mean concentration of about 657 mg/L (Table 1). Eleven wells showed average TDS concentrations below 500 mg/L (freshwater), whereas the remaining groundwater wells are classified as brackish (>500-30,000 mg/L). Although drinking water containing more than 500 mg/L is undesirable, such water, commonly used in this region as less mineralized water, is rare or not available.

The TDS values are likely elevated due to uncontrolled and intensive pumping. In addition, the dissolution of aquifer materials, leaching soluble salts following irregular rainfall events (enhanced probably by evaporative concentration) are contributing factors to high TDS levels. It is noteworthy to mention that carbonate and evaporite rocks are widespread in the study area. While seasonal variations have not been investigated, higher TDS levels are expected during summer seasons, when the demand for water increases and over-abstraction of groundwater becomes widespread.

The concentrations of water quality parameters in different wells are plotted in figure3. Higher levels were consistently observed in wells 16, 20, and 27. The average concentration of TDS in wells 16, 20, and 27 exceed the permissible limits of 1000 mg/L based on Jordan standards for drinking water (JS 2008). These wells are extensively abstracted for public use, livestock farming and irrigation as they are located in close proximity to human settlements. Total Hardness (TH) of the groundwater samples varied from 80 to 670 mg/L, with the highest value observed in well 20 and the lowest in well 18 (Table 1 and Figure3).

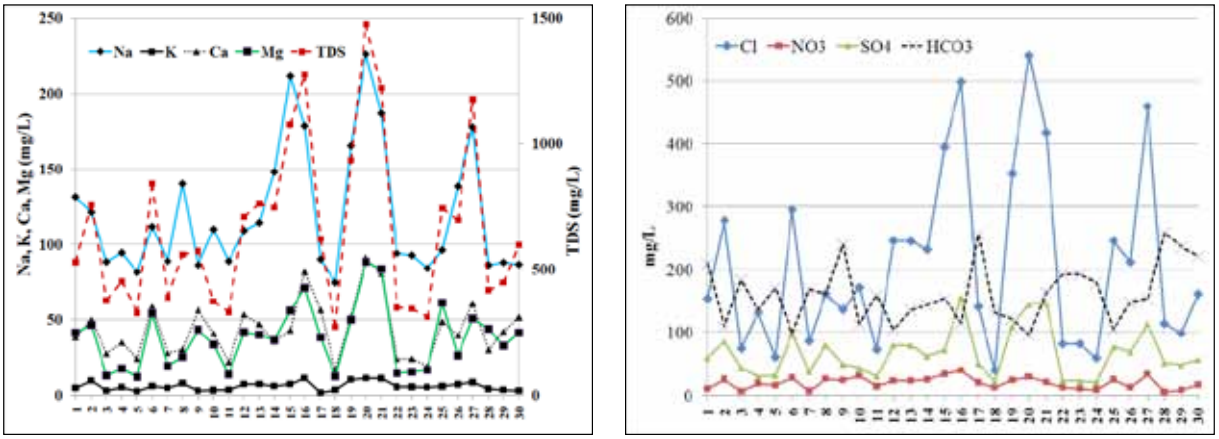

Figure 3. Concentrations of Na^+, K^+, Ca^{2+}, Mg^{2+} (left), Cl^-, NO_3^-, SO_4^{2-}, and HCO_3^- (right) in the water wells of ZRC and its surrounding areas.

Similarly, the average concentrations of Na^+, K^+, Ca^{2+} and Mg^{2+} varied widely from 58.2-261.1, 1-19.7, 10-93.4 and 4.5-106.9 mg/L, respectively (Table 1).Groundwater wells 15 and 20 showed Na^+ levels that are in excess of standard limits for drinking water (200 mg/L). Well 27 exhibited a relatively high average value for Na^+, but it agrees with the standard limit for drinking water.

Cl^- concentrations in groundwater samples ranged between 14.9 and 610.6 mg/L (Table 1), exceeding the permissible limit of 500 mg/L for drinking water set by Jordan, in well 20 (541 mg/L). Increased concentrations of Cl^- were measured in well 16, but they are still within the acceptable limit for drinking purposes. SO_4^{2-} in the water wells ranged in concentration from 19.4 to 164.2 mg/L. None of the thirty wells exceeded the Jordan drinking water limit of 500 mg/L (Table 1). The concentrations of SO_4^{2-} are likely derived from the dissolution of evaporite deposits (gypsum and anhydrite).

Nitrates (NO_3^-) are widespread throughout the aquifer and present in all of the samples, where the concentrations increased in some areas, although not all. NO_3^- concentrations ranged between 4.9 mg/L (well 28) and 52.2 mg/L (well 16), with a mean concentration of 20.1 mg/L. Few groundwater samples from well 16 exceeded the NO_3^- permissible limit for drinking water of 50 mg/L, though the average level in well 16 was 40 mg/L. The relatively high NO_3^- levels found in several samples are probably related to the leaching of agricultural nitrogen (especially the use of inorganic fertilizers and manure) with irrigation drainage or during flash floods. Farm livestock also produce nitrogen-containing waste that possibly contributes to groundwater.

No evidence of wastewater pollution has been observed, where the E. coli has been not detected / or remained constantly below 1 MPN/100 ml, except for well 24 (Table 1). Having said this, cesspools are widespread and a septic system failure is likely to occur. However, the high depths of groundwater levels (Table 6) for the majority of wells make it difficult to detect the faecal bacteria indicator (E. coli) in the water samples.

HCO_3^- concentrations ranged between 78.7 and 307.1 mg/L (Table 1). The majority of water quality parameters showed similar ups and downs in the same well simultaneously, except for HCO_3^-. Bicarbonate levels exhibited different trends, where the concentrations fluctuated independent of other ions patterns. For example, it decreased in wells 16, 20, and 27, though other parameters have exhibited exceptionally higher values. These observations may suggest that HCO_3^- was originated from different sources (which is less likely) or has been precipitated.

For a better assessment and characterization of the spatial distribution of water quality data, groundwater wells were clustered into four groups (Figure 1), and the results are presented in Table 2. The average values of pH in the groundwater wells were noticeably equal in all groups. The relatively highest values of all water quality variables were consistently observed in group 1 (G1), except for HCO_3^-. Interestingly, the groundwater samples collected from the wells located in ZRC and its nearest areas showeda relatively better water quality, with the majority of water quality parameters exhibiting lower levels in these wells (with few exceptions i.e. $HCO_3^-$and TH, though they remain within the acceptable limits for drinking purposes). This finding opposes the initial thoughts in this study and challenges the public opinion that groundwater wells in the vicinity of ZRC would probably be of a low quality.

Table 2. Average concentrations of a variety of water quality parameters clustered in four groups compared to Jordan guidelines for drinking water (data collected from August-December 2017).

Group No.	pH	Na^+	K^+	Ca^{2+}	Mg^{2+}	Cl^-	NO_3^-	SO_4^{2-}	HCO_3^-	TDS	TH
		mg/L									
G1	7.2	174.2	9.3	58.6	56.0	361.2	26.8	109.8	140.2	1020.4	372.2
G2	7.3	103.3	6.0	39.0	31.5	175.8	18.9	58.6	146.4	569.9	218.6
G3	7.1	133.7	5.5	35.3	32.2	204.8	23.0	52.1	136.7	605.7	188.7
G4	7.4	95.0	3.6	46.1	40.4	134.4	14.6	53.1	237.1	532.3	273.3
JS 286/2008***	6.5-8.5	200	-	-	-	500	50	500	-	1000	500

***: *Jordanian standards for drinking water.* -: *not required*

Data in Table 2 also show apparent spatial variations. The spatial distribution of TDS in groundwater illustrates that high occurrences of TDS are located further north-northeast (G1) with an average concentration of 1020.4 mg/L, slightly above the Jordan standards for drinking water of 1000 mg/L. However, the lowest values were measured in G4. Again, these results collectively indicate that the groundwater wells in the ZRC are probably better managed and controlled compared to others.

In addition to the dissolved salts from evaporite formation and carbonate layers, the excessive withdrawal of the groundwater coupled with the high evaporation and low rate of recharge (due to prevailing arid climate) are potentially the main contributors to the increased groundwater salinity, particularly in G1 wells. Agricultural discharges following excessive irrigation are probably not a major contributing cause to salinity due to the large depth of the groundwater levels (Table 3). Additionally, water flow directions (Figure1) are not a significant factor influencing groundwater salinity. Wells located down-gradient contain lower TDS values compared to the upper-gradient ones.

Table 3. Pearson Correlation matrix for groundwater wells characteristics.

	Well depth (m)	Yield (m^3/h)	Water level (m)	Drawdown (m)
Altitude (m)	0.73	-0.15	0.91	-0.28
Well depth (m)		-0.45	0.74	0.13
Yield (m^3/h)			-0.14	-0.17
Water level (m)				-0.08

This assessment of TDS distribution pattern in groundwater aids public water supplies and regulatory agencies in targeting zones of lower groundwater TDS concentration by relocating wells or by mixing multiple groundwater sources. In addition, TDS trends also help in quantifying the optimum groundwater abstraction rate without a major increase in salinity for a sustainable utilization of this water source, especially in areas where human settlements are in a close proximity to the groundwater wells and where over-extraction of water is common.

Similar to TDS, the average concentrations of Na^+, K^+, Cl^-, NO_3^-, and SO_4^{2-} showedsimilar spatial distribution patterns with the highest values observed in G1 and the lowest occurring in G4. Ca^{2+}, Mg^{2+}, and TH exhibited elevated levels in G1, but lower concentrations were measured in G3. In the north-northeastern wells (G1) of the study area, the average TH concentration was 372.2 mg/L; it became 188.7 mg/L in the southern groundwater wells. In general, the high values of TH are primarily attributed to the introduction of Ca^{2+} and, to a lesser extent, Mg^{2+} into the groundwater system. Ca^{2+} is derived from the dissolution of Ca^{2+} bearing minerals from the aquifer material (carbonates and evaporites) (Batayneh et al., 2014). Mg^{2+} is likely derived from the dissolution of dolomitic limestone (Batayneh and Al-Taani, 2015). In contrast, the HCO_3^- average level was highest in G4 (237.1 mg/L) compared to other clusters, which showed relatively fairly comparable values. In general, all groups showed groundwater quality values that are within the acceptable limits based on the Jordanian standards for drinking water (JS, 2008), except for TDS levels in G1.

The hydrochemical data (Table 1) and correlation analysis (Table 4) suggest that most of ions in groundwater are probably originated from similar sources. Positively moderate to strong correlations have been observed among water quality parameters (Table 1), except for HCO_3^- and pH. The resultant matrix showed weak correlations of pH with all variables. Likewise, HCO_3^- showed negatively weak to moderate correlations with most of the water quality variables.

Table 3. Correlation matrix for groundwater quality parameters.

Na^+	K^+	Ca^{2+}	Mg^{2+}	Cl^-	NO_3^-	SO_4^{2-}	HCO_3^-	TDS	TH	
-0.02	0.10	-0.10	0.08	-0.02	-0.21	0.07	0.05	-0.03	0.04	pH
	0.82	0.67	0.74	0.90	0.65	0.81	-0.42	0.90	0.74	Na^+
		0.65	0.69	0.85	0.57	0.85	-0.59	0.83	0.72	K^+
			0.92	0.86	0.66	0.89	-0.28	0.89	0.96	Ca^{2+}
				0.88	0.63	0.89	-0.30	0.90	0.97	Mg^{2+}
					0.78	0.94	-0.51	0.98	0.90	Cl^-
						0.68	-0.57	0.73	0.61	NO_3^-
							-0.45	0.94	0.92	SO_4^{2-}
								-0.43	-0.26	HCO_3^-
									0.93	TDS

TDS plotted against $Na^+/(Na^+ + Ca^{2+})$ (Gibbs, 1970) to assess the source of dissolved ions in groundwater (Figure4). This revealed that the weathering of rocks is a primary process liberating ions in water. Evaporation is a minor contributor.

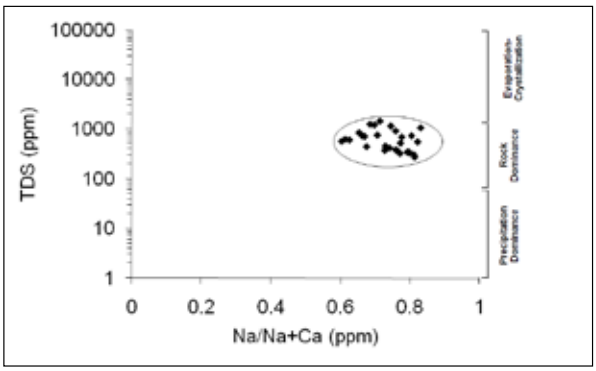

Figure 4. Plot of TDS vs. $Na^+/Na^+ + Ca^{2+}$ of groundwater samples.

Ca^{2+} is positively correlated with Mg^{2+}, and TDS with r = 0.90 and 0.89 respectively. It is believed to have been derived from limestone and dolomite, where these rocks cover a significant portion of the study area. Na^+ and Cl^- concentrations showed consistently similar ups and downs in groundwater wells (figure3). The average correlation coefficient for both ions is 0.90 (Table 4) suggesting common sources for both ions (Batayneh et al., 2014). Mineral dissolution is possibly their major source, where evaporites, particularly halite, are common in the area.

Groundwater is dominant by Na^+, Ca^{2+}, Mg^{2+}, Cl^-, HCO_3^-, and SO_4^{2-}.It is evident from piper plot (Piper, 1944) that all the samples belong to the Ca-Mg-HCO_3type (figure5). The graphs also demonstrate the dominance of alkaline earths over alkali (Ca+Mg>Na+K), and weak acidic anions exceed strong acidic anions (HCO_3>Cl+SO_4).The hydrochemical processes suggested by Chadha (1999) indicate recharging water (Ca-Mg-HCO_3 type). Recharging waters are formed when water enters into the ground from the surface carrying dissolved carbonate in the form of HCO_3^- and the geochemically mobile Ca^{2+}.

Table 1 provides information regarding the sampling groundwater wells. Wells 8 and 20 are located in higher altitudes with an elevation of 920m and 911m above sea level (a.s.l.), respectively. Whereas groundwater wells 18 and 26 lie in low-lying areas with elevations of 590m and 585m a.s.l., respectively.

It has been observed that the altitudinal variations (governing the surface drainage pattern) have no clear impact on groundwater quality. For example, wells 18 and 26 located in low-laying areas were found with a relatively good water quality, though it is expected that the intense rainfall, salts, and dissolved minerals from the surrounding soils and geologic formations are transported down-gradient (following the general flow direction) to end up in these groundwater wells.

Moreover, wells 18 and 26 have shallower depths compared to others, with about 124m and 243m deep, respectively. This also suggests that these two groundwater wells are more vulnerable to water quality deterioration. Groundwater wells 10 and 18 with relatively shallow depths have generally high water yields, among others. Groundwater table drawdown is largest in wells 9 and 28. All groundwater wells are drilled in B2/A7 aquifer except for wells 3, 4, 6, 9, and 27.

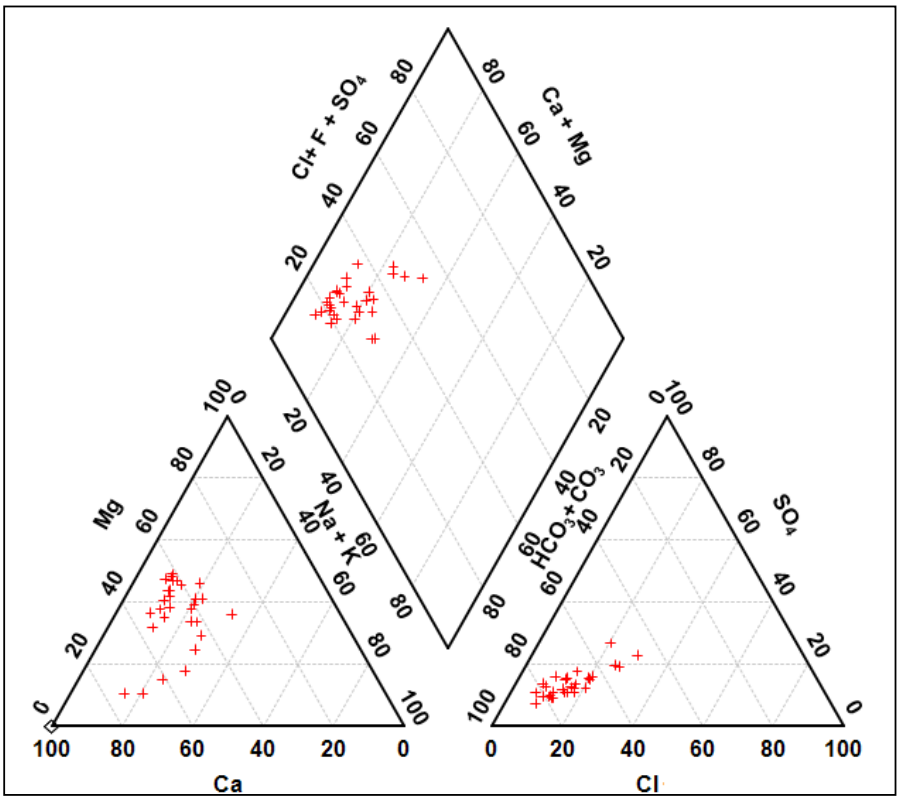

Figure 5. Hydrochemical facies shown on Piper's trilinear diagram along with dominant anions and cations and the classification of the water sample.

Correlation analysis tabulated in Table 3 shows that the characteristics of groundwater wells are not generally related, except for the following pairs: well depth and altitude (r =0.73), water level and altitude (r = 0.91), and water level and well depth (r = 0.74).

Drawdown factor was neither related to yields nor to water levels. Previous data for groundwater quality before ZRC were established (prior to 2012) and compared to the results obtained from this study. Figure 6 demonstrates the variations between the current results and those of studies before 2012.

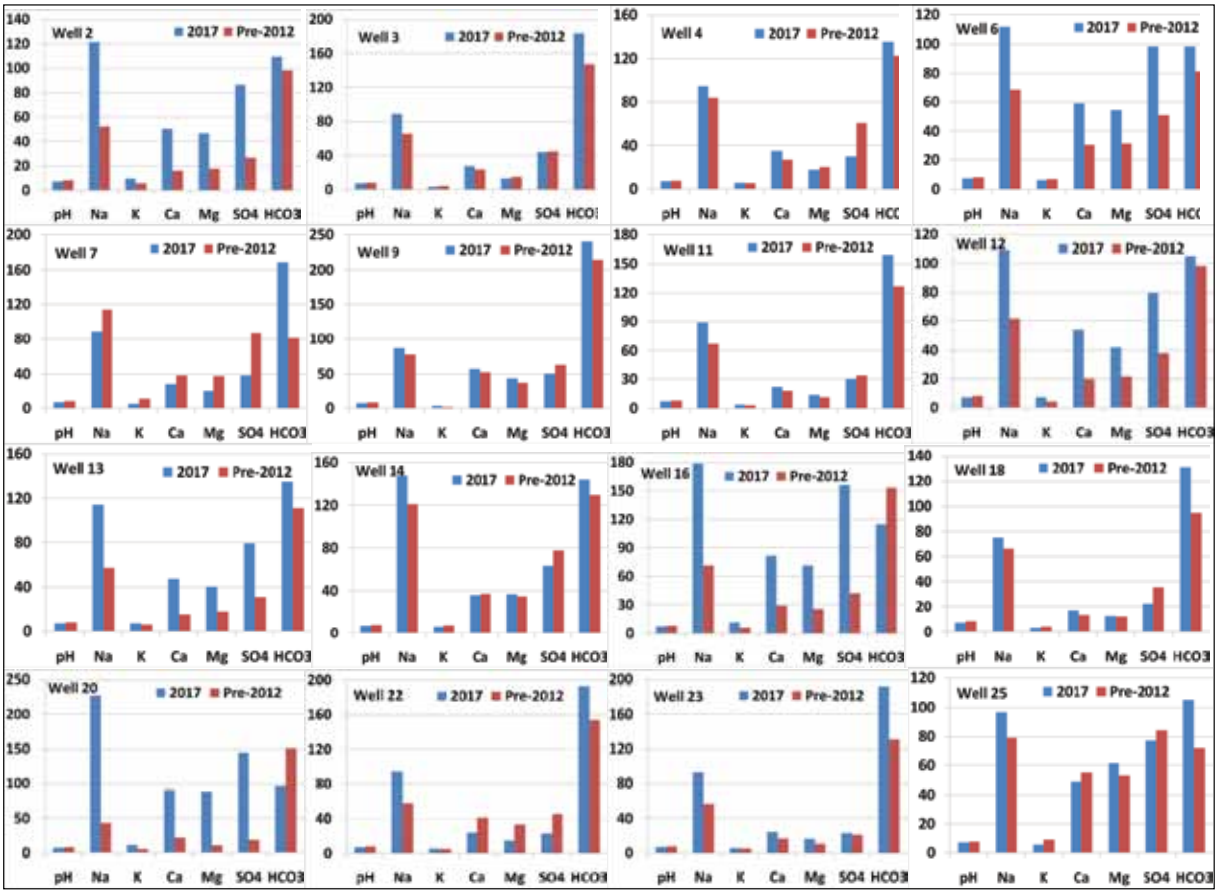

Figure 6. Comparison of water quality data (mg/L) for selected groundwater wells before ZRC was established vs. current results.

It has been noticed that the majority of water quality variables showed similar patterns, with the lower values found in the pre-2012 data and elevated levels recorded in 2017. These findings highlight the importance of drafting a proper management plan of groundwater wells, particularly, regulating groundwater pumping and designating zones for the protection of wells. The inflow of Syrian refugees has certainly increased the demands for drinking water which exacerbated the water quantity problems and would inevitably cause groundwater quality to deteriorate.

Water samples from groundwater sampling wells were analyzed for selected trace metals. The statistics of trace metals are given in Table 5. Metal contents in the groundwater samples were consistently low in all of the sampling wells. These concentrations are largely within the range listed for waters suitable for drinking water (JS, 2008). Pb contents in the water samples showed slightly higher levels than the Jordan standard guidelines for drinking water of 0.01 mg/L (Table 5). Additionally, well 15 showed a mean Mn content (0.304 mg/L) above the acceptable level of 0.0l mg/L. Cd content in well 12 (0.017 mg/L) exceeds the safe limit of 0.003 mg/L. Also, Cr levels in wells 18 (0.073 mg/L) and 21 (0.058 mg/L) are above the permissible limits for drinking water of 0.05 mg/L (JS 2008).

Table 5. Trace-metal content (mg/L) in water samples collected from wells in ZRC and the surrounding area over the period from August to December 2017.

Well No.	Fe	Mn	Ni	Cu	Pb	Zn	Cd	Cr
1	0.046	0.003	<DL	<DL - 0.028	<DL - 0.005	<DL	0.002	0.058
2	0.023	0.002	<DL	<DL - 0.019	<DL - 0.018	<DL	0.001	0.021
3	0.006	0.002	<DL	<DL	<DL - 0.019	<DL - 0.019	0.002	0.002
4	0.013	0.001	<DL	<DL - 0.027	<DL - 0.013	<DL	0.002	0.023
5	0.008	0.001	<DL	<DL - 0.012	<DL - 0.013	<DL	0.002	0.008
6	0.093	0.006	<DL	<DL	<DL	<DL - 0.019	0.001	<DL - 0.021
7	0.027	0.002	<DL	<DL - 0.012	<DL - 0.025	<DL - 0.045	0.002	<DL - 0.01
8	0.102	0.003	<DL	<DL - 0.008	<DL - 0.041	<DL - 0.887	0.002	0.026
9	0.092	0.011	<DL	<DL - 0.019	<DL - 0.006	<DL - 0.013	0.002	0.015
10	0.109	0.004	<DL	<DL - 0.014	<DL - 0.02	<DL - 0.001	0.001	0.003
11	0.016	0.001	<DL	<DL - 0.022	<DL - 0.021	<DL	0.002	0.032
12	0.021	0.003	<DL	<DL - 0.006	<DL - 0.038	<DL	0.017	0.016
13	0.125	0.003	<DL	<DL - 0.029	<DL	<DL - 0.083	0.002	0.017
14	0.025	0.002	<DL	<DL	<DL	<DL	0.001	0.017
15	0.859	0.304	<DL	<DL - 0.059	<DL - 0.034	<DL	0.001	0.043
16	0.013	0.001	<DL	<DL - 0.003	<DL	<DL - 0.015	0.001	0.012
17	0.089	0.003	<DL	<DL - 0.012	<DL - 0.009	<DL - 0.002	0.002	0.032
18	0.188	0.007	<DL	<DL - 0.032	<DL - 0.029	<DL - 0.361	0.002	0.072
19	0.018	0.002	<DL	<DL - 0.018	<DL	<DL	0.001	0.023
20	0.110	0.004	<DL	<DL	<DL	<DL	0.002	0.018
21	0.091	0.010	<DL	<DL	<DL - 0.002	<DL	0.002	0.058
22	0.034	0.003	<DL	<DL	<DL - 0.017	<DL	0.002	0.032
23	0.013	0.002	<DL	<DL - 0.013	<DL - 0.029	<DL	0.001	0.034
24	0.020	0.002	<DL	<DL - 0.025	<DL - 0.023	<DL	0.002	0.014
25	0.142	0.003	<DL	<DL - 0.007	<DL - 0.007	<DL - 0.107	0.001	0.032
26	0.011	0.003	<DL	<DL - 0.033	<DL - 0.006	<DL	0.002	0.019
27	0.047	0.005	<DL	<DL	<DL	<DL - 0.041	0.002	0.040
28	0.025	0.004	<DL	<DL - 0.044	<DL - 0.056	<DL - 0.237	0.002	<DL - 0.022
29	0.075	0.002	<DL	<DL - 0.011	<DL - 0.04	<DL - 0.032	0.002	<DL - 0.007
30	0.195	0.198	<DL	<DL	<DL - 0.005	<DL	0.002	0.056
JS 286/2008*	1	0.1	0.07	1	0.01	4	0.003	0.05

These low trace-metal concentrations measured in the groundwater samples probably indicate a gelogenic origin. It is believed that the primary source of dissolved metals to groundwater is not probably metals leached from the surrounding rocks and soils, but rather released from aquifer materials (water-rock interaction). It can also be suggested that the groundwater aquifer is not significantly recharged from the surface runoff; the recharge rate from the surface water is low or negligible. This is consistent with the low and erratic annual precipitation rate occurring in the region.

On the other hand, metals may have been released from aquifer sediments and/or leached from soils during events of intense rainfall (occurs as flash flood),They have been either precipitated due to near-neutral pH and oxidizing conditions, or adsorbed onto metal oxides and clays. Metal release from aquifer sediment is affected by pH and salinity, where the lower pH and salinity are, the higher the metals that are released (Gambrell et al., 1990; Lau and Chu, 1999). Therefore, the mobilization of the metals from aquifer materials to groundwater is not preferential due to the coupling effect of the relatively high levels of salinity and pH in the water. In addition, flash rainfall events occurring in the region do not allow metal release from rocks as the flow path is rather short.

Previous data were obtained in regard to trace-metal contents in some groundwater wells (Table 6) representing the period before ZRC was established. While both data exhibited low levels of trace metals in the water samples, slightly higher contents were constantly observed in the current study compared to previous data.

Table 5. Available data about trace metals (mg/L) in water from selected wells prior to the ZRC establishment.

Well No.	Fe	Mn	Ni	Cu	Pb	Zn	Cd	Cr
2	-	<0.01	<0.01	<0.01	<0.01	-	-	0.01
3	<0.1	0.04	<0.01	0.1	<0.01	-	-	0.02
4	-	<0.10	<0.02	<0.02	<0.02	-	<0.06	-
5	-	<0.01	<0.01	<0.01	<0.01	-	-	0.01
6	0.01	0.01	0.01	0.01	0.01	0.01	0.01	0.01
7	<0.10	<0.02	<0.02	<0.02	-	<0.06	-	0.01
9	0.06	0.01	<0.01	0.01	0.05	0.09	-	<0.02
10	0.02	<0.005	<0.01	<0.02	<0.005	<0.02	<0.003	0.006
11	<0.10	<0.02	<0.02	<0.02	-	0.06	<0.003	0.02
12	-	<0.01	<0.01	<0.01	<0.01	-	-	0.01
16	-	<0.01	<0.01	<0.01	-	-	<0.003	<0.01
17	-	0.007	<0.01	<0.01	<0.01	-	<0.003	<0.01
18	0.08	0.02	<0.01	0.01	-	<0.04	-	0.0142
20	<0.1	<.01	<0.01	<0.01	<.01	<.06	-	<.01
22	<0.1	<0.02	<0.02	<0.02	-	<.06	-	<.02
23	-	<.01	<0.01	<0.01	<.01	<.06	-	0.02
24	<0.1	<.01	<0.01	<0.01	<.01	<.06	-	0.01
25	<0.1	<.01	<0.01	<0.01	<.01	<.06	-	0.01

5. Conclusions

This study was conducted to assess the groundwater quality within ZRC and the surrounding areas. ZRC is the largest Syrian camp in Jordan and was built within the Amman-Zarqa Basin, a major groundwater aquifer system in Jordan. With few exceptions. The majority of water quality parameters showed values that are within the permissible limits based on Jordan standards for drinking water. Groundwater quality is impacted by the weathering of rocks, uncontrolled and intensive pumping, dissolution of aquifer materials and the leaching of soluble salts following irregular rainfall events. This study confirms that groundwater wells located in ZRC and its nearby area are generally of a better quality compared to others. These wells are properly controlled and managed with the aid of the UN and other humanitarian agencies. Having said this, evidences of water quality deterioration were observed in the current study compared to data before 2012 (before ZRC was established).The inflow of Syrian refugees has certainly increased the demand for water, which exacerbated the water supply problems and will inevitably impact groundwater quality, though immediate risks to groundwater quality are not very likely.

Acknowledgment

The work was funded by the Deanship of Scientific Research/ Al al-Bayt University, Jordan. The authors would like to thank Al al-Bayt University for supporting this project. The suggestions of the anonymous reviewers who greatly contributed to the final version of this article are also highly acknowledged.

References

Al Mahamid, J. (2005). Integration of Water Resources of the Upper Aquifer in Amman- Zarqa Basin based on Mathematical Modeling and GIS, Jordan, PhD Dissertation, Freiberg University, Freiberg Online Geosciences12:223.

Al-Harahsheh, S., Al-Adamat, R., Abdullah, S. (2015). The Impact of Za'atari Refugee Camp on the Water Quality in Amman-Zarqa Basin. Journal of Environmental Protection 6: 16-24. doi: 10.4236/jep.2015.61003.

Al-Rawabdeh, A., Al-Ansari N., Al-Taani, A. A., Al-Khateeb, F., Knutsson, S.(2014). Modeling the Risk of Groundwater Contamination using Modified DRASTIC and GIS in Amman-Zerqa Basin, Jordan. Central European Journal of Engineering4: 264–280.

Al-Rawabdeh, A., Al-Ansari, N., Al-Taani, A. A., Knutsson, S. (2013). A GIS- based Drastic Model for Assessing Aquifer Vulnerability in Amman-Zerqa Groundwater Basin, Jordan. Engineering 5:490–504.

Al-Taani, A. A. (2013).Seasonal Variations in Water Quality of Al-Wehda Dam North of Jordan and Water Suitability for Irrigation in summer. Arabian Journal of Geosciences 6:1131–1140.

Al-Taani, A. A. (2014). Trend analysis in water quality of Al-Wehda Dam, North of Jordan. Environmental Monitoring and Assessment 186:6223–6239.

Al-Taani, A. A., Batayneh, A., El-Radaideh, N.,Al-Momani, I., Rawabdeh, A.(2012). Monitoring of Selenium Concentrations in major Springs of Yarmouk Basin, North Jordan. World Applied Sciences Journal18:704–714.

Al-Taani, A. A., El-Radaideh, N., Al Khateeb, W., Al Bsoul, A.(2018b). Reservoir Water Quality: A case from Jordan. Environmental Monitoring and Assessment190: 604. https://doi.org/10.1007/s10661-018-6976-9.

Al-Taani, A. A., El-Radaideh, N., Al-Khateeb, W. (2018a). Status of Water Quality in King Talal Reservoir Dam, Jordan. Water Resources 45:603-614.

APHA (American Public Health Association) (1998). Standard Methods for the Examination of Water and Wastewater. Washington DC: APHA, 20thEd.

Batayneh, A. and Al-Taani, A. A. (2015). Integrated Resistivity and Water Chemistry for Evaluation of Groundwater Quality of the Gulf of Aqaba Coastal Area in Saudi Arabia. Geosciences Journal 20:403 - 413.

Batayneh, A.,Zaman, H., Zumlot, T., Ghrefat, H., Mogren, S., Nazzal, Y., Elawadi, E., Qaisy, S., Bahkaly, I., Al-Taan, A.(2014). Hydrochemicalfacies and Ionic Ratios of the Coastal Groundwater Aquifer of Saudi Gulf of Aqaba: Implication for Seawater Intrusion.Journal of Coastal Research 30:75-87.

Bender, F. (1974). Geology of Jordan, Gebrueder Borntraege, Berlin.

Chadha, D. K. (1999). A proposed new Diagram for Geochemical Classification of Natural Waters and Interpretation of Chemical Data. Hydrogeology Journal 7:431– 439.

Gambrell, R.P., Wiesepape, J. B., Patrick, W. H., Duff, M. C. (1991). The Effects of pH, Redox and Salinity on Metal Release from a Contaminated Sediment. Water, Air and Soil Pollution 57:359-367.

Gharaibeh, A. (2003). Geological map of Umm Al Jimal. Natural Resources Authority. Umm Al Jimal map Sheet 3245-I, scale 1:50.000.

Gibbs, R. (1970). Mechanisms Controlling World Water Chemistry. Science170:1088– 1090.

JS (Jordanian Standards 286). (2008). Water -Drinking Water,

JJEES

JJEES (2020) 11 (4) 272-281
ISSN 1995-6681

Jordan Journal of Earth and Environmental Sciences

Mineralogical and Geochemical Characterization of Jarash Kaolinitic Clay, Northern Jordan

Talal Al-Momani*, Mohammad Alqudah,"Mohammed-Ezz-Aldien" Dwairi

Yarmouk University, Faculty of Science, Department of Earth and Environmental Sciences, Jordan.

Received 26 January 2020, Accepted 18 June 2020

Abstract

Kaolinite-rich beds occur in Jarash area, northern Jordan. The major chemical components of Jarash kaolinitic clay are SiO_2, Al_2O_3 and Fe_2O_3 with average values of 61.0% (range = 47.5 - 78.1%), 19.77% (range = 10.8 - 26.33%), 4.58% (range = 1.41 - 10.15%) respectively. Other oxides (K_2O, TiO_2, CaO, MgO, and MnO) are present as minor components. The low Al_2O_3 and high Fe_2O_3 values indicate a low-grade clay deposit. The XRD results have indicated that kaolinite and quartz are the major mineral constituents, while smectite and muscovite/illite are the minor constituents. The SEM and TEM photomicrographs have indicated that kaolinite is well crystalline with euhedral to subhedral pseudohexagonal forms. IR spectroscopy results indicate that the kaolinite is moderate to well crystalline. The thermographs (DTA/TGA results) confirm the thermal behavior of kaolinite as the structure decomposes at ~ 900°C.

The chemical, mineralogical, physical, and technical characteristics of Jarash kaolinitic clay (after attrition and wet sieving) have indicated its possible suitability for pottery, ceramic tiles, and brick-making industries.

Keywords: Clay, Characterization, Kaolinite, Ceramics, Jarash, Jordan.

1. Introduction

Clay minerals constitute about 16% of the total volume of sedimentary rocks on the Earth's surface (Khoury, 2002). The term clay refers to the sediments when consisting of grains the size of less than 2 μm in diameter. The claystone usually consists of a mixture of clay minerals and other rock debris of varying composition (Khoury, 2002; Khoury et al., 2008). Kaolinite, the most common clay mineral, is a 1:1 layered silicate composed of alternating layers of $[Si_2O_5]^{2-}$ and $[Al_2(OH)_4]^{2+}$. The theoretical formula of kaolinite is $Si_2Al_2O_5(OH)_4$ (frequently expressed as $Al_2O_3.2SiO_2.2H_2O$). Kaolin deposits contain kaolinite together with other clay minerals, e.g., smectite and illite (Correia et al., 2005).

Clays have played a very important role in the industrial technology in recent years; kaolinite is one of the most important and widely-distributed clay minerals (Murray 2007; Dominguez et al., 2016; Abu Yaya et al., 2017; Kharbish and Farhat, 2017). The outstanding chemical and physical properties of kaolinite enable its use in agricultural, engineering, and construction industries. Kaolinite is used as an important commodity in ceramic, paper, plastic, rubber, cement, clay bricks, geopolymers, paint, cosmetic, and many other industries (Ciullo, 1996; Murray 2007; Al Ani and Sarapaa, 2008; Attah and Oden, 2010; Kashcheev and Turlova, 2010; Khoury 2019).

Kaolinite is used in many applications such as paper filling and coating (45 %), refractories and ceramics (31 %), fiberglass (6 %), cement (6 %), rubber and plastic (5 %), paint (3 %), and other industries (4 %) (Eletta et al., 2015). Technological properties of ceramic products depend on the physical, chemical, and mineralogical characteristics of the starting raw materials, which also control the overall processing before firing (Correia et al., 2005).

In Jordan, kaolinite-rich beds occur in Mahis, Ghor-Kabid, Batn El-Ghoul, and Hiswa areas (Khoury 2002; 2006). The Jordanian kaolinite was characterized by many authors (i.e. Khoury and El-Sakka, 1986 ; Al-Momani, 2000, 2008; Qtaitat and Al-Trawneh 2005; Al-Momani and Khoury, 2010; Gougazeh and Buhl 2010; Al-Momani and Dwairi, 2018; Khoury 2002; 2019). Kaolinite is used in the cement industry, ceramics (sanitary ware and tiles, artistic ceramic ware, table-ware kitchen-ware, and stone-ware (pipes and tiles). The estimated kaolin reserves in various areas in Jordan are as follows: Batn el-Ghoul (2200 Mt), Al-Mudawwara (9700 Mt), Al-Hiswa (54 Mt), and Jabal Umm Sahm and Dubaydib (1090 Mt) (Yasin and Ghannam, 2006).

The geology (sedimentology, paleogeography, structures, mineralogical and engineering behavior of some clay) and depositional environments of Jarash kaolinitic clay were investigated by many authors (Amireh 1994; Ahmad et al., 2012; Abu Hamad et al., 2016).

The following work aims for the first time to characterize and investigate the possible industrial use of the clay deposits in Jarash, northern Jordan.

* Corresponding author e-mail: talalmom@yu.edu.jo

2. Geological Setting of the Study Area

Jarash clay deposits belong to the Early Cretaceous Kurnub Group of Jordan (Table 1) that crops out in many sites of Jordan including the studied area. In northern Jordan, the Kurnub Group (KG) is subdivided into three formations; Ramel, Jarash, and Bir Fa'as from base to top (Amireh and Abed, 1999; Amireh, 2000).

Amireh (1994) used heavy and clay minerals as an effective tool for solving stratigraphic problems. The heavy and clay minerals have been applied on the Kurnub Sandstone (Early Cretaceous) of Jordan. Ahmad et al. (2012) performed a palynological study on the Early Cretaceous Kurnub Sandstone Formation from Mahis area, central Jordan. Their data was correlated with Abu Hamad et al. (2016) results from the Jarash Formation (Aptian–Albian, Kurnub Group) of northern Jordan.

Figure (1) illustrates the geology of the studied area. Jarash clay deposits belong to the Lower Cretaceous Sandstone (Aptain-Albian age) which consists mainly of clastic sedimentary rocks including dominant sandstones with intercalation of claystones (Amireh, 1997; Abdelhamid, 1995). The studied claystones in the Jarash area are intercalated within the sandstone layers of the Jarash Formation.

Table 1. General Stratigraphy of the Kurnub Group and Jarash Formation in the studied area (Amireh and Abed, 1999).

Era	Period	Series	Group	Formation	Age
Mesozoic	Cretaceous	Upper Cretaceous	Ajliun Group	Na'ur	Turonian
					Cenomanian
		Lower Cretaceous	Kurnub Group	Bir Fa'as	Albian
				Jarash	
				Ramel	Aptain

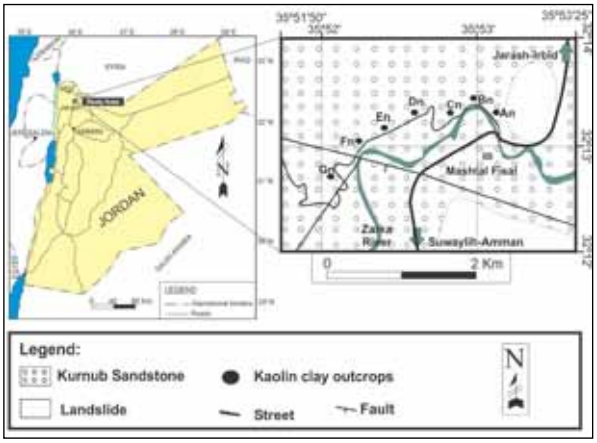

Figure 1. Geological map of the studied area (Modified from Sawariah and Barjous, 1993; Royal Jordanian Geographic Center, 2003).

3. Methodology

Field-work and sampling were carried out during summer 2015 and have focused on the Jarash clay deposit that is located 38 km to the south of Irbid city and around 45 km to the north of Amman city. The site coordinates are 32° 12′ 00″ N – 32° 14′ 00″ N and 35° 51′ 50″ E – 35° 53′ 25″ E (Figure 1).

110 representative samples were collected from the clay outcrops [seven bulk samples before and after attrition and wet sieving; ninety-six from the different seven outcrops (An, Bn, Cn, Dn, En, Fn, and Gn)]. Attrition and wet sieving were carried out for the bulk samples.

The attrition scrubbing can be referred to as the first step of the wet sieving. The main objective of this process is to separate the fine particles by water and to increase the scoring action of the coarse particles with each other (Preston and Tatarzyn, 2013). Wet sieving was used to separate the fine particles from the coarse particles and to eliminate the major impurities (Bloodworth et al., 1993; Sandgren et al., 2015). Laboratory attrition scrubber model (IKA-Werk TR-50) was used in this study. The wet sieving was done according to the method of (Bloodworth et al., 1993), British Geological Survey.

Characterization of the clay samples has included detailed chemical analyses for major and trace components using X-ray fluorescence (XRF) and Inductively-coupled plasma (ICP-AES) techniques, mineralogical analysis using X-Ray diffraction (XRD), Infrared Spectroscopy (IR), Scanning electron microscopy (SEM), Transmission electron microscope (TEM), differential thermal (DTA), differential thermogravimetric (DTG) and thermogravimetric analyses (TGA) techniques.

The X-ray fluorescence (XRF) was used in the analysis of the major oxides (Si, Al, Fe, Ti, Mg, Ca, Mn, Na, K, P) using Bruker axs XRF-S4. The samples were analyzed at the laboratories of the Ministry of Energy and Mineral Resources – Amman. A 0.7 gm of each powdered sample was weighted in a clean platinum crucible. Each sample was mixed with 7 gm of flux [1 part Li – tetra borate and 4 parts Li – Meta borate] then was fused in a platinum crucible at 1200˚C for five minutes using a standard burner. After cooling, glass discs were used for major elemental analysis.

Fourteen bulk representative samples were analyzed for their trace elements' content (Be, B, Ba, Cd, Co, Cr, Cu, Li. Mo, Nb, V, Pb, Sn, Sr, Y, Zr, Bi, As and W) using Quantima ICP – AES.

Bruker D4 ENDEAVOUR diffractometer with Cu kα radiation (λ = 1.5418) and a scan rate speed of 2˚/min at 40 kV and 30 mA were used to obtain the X-ray diffractograms for the whole rock samples that were scanned from 2˚ - 65˚ 2θ. The oriented clay samples were scanned from 2˚ - 30˚ 2θ for untreated, glycolated and heated (550˚C) preparations following the procedure of (Poppe et al., 2001, Hutchison, 1974).

Undisturbed clay samples (5 to 10 mm in length) were prepared for SEM analysis. The samples were coated with gold to produce clear and high resolution images (Welton, 2003). FEL-Quanta 200 instrument was used with a magnification range from 1000 to 30,000X (5000X to 20,000X was the most useful).

A transmission electron microscope (TEM) (ZEISS EM 10 TR) was used. TEM micrographs usually give information about the shape, size, and the arrangement of the particles. It also gives more detailed information on the crystallographic and the compositional nature of the particle (William and Carter, 2009). Fifteen representative samples were prepared by dispersing a small portion of the <63 µm fraction using an ultrasonic device. A small amount of this dispersed material was sprayed onto grids, and was supported by a thin carbon film, dried, and mounted in the microscope.

The IR spectroscopy is usually used to focus on the degree of crystallinity of kaolinite (Djomogue and Njopwovo, 2013; Johnston, 2017; Kloprogge, 2017; Madejová, et al., 2017). Potassium Bromide (KBr) pellets after wet sieving were prepared for seven representative samples using FT-IR (Bruker FT-IR- 4100) instrument over the range of 400 to 4000 cm^{-1}.

Thermal analyses are used to study the properties of the materials as a result of changing in temperature. In addition, mass change, phase diagrams, and thermal capacity can be obtained through these analyses. The differential thermal analysis (DTA) gives information about endothermic or exothermic reactions. The endothermic reaction describes desorption of surface H_2O, dehydration at low temperature and dehydroxylation at 550°C. On the other hand, crystallization through exothermic reaction takes place at high temperature (>900°C) to form mullite. The thermogravimetric analysis (TGA) determines the mass change with the increase of temperature (Guggenheim and Koster, 2001). The DTA, DTG, and TGA analyses were made using NETZSCH STA 409 PG/PC.

4. Results and Discussion

4.1. XRF Results before and after Attrition and Wet Sieving

The XRF results of the seven bulk samples are given in Table (2). The SiO_2, Al_2O_3, Fe_2O_3, and LOI are the major components, while TiO_2, K_2O, MnO, MgO, CaO, P_2O_5 are relatively minor components. SiO_2 and Al_2O_3 are usually the main chemical constituents of kaolinite, quartz, and illite. The XRF results after attrition and wet sieving (<63µm) for all of the samples are also given in Table (2).

Table 2. Maximum, minimum, and average values (wt. %) of the major oxides before and after attrition and wet sieving of the seven bulk Jarash clay samples.

Oxides (wt.%)	Minimum Value		Maximum Value		Average Value		Standard Deviation	
	Before	After	Before	After	Before	After	Before	After
SiO_2	62.5	47.5	85.13	78.60	73.75	61.00	7.22	7.07
TiO_2	0.72	1.06	1.77	2.33	1.303	1.75	0.30	0.25
Al_2O_3	7.54	10.8	20.70	26.33	12.69	19.77	4.10	3.79
Fe_2O_3	1.30	1.41	5.17	10.15	2.912	4.58	1.25	1.74
MnO	0.00	0.00	0.1	0.058	0.008	0.006	0.025	0.01
MgO	0.15	0.24	0.83	1.16	0.293	0.59	0.163	0.23
CaO	0.11	0.21	1.49	10.3	0.720	1.22	0.491	1.46
Na_2O	0.00	0.00	0.18	1.78	0.029	0.058	0.05	0.22
K_2O	0.00	0.05	1.46	1.88	0.864	1.27	0.34	0.20
P_2O_5	0.03	0.029	0.08	0.21	0.044	0.09	0.014	0.004
LOI	3.00	4.4	8.00	16.6	5.54	9.35	1.374	2.20

Table 2 shows that the trend for major oxides' readings before and after wet sieving and attrition. Silica is the highest value, followed by alumina and iron oxides. The table shows also that silica has decreased, and alumina and iron oxides have increased after wet sieving and attrition.

Increased iron content in the clay-rich fraction indicates the presence of iron oxides as fine-grained particles (Jovanovic and Mujkanovic, 2013). Iron oxide (Fe_2O_3) in the clay fraction is detrimental to the clay's effective performance as a refractory material; it then became imperative to reduce it to an acceptable level of less than 1% by leaching with oxalic acid (Al-Momani 2008; Abd El-Raheem et al., 2009; Florunso et al., 2014).

Correlation Coefficient matrix for the major oxides is given in Table (3). This Table exhibits a high negative correlation between Al_2O_3 and SiO_2 (-0.77), Fe_2O_3 and SiO_2 (-0.81), and LOI and SiO_2 (-0.84). A high positive correlation between LOI and Al_2O_3 (0.73) indicates its relation to kaolinite.

Table 3. Correlation Coefficient matrix for the major oxides in the (96) representative Jarash clay samples. Correlation is significant at the 0.05 level.

	SiO_2	Al_2O_3	Fe_2O_3	TiO_2	Na_2O	K_2O	MnO	MgO	CaO	P_2O_5	LOI
SiO_2	1	-0.77	-0.81	-0.42	0.19	-0.40	-0.44	-0.47	0.36	-0.27	-0.84
Al_2O_3		1	0.42	0.43	-0.39	0.41	-0.77	0.41	-0.33	0.36	0.73
Fe_2O_3			1	0.26	0.006	0.28	0.52	0.50	-0.32	0.20	0.70
TiO2				1	-0.544	0.27	0.083	0.081	-0.221	0.17	0.35
Na_2O					1	-0.71	0.060	-0.003	0.203	-0.17	-0.15
K_2O						1	0.080	0.341	-0.100	0.17	0.42
MnO							1	0.065	-0.30	0.062	0.19
MgO								1	0.260	0.48	0.71
CaO									1	-0.047	0.011
P_2O_5										1	0.52
LOI											1

4.2. ICP Results

The ICP results of the trace elements for the bulk samples before and after attrition and wet sieving (grain size <63µm) are given in Table (4).

Table 4. Minimum, maximum, average (ppm), and standard deviation values for the different trace elements before and after attrition and wet sieving.

Trace Element (ppm)	Minimum		Maximum		Average		Standard Deviation	
	Before	After	Before	After	Before	After	Before	After
As	77	69	360	276	186	165	244.7	86.03
B	57	41	100	128	70	82	14.4	26.2
Ba	166	197	245	266	206	229	29.9	27.6
Be	2	3	3	3	3	3	0.577	0.0
Bi	ND	ND	ND	ND	ND	ND	ND	ND
Cd	1	3	32	9	16.3	6	22.13	4.24
Co	5	1	73	12	28	8	30.43	4.65
Cr	82	89	125	193	98	156	13.9	40.3
Cu	3	2	8	10	4	3	2.24	2.66
Li	18	31	55	67	35	48	13.1	13.9
Mo	ND	ND	ND	ND	ND	ND	ND	ND
Nb	7	22	59	71	33	43	20.42	19.4
Pb	17	20	119	168	55	100	44.7	74.73
Sn	9	24	169	79	78	52	60.75	27.54
Sr	137	154	300	386	217	274	61.7	72.15
V	77	91	118	149	93	120	16.3	20.7
W	47	34	64	116	55	66	12.02	35.1
Y	30	32	44	54	36	43	4.99	7.71
Zr	232	258	1249	483	568	351	433.9	83.6

(ND: Not Detected).

Some trace elements are enriched in the original samples, and could be incorporated in the non-clay heavy minerals. Other trace elements are enriched in the fine fraction (<63 µm), and could be incorporated in the structure of the clay minerals (Khoury, 2002). The results of trace elements in the Jarash clay samples after wet sieving (<63µm) show that Zr > Sr > Ba > As > Cr > V > Pb > B > W < Sn > Li > Nb > Y > Co > Cd > Cu > Be. The <63µm size fraction indicates a relatively high concentration of Zr (Average 568 and 351 ppm before and after attrition and wet sieving) that could be related to detrital zircon.

Trace elements are a significant factor in coloring the clay industrial products, and could have a negative impact on the environment through the accumulation of toxic elements in plants, water, and soils (Hou and Jones, 2000).

4.3. X-ray Diffraction (XRD)

The results of X-ray diffraction analysis of the samples before attrition scrubbing and wet sieving indicate that quartz and kaolinite are the most abundant minerals in all the samples. The strongest (highest) peaks for quartz appear at d-spacings=3.34 Å (2θ= 26.67) and 4.26 Å (2 θ= 20.85). Kaolinite major peaks appear at d-spacings 7.17 Å (2 θ= 12.34) and 3.58 Å (2 θ= 24.88). Muscovite/illite, calcite, and smectite are found as minor constituents.

Typical oriented XRD clay results for the normal (air dried), glycolated, and heated at 550 °C preparations are illustrated in Figure (2). Kaolinite is characterized by two basal reflections: (001) and (002). The first reflection appears at 7.15 Å, the second one appears at 3.56 Å. Kaolinite reflections are not affected by glycolation, but they disappear upon heating to 550 °C.

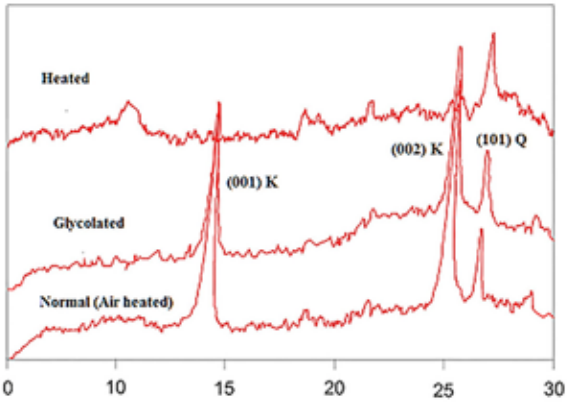

Figure 2. Typical oriented XRD patterns for air-dried, glycolated, and heated to 550 °C sample (Dn2). The number between the brackets indicates hkl reflections. (K: Kaolinite and Q: Quartz).

4.4. Scanning Electron Microscope (SEM)

The crystal shape, texture, and morphology of kaolinite from Jarash clay is obtained from the SEM micrographs as illustrated in Figure (3). Kaolinite is well crystalline with an euhedral pseudohexagonal form, and its particle size ranges between 1 and 4 µm.

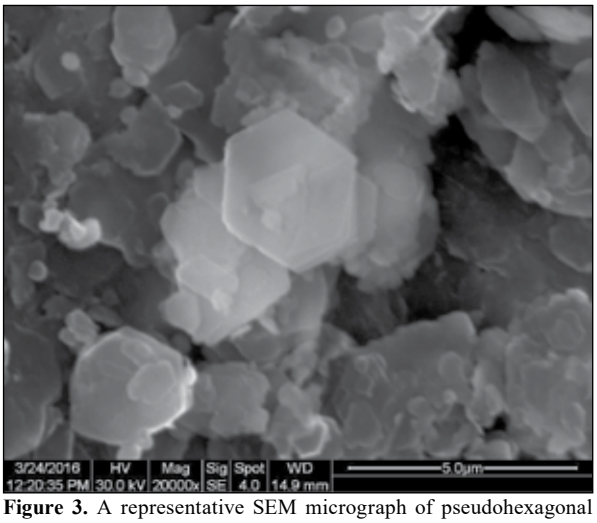

Figure 3. A representative SEM micrograph of pseudohexagonal kaolinite from Jarash clay (20000X) (Sample No. Fn1).

4.5. Transmission Electron Microscopy (TEM)

Kaolinite has a pseudohexagonal form (euhedral to subhedral) with a particle size that ranges between 200 and 300 nm. Figure (4) shows a typical TEM micrograph of the Jarash kaolinite.

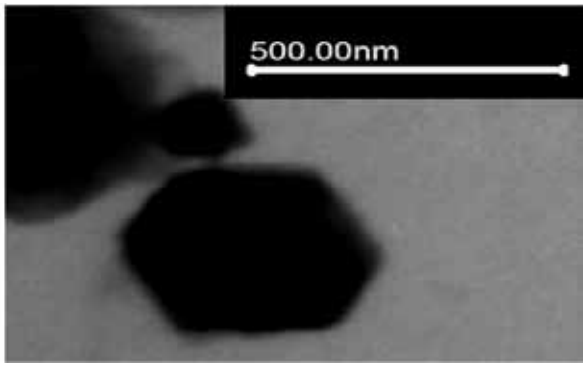

Figure 4. Transmission electron micrograph of well-crystalline pseudohexagonal kaolinite from Jarash clay deposit (Sample No. Bn2).

4.6. Infrared Spectroscopy (IR)

Theoretical kaolinite shows high-intensity absorption peaks at 3694, 3650, 3620, 1114, 1032, 1010, 936, 912, 790, 752, 693, 537, 468, 430 cm^{-1} Ekosse (2005).

Kaolinite $[Al_2Si_2O_5(OH)_4]$ is made up of four well-resolved absorption bands of the hydroxyl group (OH-) which are located at 3695 cm^{-1}, 3670 cm^{-1}, 3650 cm^{-1}, and 3620 cm-1. The high frequency bands are located at 3670 cm^{-1} and 3695 cm^{-1}, the medium frequency is at 3950 cm^{-1}, while the low-frequency bands are located at 3620 cm^{-1}, 3670 cm^{-1}, 3695 cm^{-1} and 3650 cm^{-1}, due to the vibration of the external hydroxyls, through the 3620 cm^{-1} which is described as the inner hydroxyls (Vaculikova et al., 2011; Madejová, et al., 2017).

Infrared spectroscopy (IR) results of selected samples after attrition and wet sieving (< 63 µm) are illustrated in Figure (5). The figure shows a high-intensity absorption band at 3699.99 cm-1, and at 3620.02 cm^{-1}, medium intensity peak at 1618.04 cm^{-1}, and low intensity peaks at 1031.42 cm^{-1}, 912.92cm^{-1}, and at 469.41 cm^{-1} that indicate a moderate to well crystalline kaolinite when compared to Vaculikova et al. (2011) and Madejová, et al. (2017).

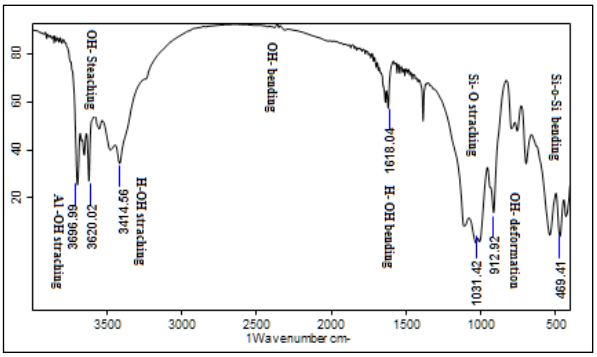

Figure 5. Infrared absorption spectra of Jarash clay from 400 to 4000 cm-1 after attrition and wet sieving (Sample An15).

4.7. DTA-TG Analyses

The DTA results of Jarash clay have indicated that kaolinite is the major clay component. Figures (6 and 7) show the first endothermic peaks range from 150°C to 200°C. The main dehydroxylation endothermic peaks ranges from 500°C to 550°C that indicate the decomposition of kaolinite. A small exothermic peak appears at a range from 880°C to 940°C that is related to the recrystallization process.

The DTG and TG results are illustrated in Figures (6 and 7). It indicates a total loss in weight that ranges from 8 % to 18 %, and is related to dehydration and dehydroxylation. The loss of weight as a result of dehydroxylation of pure kaolinite is 14 % (Eslinger and Peaver, 1988). The dehydroxylation of Jarash clay ranges from 5 % to 9.5 % which means that the samples include other minerals as quartz.

The dehydroxylation process of kaolinite occurs at temperatures ranging from 400 to 700°C, Table (5) (Kakali et al., 2001; Erdemoğlu et al., 2020).

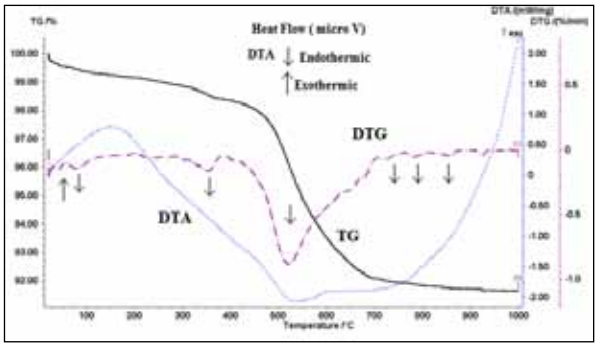

Figure 6. Typical thermal curves (DTA, TG, and DTG) for Jarash clay. (Heating rate = 20°C /min).

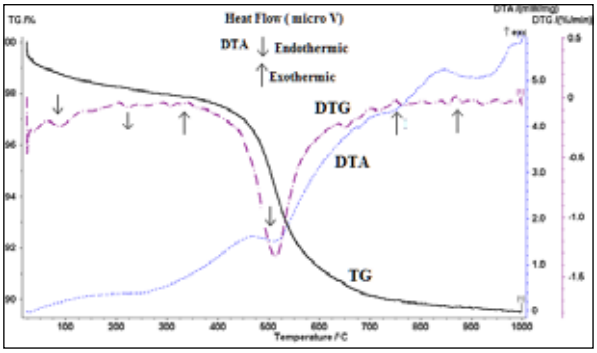

Figure 7. Typical thermal curves (DTA, TG, and DTG) for Jarash clay (Heating rate= 20°C /min).

The XRD, SEM, TEM, IR, DTA and TGA results confirm that the kaolinite of Jarash clay is well crystalline and the (< 63 µm) size fraction is mixed with quartz as a non-clay mineral.

4.8. Possible Industrial Applications

Table (6) summarizes the main chemical constituents of kaolinite deposits of Jordan including this study. Table (7) is a comparison between the average chemical composition of Jarash clay and some selected clay deposits around the World.

Table 5. Thermal transformation stages of kaolinite.

Mineral	Temperature	Thermal transformation phase	Reference
Kaolinite	T<100°C	Low temperature release of absorbed water in pores, on the surfaces.	Kakali et al. (2001)
Kaolinite	100<T<400°C	Weight loss that can be correlated with a pre-dehydration process.	Kakali et al. (2001)
Kaolinite	T<400°C	Removal of surface, pore, and adsorbed water	Erdemoğlu et al. (2020)
Kaolinite	400<T<650°C	Dehydroxylation of kaolinite	Kakali et al. (2001)
Kaolinite	400°C<T<700°C	Dehydroxylation	Erdemoğlu et al. (2020)
Kaolinite	T = ~1000°C	Crystallization of mullite	Kakali et al. (2001)
Kaolinite	T = ~1000°C	Formation of mullite phase and amorphous SiO_2	Erdemoğlu et al. (2020)
Kaolinite	T >1200°C	Crystallization of cristobalite from amorphous SiO_2	Erdemoğlu et al. (2020)

Table 6. Chemical composition of kaolinite clay deposits of Jordan (Alshaaer et al., 2002; Khoury, 2002; Yasin and Ghannam, 2006; AL-Momani, 2008; AL-Momani and Khoury, 2010; present study).

Area	Al_2O_3%			SiO_2%			Fe_2O_3%		
	Min.	Max.	Aver.	Min.	Max.	Aver.	Min.	Max.	Aver.
Batn El-Ghoul	14.01	25.37	19.30	47.79	68.32	56.66	4.05	8.37	7.33
Al-Mudawwara	13.36	27.54	18.97	41.87	70.20	54.95	4.54	10.54	7.91
Al-Hiswa	15.62	28.96	19.25	46.60	66.47	58.73	1.38	9.58	9.15
Jabel Umm Sham and Dubaydib	17.00	24.70	22.52	49.04	61.67	51.50	3.50	11.04	5.52
Jarash Clay (Present Study)	10.8	26.33	19.77	47.5	78.60	61.00	1.14	10.15	4.58

Table 7. Average chemical composition of Jarash clay deposits compared with other clay deposits around the world (wt %).

Oxide (wt. %)	This study	Other Kaolinite deposits in the world			
		Italy	Nigeria	Jordan	Typical chemical composition of clay materials for ceramic tiles from different countries. (AL-Momani, 2000)
		I	II	III	
SiO_2	61.00	65.43	60.21	58.73	44.9 - 70.0
Al_2O_3	19.77	19.61	19.05	19.25	19.61 - 32.0
Fe_2O_3	4.58	5.72	3.78	9.15	0.5 - 8.6
TiO_2	1.75	0.59	--	0.83	0.0 - 1.4
Na_2O	0.06	0.48	0.42	0.09	0.0 - 1.0
K_2O	1.27	1.3	2.16	1.39	0.5 - 1.98
MnO	0.006	--	0.02	0.04	--
MgO	0.59	0.15	1.50	0.16	0.05 - 1.96
CaO	1.22	0.16	0.30	0.05	0.0 – 1.0
P_2O_5	0.09	--	--	0.083	--
LOI	9.35	6.39	10.2	9.36	7.5 - 13.6

I. Clay from Sardinia Italy (Ligas et al., 1997).
II. Ibere and Oboro clay deposits in Nigeria (Mark, 2010).
III. Hiswa clay Kaolin A3 (AL-Momani, 2000; AL-Momani, 2008; AL-Momani and Khoury, 2010).

It is noted from Table (6) that the average concentration of aluminum oxide (Al_2O_3%) in the Jarash clay is higher than other different regions (Batn El-Ghoul, and Jabel Umm Sham and Dubaydib), with the exception of Al-Mudawwara and Al-Hiswa clay. In Jarash clay, the average silica oxide (SiO_2%) is higher and the iron oxide (Fe_2O_3%) is lower than other different regions (Al-Mudawwara and Jabel Umm Sham and Dubaydib).

The chemical composition of the Jarash clay deposits as indicated in Table (7) suggests its use as a raw material for refractories or ceramic (Al-Momani, 2000; Mark, 2010) and for the manufacture of vitrified tiles (Ligas et al., 1997; Al-Momani, 2000)

The chemical composition is consistent with those results obtained in a previous work on the physical and technical characteristics of the Jarash clay deposits (Al-Momani and Dwairi, 2018). The authors concluded that the bulk samples of Jarash clay after the attrition and wet sieving were plotted graphically in the region of the kaolinite, while some samples were plotted in the region of the plastic kaolin (Figure 8). Plastic kaolinite may be affected by the variations of liquid limit (LL), plastic limit (PL), and plasticity index (PI) in the different samples of Jarash clay. Using the clay workability sheet of Bain and Highly (1978), most of the bulk samples of Jarash clay fall within the region of optimum molding properties, and acceptable molding properties which indicate that Jarash clay is suitable for pottery, and brick-clay industry (Figure 9). In addition, the physical characteristics (whiteness, bulk density, and oil absorption), chemical characteristics, technical characteristics [liquid limit (LL), plastic limit (PL), and plasticity index (PI)] of Jarash clay after the attrition and wet sieving endorse that Jarash clay deposits is suitable for pottery, ceramic tiles, and brick-making industries (Table 8).

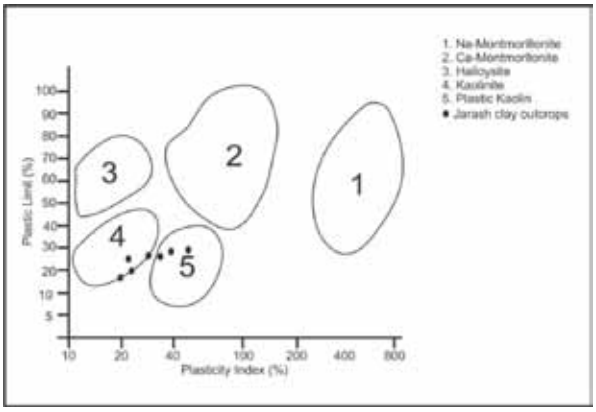

Figure 8. Clay identification for bulk samples after wet sieving and attrition for Jarash clay (<63µm) (Al-Momani and Dwairi, 2018).

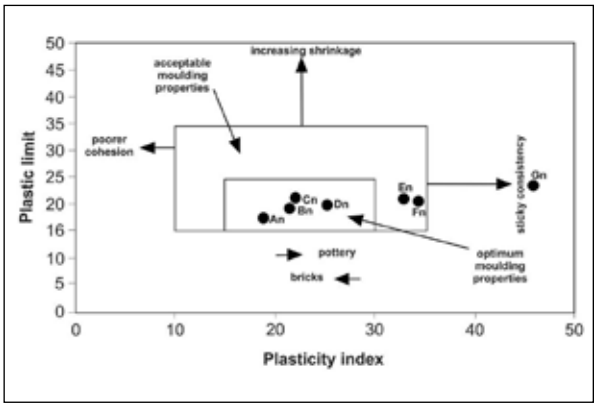

Figure 9. Clay workability chart for samples after wet sieving and attrition (<63 µm) (Al-Momani and Dwairi, 2018).

Table 8. Comparison between the typical chemical properties of clay materials for ceramic tiles.

The Present Study			Mark (2010)	AL-Momani, (2010)	Typical chemical composition of clay materials for ceramic tiles from different countries. (AL-Momani, 2000)
Chemical composition (wt. %)					
SiO_2%		61.00	60.21	58.73	44.9 - 70.0
Al_2O_3%		19.77	19.05	19.25	19.61 - 32.0
Fe_2O_3%		4.58	3.70	9.15	0.5 - 8.6
TiO_2%		1.75	--	0.83	0.0 - 1.4
Na_2O%		0.06	0.42	0.09	0.0 - 1.0
K_2O%		1.27	2.16	1.39	0.5 - 1.98
MnO%		0.006	--	0.04	--
MgO%		0.59	1.50	0.16	0.05 - 1.96
CaO%		1.22	0.30	0.05	0.0 - 1.0
P_2O_5%		0.09	-	0.08	--
LOI		9.35	10.2	7.14	7.5 - 13.6
Technical properties					
Plastic limit (Wt. %)	Range	15.9 - 26.3	19.0	18.09	16.0 – 26.0
	Average	19.74			
Liquid limit (Wt. %)	Range	34.2 - 71.5	42.4	30.05	23.0 – 42.0
	Average	48.18			
Plasticity index (Wt. %)	Range	18.3 - 45.2	23.0	11.96	9.0 – 26.6
	Average	19.74			
Physical properties					
Bulk Density (g/cm^3)	Range	0.86 - 1.22	1.66	0.69-1.33	
	Average	0.99			
Oil Absorption (g/100g)	Range	23.35 - 46.5	--	21.81-35.34	
	Average	33.1			

5. Conclusions

XRD, SEM, TEM, IR, DTA, DTG, and (TGA) results have confirmed that kaolinite is the major Jarash clay mineral constituent together with quartz. Small amounts of muscovite/illite and smectite are also present. Kaolinite of Jarash clay is well crystalline with a pseudohexagonal form and a crystal size that ranges between 1 and 4 µm.

The overall chemical results are comparable with other clay deposits in Jordan (Batn el-Ghoul, Al-Mudawwara, Al-Hiswa) and other countries (Nigeria and Italy).

The chemical, mineralogical, physical, and technical characteristics of Jarash clay after the attrition and wet sieving suggest its use in pottery, ceramic tiles, and brick-making industries.

Processing and treatment of Jarash clay should be used to increase the Al_2O_3 and reduce the Fe_2O_3 contents which can be achieved by different methods such as chemical leaching in order to meet the specifications of other ceramic industries.

Acknowledgements

First of all, the authors would like to express thanks to reviewers, editor–In-chief, and editing staff for their special efforts, supervision, fruitful discussion, critical reviewing, and concern to improve this work. The financial support from the Deanship of Scientific Research and Graduate Studies at Yarmouk University is gratefully acknowledged (Project number: 29/2015). Thanks are given to Prof. Dr. Ahmad Abu Hilal for his critical notes to improve this paper.

References

Abd El-Raheem, F.H., Selim, K.A., Abdel-Khalek, N.A. (2009). Some parametersaffecting beneficiation of fine kaolin particles. The Journal of Ore Dressing 11 (21): 1-8.

Abedlhamid, G. (1995). The Geology of Jarash Area, Map Sheet 3154-I, National Resources Authority, Amman.

Abu Hamad, A.H., Amireh, B. Jasper, A., Uhl., D. (2016). New Palaeobotanical data from the Jarash Formation (Aptian–Albian, Kurnub Group) of NW Jordan. The Palaeobotanist 65 (1): 19–29.

Abu Yaya, E. K., Tiburu, M.E., Vickers, J.K., Efavi, B., Onwona A., Kevin, M.K. (2017). Characterization and identification of local kaolin clay from Ghana: A potential material for electro porcelain insulator fabrication. Applied Clay Science 150: 125-130.

Ahmad, F., Abu hamad, A. Obidat, M. (2012). Palynological study of the Early Cretaceous Kurnub Sandstone Formation, Mahis area Central Jordan. Acta Palaeobotanica 52(2): 303-315.

Al Ani, T. and Sarapaa, O. (2008). Clay and Clay Mineralogy. Physical- Chemical properties and Industrial uses. Geological Survey of Finland, Finland.

Al-Momani, T.M. (2000). Characterization, Industrial Utilization and Environmental Impact of the Hiswa Clay Deposits, South Jordan. Ph.D. Thesis, University of Jordan. Jordan.

Al-Momani, T.M. (2008). Reducing the Iron Content of Hiswa Clay Deposits, South Jordan by Chemical Leaching. Abhath

AL-Yarmouk: "Basic Science and Engineering 17: 127-145.

Al-Momani, T.M. and Dwairi, M. (2018). Physical and technical characteristics of Jarash Clay deposits from northern Jordan. Jordan Journal of earth and environmental sciences 9: 81-88.

Al-Momani, T.M. and Khoury, H.N. (2010). Processing and Treatment of Hiswa Clay Deposits, South Jordan Using Hydrocyclone Separation and High Intensity Wet Magnetic Separation. Dirasat: Pure Sciences 37: 36-47.

Alshaaer, M., Cuypers, H., Wastiels, J. (2002). Stabilization of kaolinitic soil for construction purposes by using mineral polymerization technique. In: Resheidat, M. (Ed.), Proceedings of the 6th International Conference on Concrete Technology for Developing Countries. pp: 1085-1092, Jordan.

Amireh, B. (1994). Heavy and clay minerals as tools in solving stratigraphic problems: A case study from the Disi Sandstone (Early Ordovician) and the Kurnub Sandstone (Early Cretaceous) of Jordan. Neues Jahrbuch für Geologie und Paläontologie. Monatshefte 4: 205-222.

Amireh, B. (1997). Sedimentolgy and Paleography of the regressive-transgressive Kurnub Group (Early Cretaceous) of Jordan. Sedimentary Geology 112: 69-88.

Amireh, B. (2000). The Early Cretaceous Kurnub Group of Jordan: Subdivision. Neues Jahrbuch fur Geologie und Palaontologie Monatshefte 2000: 29-57.

Amireh, B. and Abed, A. (1999). Depositional Environments of the Kurnub Group (Early Cretaceous) in northern Jordan. Journal of African earth Sciences 29: 449-468.

Attah, L.E. and Oden, I. M. (2010). Physico-Chemical Properties and Industrial Potential of some Clay Deposits in Calabar Area, South Eastern Nigeria. Global Journal of Environmental Sciences 9: 39-49.

Bain, J.A. and Highly, D.E. (1978). Regional appraisal of clay resources challenge of the clay mineralogist. In: Mortland M. M. and farmer V. C. (Eds.), Proc. Int. Clay Conference. Elsevier. Amsterdam.

Bloodworth, A.J. Highley, D.E. Mitchell, G.J. (1993). Industrial Mineral laboratory manual: Kaoline. British Geological Survey. UK.

Ciullo, P. (1996). Industrial rock and their uses, Noyes publication, USA.

Correia, S.L., Curto, K.A. S., Hotza, D., Segadaes, A.M. (2005). Clays from southern Brazil: Physical, chemical and mineralogical characterization. Material Science Forum 498: 447-452.

Djomogue, P. and Njopwovo, D. (2013). ET-IR Spectroscopy Applied For Surface Clay Characterization. Journal of Surface Engineered Materials and Advanced Technology 3: 275-282.

Dominguez, E., Dondi, M., Etcheverry, R., Recio, C., Iglesias, C. (2016). Genesis and mining potential of kaolin deposits in Patagonia (Argentina). Applied Clay Science 131: 44-47.

Erdemoğlu, M., Birinci, M., Uysal, T. (2020). Thermal Behavior of Pyrophyllite Ore during Calcination for Thermal Activation for Aluminum Extraction by Acid Leaching. Clays and Clay Minerals 68(2): 89-99. https://doi.org/10.1007/s42860-019-00061-w

Ekosse, E. (2005). Fourier transform infrared Spectrophotometry and X-ray powder diffractometry as complementary techniques in characterizing clay size fraction of kaolin-ray. Diffraction Unit. Facility of Sciences, University of Botswana. Botswana.

Eletta, O.A., Aluko, F.I., Adekola, F.A. (2015). Bleaching of Nigerian kaolin by oxalic acid leaching. Journal of chemical technology and metallurgy 50: 623-630.

Eslinger, E. and Peaver, D. (1988). Clay minerals for petroleum geologist and engineers. Short course no. 22th Sep. Society for Sedimentary Geology, Tulsa, U.S.A.

Florunso, D.O., Olubambi, P., Borode, J.O. (2014). Characterization and qualitative analysis of some Nigerian clay deposits for refractory applications. IOSR Journal of Applied Chemistry 7: 40-47.

Gougazeh, M., and Buhl, C.H. (2010). Geochemical and mineralogical characterization of the jabal al-harad kaolin deposit, Southern Jordan for its possible utilization. Clay Minerals 45: 307-314.

Guggenheim, S. and Koster Van Gross, A.F. (2001). Baseline Studies of the Clay Minerals Society Source Clays: Thermal Analysis. Clay and Clay minerals 49 (5): 433-443.

Hou, X. and Jones, T. (2000). Inductively Coupled plasma/ Optical Emission Spectrometry Encyclopeida of Analytical Chemistry. John Wiley and Sons Ltd, Chichester.

Hutchison, C.S. (1974). Laboratory handbook of petrographic Techniques. John Wiley and sons, New-York.

Johnston, C. (2017). Infrared and Raman Spectroscopies of Clay Minerals, In: Bergaia, F. (ED.), Developments in Clay Science-8, Infrared Studies of Clay Mineral-Water Interactions, Elsevier, U.S.A. pp. 288-309.

Jovanovic, M. and Mujkanovic, A. (2013). Characterization, beneficiation and utilization of the clay from central Bosnia. 17th International research / expert conference "Trends in the development of machinery and associated technology", Istanbul, Turkey.

Kakali, G., Perraki, T., Tsivilis, S., Badogiannis, E. (2001). Thermal treatment of kaolin: the effect of mineralogy on the pozzolanic activity. Applied Clay Science 20: 73– 80.

Kashcheev, D. and Turlova O.V. (2010). Physical-chemical properties of ceramic mix using Nizhneuvel Skoe clay. Glass and Ceramics 67 (5): 173-175.

Kharbish, S., and Farhat, H.I. (2017). Mineralogy and physico-chemical properties of Wadi Badaa clays (Cairo-Suez district, Egypt): a prospective resource for the ceramics industry. Arabian Journal of Geosciences 10 (174): 3-10. https://doi.org/10.1007/s12517-017-2969-1.

Khoury, H.N. (2002). Clays and clay minerals in Jordan. Publications of the Deanship of Academic Research. University of Jordan. Amman- Jordan.

Khoury, H.N. (2006). Industrial rocks and minerals in Jordan. Publications of the Deanship of Academic Research. The University of Amman-Jordan.

Khoury, H.N. (2019). Review of clays and clay minerals in Jordan. Arabian Journal of Geosciences 12: 706. https://doi.org/10.1007/s12517-019-4882-2.

Khoury, H.N., Hodali, H., Hourani, M., Mubarak, Y., Faqir, N., Hanayneh, B., Esaifan, M. (2008). Mineral Polymerization of Some Industrial Rock and Minerals in Jordan. Publications of the Deanship of Academic Research. University of Jordan. Amman-Jordan.

Khoury, HN. and El-Sakka, W. (1986). Mineralogical and industrial characterization of the Batn El-Ghoul clay deposits, southern Jordan. Applied Clay Science 1(4): 321-331, 333, 335, 338, 341, 344, 347-351. https://doi.org/10.1016/0169-1317(86)90009-8.

Kloprogge, J.T. (2017). Raman and Infrared Spectroscopies of Intercalated Kaolinite Groups Minerals. In: Bergaia, F. (Ed.), Developments in Clay Science-8, Infrared Studies of Clay Mineral-Water Interactions, Elsevier, U.S.A. pp. 343-410.

Ligas, P. Uras, I. Dondi, M.M., Marsigli, M. (1997). Kaolnitic Materials from Romania (North- West Sardinia, Italy) and their Ceramic Properties. Applied Clay Sciences 12: 145-163.

Madejová, J., Gates, W.P., Petit, S. (2017). IR Spectra of Clay Minerals. In: Bergaia, F. (Ed.), Developments in Clay Science-8.

Infrared Studies of Clay Mineral-Water Interactions, Elsevier, U.S.A. pp. 107-149.

Mark, U. (2010). Characterization of Ibere and Oboro Clay Deposits in Abia State, Nigeria for Refractory Applications. International Journal of Natural and Applied Sciences 6 (3): 296-305.

Murray, H. (2007). Applied Clay mineralogy: Occurrences, Processing and Application of Kaolin's, Bentonies, Palygorskite-Sepiolite, and Common Clays. Elsevier, U.S.A.

Poppe, L.J. Paskevich, V.F. Hathaway, J.C. Blackwood, D.S. (2001). A laboratory Manual for X-Ray powder Diffraction. U.S. Geological Survey, U.S.A.

Preston, M. and Tatarzyn, J. (2013). Mineral Processing Optimizing Plants efficiency With Attrition Scrubbers. Yan-Tai Jin-Peng Mining Machinery Company. China.

Qtaitat, M.A. and Al-Trawneh, I.N. (2005). Characterization of kaolinite of the Baten ElGhoul region/south Jordan by infrared spectroscopy. Spectrochimica Acta Part A: Molecular and Biomolecular Spectroscopy 61(7): 1519-1523. https://doi.org/10.1016/j.saa.2004.11.008

Royal Jordanian Geographic Center, Jarash maps sheet (2003). 1:25.000, Amman, Jordan.

Sandgren, M.E. Berglind, B. Modigh, S. (2015). Basics in mineral processing handbook, Finland.

Sawariah, A. and Barjous, M. (1993). Geology of Suwaylih area. Map Sheet no.3154-II. Natural Resources Authority, Amman.

Vaculikova, L. Plevona, E. Vallova, S. Koutnik, I. (2011). Characterization and differentiation of Kaolinites from selected Czech deposits using Infrared spectroscopy and differential thermal analysis. Acta Geodynamica et Geomaterialia 8(1):59-67.

Welton, E. (2003). SEM Petrology Atlas. The American Association of Petroleum Geologists. Tulsa, Oklahoma, U.S.A.

William, D. and Carter, B. (2009). Transmission electron microscopy a textbook for materials sciences. 2nd Ed., Springer, U.S.A.

Yasin, S. and Ghannam, A. (2006). Kaolinite, National Resource Authority, Amman, Jordan.

JJEES

JJEES (2020) 11 (4) 282-290
ISSN 1995-6681

Jordan Journal of Earth and Environmental Sciences

Factors Affecting the Rate of Absorption of Sulfur Dioxide into Fly Ash Suspensions

Ahmad Al-Haj-Ali

University of Jordan, School of Engineering, Department of Chemical Engineering, Jordan.

Received 15 February 2020; Accepted 18 June 2020

Abstract

The absorption rate of sulfur dioxide into aqueous suspensions of lignite fly ash was experimentally investigated using lab-scale continuously stirred tank reactor. The effects of SO_2 inlet concentration, suspension concentration, and temperature were evaluated and reported. Concurrent gas absorption and alkalinity leaching from ash particles produced 1.5 to 4.0 times higher concentrations of Ca and Mg alkalinity and thus much higher SO_2 removal capacity compared to consecutive leaching and gas absorption due to the role of pH and chemical changes associated with it. Data on SO_2 solubility in ash suspension and pH as well as stoichiometric relations among chemical reactions are used to correlate absorption rate to alkaline metals leaching rate. Initial absorption was found to be a function of inlet SO_2 concentration and independent of suspension concentration due to quick surface leaching. In the later stages, the absorption rate becomes a strong function of the leaching rate connected to alkalinity release from the interior surfaces of ash particles.

Keywords: Flue gas, desulfurization, sulfur dioxide, fly ash, absorption, leaching, calcium, magnesium, kinetics

1. Introduction

Fly ash is a problematic fine powder waste captured by air-pollution control equipment after fossil fuel combustion processes in power plants and other industrial activities. Due to its physical and chemical properties as well as massive production rate, this material threatens human health and all elements of the environment making fly ash management with safe disposal a big challenge (Baig and Yousaf, 2017; Blissett and Rowson, 2012). Several hundred million tons of fly ash are produced annually from power plants worldwide, with less than 50% being utilized and reused, mostly in civil engineering (construction) and agricultural (ameliorating soil conditions) applications (Yao et al., 2015). Fly ash particles captured by air pollution collection devices are transported via wet sluicing to lagoons, dry handling to landfill or reuse destination (Ritter, 2016; Ahmaruzzaman, 2010).

However, fly ash has the potential to be a resource material rather than being solely a hazardous waste. It can be used as raw material for geopolymers having adsorption and ion exchange properties to remove many air and water and wastewater pollutants (Ge et al., 2018; Blissett and Rowson, 2012; Swanepoel and Strydom, 2002). One practical and sustainable option for the power industry is the recycling and utilization of fly ash as scrubbing medium in both wet and dry flue-gas desulfurization (FGD) systems. Fly ash is known to provide alkaline species upon leaching in water which are capable of neutralizing acidic stack gases, particularly, SO_2, and the material has attracted researchers over the past decades (Li et al., 2008). This capability has been investigated, particularly by using fly ash as an inexpensive supplement to lime or seawater in conventional wet scrubbing systems, or as the sole absorbent for FGD of low-sulfur power plants (International Energy Agency, 2020; Back et al., 2019; Liao et al., 2012). More research is needed for a better understanding of the kinetics of sulfur dioxide scrubbing in fly ash media in order to design and optimize the scrubbing process system. The main objective of this study is to evaluate the rate of SO_2 absorption into fly ash suspensions at key operating conditions in a three-phase stirred tank slurry reactor. A theoretical chemical and mass transfer analyses are used to arrive at a simple correlation for the rates of simultaneous alkalinity leaching and gas absorption processes.

2. Methodology

Fly ash from lignite coal is used as a source of alkalinity. The chemical composition for the ash used in this study is given in Table 1 (Al-Haj Ali, 1989). A stirred vessel was used to carry out both leaching and gas absorption experiments. The reactor consisted of a four-liter vessel of Pyrex glass, 14 cm in diameter and 34 cm in height equipped with a four-bladed turbine impeller which is 6.4 cm in diameter and 1.27 cm in width. The impeller was fitted by a 1.27 cm motor shaft which, in turn, was fitted by a mechanical seal and bearings to the reactor cover. The cover was provided with adequate ports for feeding the solid particles, temperature measurement, liquid sampling and gas exit. The cover, shaft, turbine, sparger, sampling pipe and fittings were all stainless steel. A schematic diagram illustrating the experimental setup is shown in Figure 1

* Corresponding author e-mail: ahmad.ay55@gmail.com

Table 1. Chemical composition (weight percent) of fly ash size cuts used in the study

	SiO_2	Al_2O_3	Fe_2O_3	CaO	MgO	Na_2O	K_2O	TiO_2	MnO_2	P_2O_5	LOI*
53-63µm	48.0	22.2	5.83	12.7	4.31	2.00	1.22	0.77	0.01	0.26	0.82
63-75µm	47.3	22.0	6.49	12.9	4.44	2.01	1.22	0.78	0.02	0.26	0.83

**Loss on Ignition*

For absorption experiments, SO_2 was diluted in nitrogen to the desired inlet gas concentration by setting the appropriate flow rates of SO_2 while maintaining the flow rate of nitrogen constant. Gases were fed to the reactor by means of a 0.5 cm diameter stainless steel ring sparger installed through the reactor cover. Before that, they passed through a long tubing to allow for better mixing. The sparger ring was provided with sixteen perforations, 0.05 cm diameter each. Each gas was delivered at 1.36 atm. For leaching experiments, only nitrogen was allowed to pass through the reactor. SO_2 and N_2 flow meters were calibrated by the soap-bubble method and wet-test meter, respectively. Effluent gases from the reactor were passed through a twenty-liter container with 20% sodium hydroxide to remove unreacted SO_2, followed by a vent to allow non-absorbed gases to pass to the fume hood.

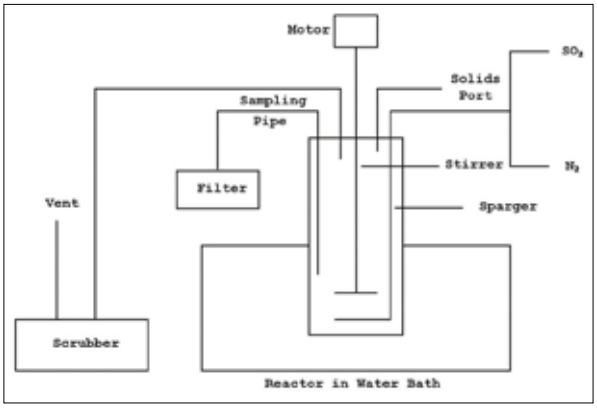

Figure 1. Schematic diagram illustrating the experimental setup.

A variable speed stirrer capable of providing up to 2000 rpm of impeller speed was used. The speed was adjusted and monitored using a strobe light. All the reactor experiments were carried out at a constant temperature. Isothermal conditions were maintained by immersing the reactor in a constant-volume water bath. For the leaching experiments, the pH of the water was adjusted to the desired level prior to the addition of the solids. For the absorption experiments, the pH of the water was not adjusted; rather it remained in the range of 5.4-5.6 due to the acidic nature of aqueous species present. The suspension pH was not controlled in order to quantify the changes caused by ash leaching, gas absorption or both. Initial pH was adjusted to 2.0 or 6.0 for leaching-only experiments (without SO_2 absorption) using 2.0 N nitric acid.

Ash suspensions were prepared by the addition of an accurately weighted amount of ash powder to a volume of 2 L of distilled water in the reactor at the desired conditions of the experiment (stirring, temperature and initial pH). Solids were fed by a funnel through a designated port in the reactor cover and it was completed within ten to twenty seconds. Samples were withdrawn from the reactor at the desired times (3, 5, 10, 15, 30, 45, 60 min … etc.) through a sampling pipe into a vacuum filtration system. About 5-10 cm^3 of filtrate were collected through 0.45µm pore-size membranes into a screw-capped test tube. Part of the filtrate was used to measure the leachate pH and the rest was used for the determination of dissolved metal concentrations.

Three types of analyses were performed on liquid samples, namely, determination of dissolved Ca or Mg concentrations released during leaching, both in the absence and the presence of gas absorption using a Perkin Elmer atomic absorption spectrophotometer; determination of concentrations of absorbed sulfur S(IV) species was done using iodometric titration, and measurement of pH was conducted using a digital pH meter. The chemical composition of ash particles (expressed as weight percent of CaO and MgO among other components) are conducted using X-ray spectrophotometry. The composition of the gas feed to the reactor was analyzed by a Hewlett Packard gas chromatography Model 5890A to verify the percentage SO_2 in the N_2/SO_2 mixture set by adjusting the individual gas flow rates (Al-Haj Ali, 1989).

3. Results and Discussion

In the absence of SO_2 gas, leaching experiments in the reactor at specified conditions produced the results shown in Table 2. The alkaline species leached out in significant amounts from fly ash particles are Ca and Mg cations, with Na and K cations being undetectable. Lower pH is favorable to dissolve more Ca and Mg due to the effect of acid-base interaction, which is also confirmed in other reported studies (Gao et al., 2011; Gitari et al., 2009). Dissolved calcium concentrations produced are quite higher than those of magnesium, an observation which can be explained by the fact that calcium hydroxide is far more soluble in water than magnesium hydroxide. The solubility product (K_{sp}) of $Ca(OH)_2$ at 25ºC is 5.02 x10^{-6} mol/L compared to 5.61 x10^{-12} mol/L for $Mg(OH)_2$ (Lide, 2003). Therefore, these two metal ions are responsible for the alkaline character of the ash suspensions.

Table 2. Concentrations of dissolved alkaline metals after 60 minutes of leaching in reactor

Cation	Concentration (mg/L)	
	pH 2.0	pH 6.0
Ca^{2+}	164	55
Mg^{2+}	35	1
Na^{+}	nil	Nil
K^{+}	nil	Nil

Results of concentration (for dissolved sulfur or Ca and/ or Mg) versus time obtained from experiments on SO_2 absorption into pure water as well as leachate (solid-free) and suspensions of fly ash will be presented and discussed to illustrate the effect of selected operating conditions on gas absorption rate. A theoretical analysis will also be presented and applied to the experimental data. The total concentration of S(IV), including both concentrations of unhydrolyzed $SO_{2(aq)}$ and bisulphite ions (HSO_3^-), was determined experimentally by the iodometric titration. Since the reactor was purged with nitrogen before the SO_2 flow started and there was no oxygen in the feed gas, no oxidation took place in the reactor and, therefore, no sulphate (SO_4^{2-}) was formed. The ash powder was added three minutes before SO_2 was sparged in and the pH increased to around 10. All experiments showed that as soon as the gas was introduced into the liquid phase, the suspension pH dropped sharply due to the rapid absorption of SO_2, and then it stabilized at a value in the range of 5.4-5.6, which is considered to be initial pH for absorption study. The pH profiles of the three-phase system during simultaneous leaching and gas absorption under selected process parameters are reported.

3.1 Effect of Temperature

The effect of suspension temperature on the total concentration of aqueous sulfur, S(IV), obtained by the absorption of SO_2 into lignite ash suspensions is shown in Figure 2. The experiments were carried out at 20, 40, and 55°C while keeping the suspension concentration at 10 g/L and the SO_2 inlet concentration at 0.5 mol %. S(IV) values obtained at 55°C are slightly less than those obtained at lower temperatures, which can be attributed to lower gas solubility at the gas-liquid interface. Other studies also indicated that the negative effect of temperature on SO_2 solubility is slightly higher than its positive effect on diffusivity (Ma et al., 2019).

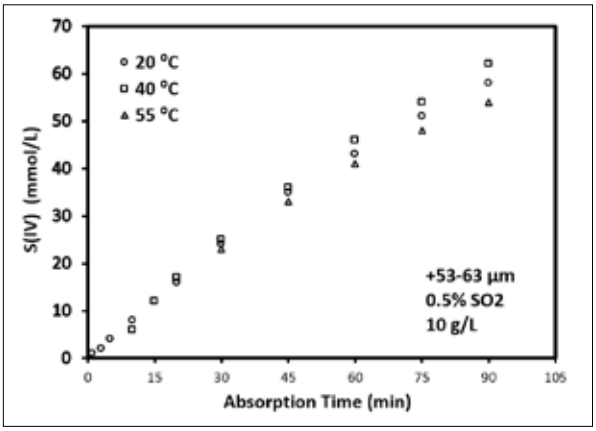

Figure 2. Effect of suspension temperature on absorbed S(IV) concentration.

Temperature is expected to have a dual effect on the overall process of SO_2 removal by suspensions of sparingly soluble solids. The dissolution of alkaline compounds in the solid particles gets a small enhancement as temperature is increased due to the increase in their solubility and ionic diffusivities, while the solubility of the gas is decreased by about 50% when the temperature is increased from 20°C to 40°C. The outcome of these two opposing effects will depend on the characteristics of the medium and the experimental conditions including the temperature level. Due to the insignificant influence of temperature on the absorption rate, the process can be assumed to be controlled by mass transfer rather than chemical reaction kinetics. Further experiments were conducted at 40°C.

3.2 Absorption in Water, Clear Solution, and Suspension

The results of absorption experiments using the three different media are shown in Figure 3. In one experiment, inlet concentration of SO_2 of 0.5 mol % was allowed to equilibrate with distilled water in the stirred tank reactor at 40°C. The solution is saturated with dissolved unhydrolyzed SO_2 and bisulphite ions [total S(IV)] in 20-30 min levelling off at 11 mmol/L. Another absorption experiment was carried out in which the absorbing medium is a clear solution of ash leachate. A leaching-only experiment was conducted in the reactor using 10 g ash/L at initial pH of 5.5 and 40°C for sixty minutes. The suspension was filtered, ash particles were discarded, and a filtrate was added to the reactor as a medium for SO_2 absorption. The S(IV) concentration leveled off at 45-60 minutes at 21 mmol/L, twice as much as S(IV) in water.

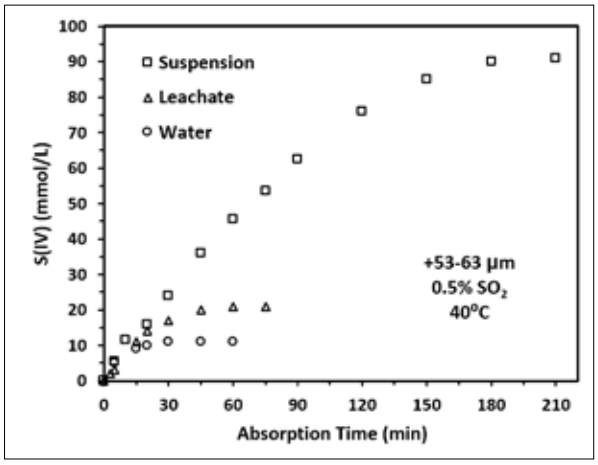

Figure 3. Comparing SO2 absorption into water, leachate solution and suspension.

In a third experiment, concurrent leaching from suspension (at 10 g/L) and gas absorption are allowed to proceed for the same conditions above. It can be seen that during the first 10-15 minutes of contact, the rate of absorption was the same regardless of the type of absorbing medium as indicated by the initial slopes. After sixty minutes, the solution of leachate solution absorbed twice as much SO_2 as pure water at the given conditions. When ash suspension was allowed to release the alkalinity simultaneously with absorption, the amount of the gas absorbed after sixty minutes (and later times) increased to more than four times as much as that of the solid-free leachate solution. This large difference in the absorption capabilities of the suspension and leachate reflects a corresponding large difference in the amount of available soluble Ca and Mg. Since this alkalinity is produced by the continuous dissolution of the alkaline metals in the ash, the concurrent use of a suspension rather than a leachate solution is necessary to enhance leachable alkalinity and maximize the scrubbing ability of the ash. In order to achieve this, the conditions that favor the dissolution of Ca and Mg, in particular, high suspension concentration and a lower pH, should be maintained.

3.3 Effect of Suspension Concentration

The effect of ash suspension concentration or slurry density on the change of S(IV) concentration with time is shown in Figure 4. The inlet SO_2 concentration was kept constant at 0.5 mol %. In the first 20-30 minutes, gas absorption capability of the suspension is quite independent of the amount of solids present due to the readily soluble and sufficient Ca and Mg released from external particle surfaces. After this initial period, S(IV) concentration increased gradually with the increasing of suspension concentration (5, 10 and 20 g/L) to level-off at different times depending on the quantity of alkalinity provided by each suspension concentration. The same trend is reported by Liao et al. (2012) who experimentally studied the SO_2 removal in coal fly ash slurries.

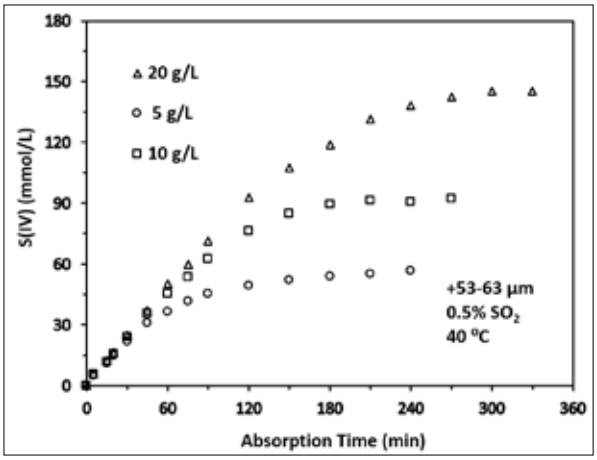

Figure 4. Effect of suspension concentration on the amounts of S(IV) absorbed.

3.4 Comparing Leached Metal Cations with and without Absorption

The concentrations of Ca and Mg species released from ash during SO_2 absorption at different suspension concentrations are shown in Figure 5 (a,b). To further illustrate the significant differences between gas absorption capabilities of concurrent absorption/ leaching and leaching prior to absorption, the concentrations of Ca or Mg released from ash in the absence of SO_2 are plotted in Figure 6 (a,b). A comparison of data in these two Figures indicate that the concentrations of metals released during absorption increased by a factor of 1.5- 2.0 and 1.5- 4.0 times for Ca and Mg, respectively compared to those in the absence of SO_2. This comparison is based on values obtained at contact times at 60 and 180 minutes, when the curves started to level off. Moreover, dissolution of Ca and Mg in the presence of absorbed SO_2 continued for much longer times before the concentrations reached a constant value. The large increase in dissolved Ca and Mg concentrations can be explained by fast chemical reactions between acidic species produced by the hydrolysis of SO_2 (bisulphite ions) with alkaline metal ions (Ca^{2+} and Mg^{2+}). These reactions are given and discussed later along with the effect of pH on the concurrent leaching and absorption processes.

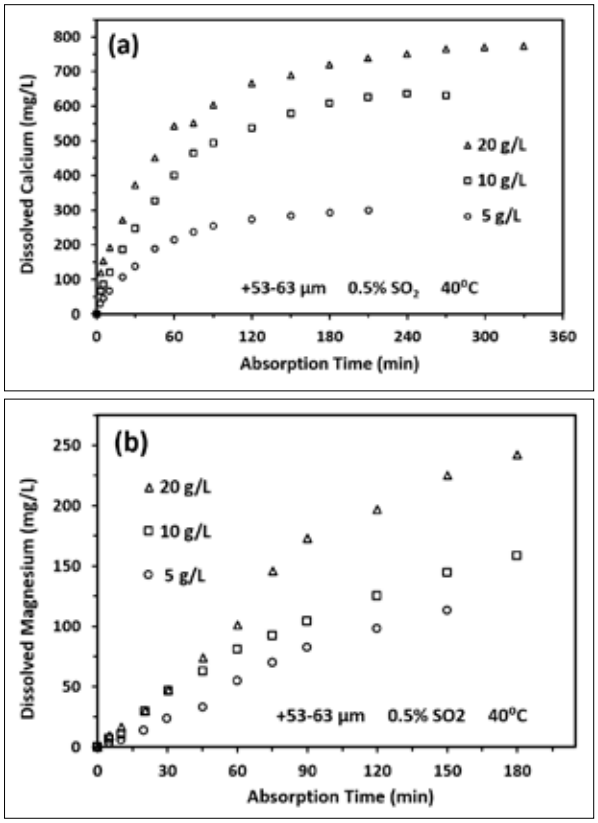

Figure 5. (a, b). Concentrations of Ca and Mg released from ash suspensions during SO_2 absorption.

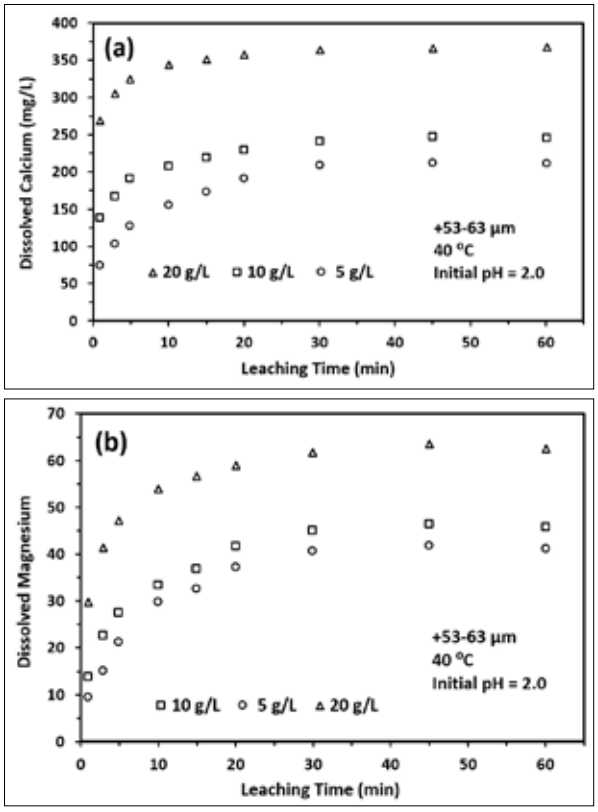

Figure 6. (a, b). Concentrations of Ca and Mg released from ash suspensions prior to SO_2 absorption.

3.5 Effect of SO_2 Inlet Concentration

Results of S (IV) concentrations versus absorption time at three different SO_2 inlet concentrations (expressed as mol percent SO_2 in N_2/SO_2 mixture) and constant suspension concentration (10 g/L) are plotted in Figure 7. At any given time, S (IV) increased with increasing the SO_2 gas inlet concentration since more SO_2 will dissolve in solution accordingly. Similar results are reported in the literature including those of Ma et al. (2019) who studied SO_2 scrubbing by seawater and Liao et al. (2012) who studied the SO_2 removal in fly ash slurries at inlet gas concentrations 1000-10000 mg SO_2/m^3.

A reactor model based on mass balance is useful in expressing initial absorption rates, at which most of the gas is removed in the early stages of the process. Based on the assumption of a well-mixed gas phase, a mass balance for SO_2 over the entire gas volume in the reactor, V_g, at any time, t, gives:

$$Q\,C_{gf} - Q\,C_g - r\,V_L = V_g\,(dC_g/dt) \quad (1)$$

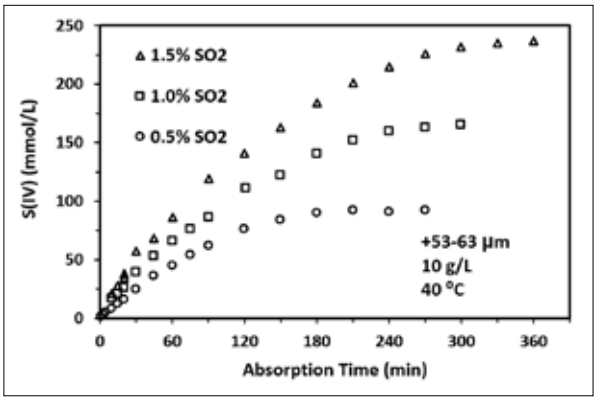

Figure 7 Effect of SO_2 inlet concentration on the amounts of S(IV) absorbed.

The accumulation term (dC_g/dt) can be neglected because of the small values of both the gas volume, V_g, and the rate of change in the gas concentration with time. The gas volume (or holdup) in the reactor was estimated to be about 100 cm^3 which is only 5% of the liquid volume (2 L). Also, the variation of exit gas-phase concentration, C_g, with time is not high especially at the later stages of absorption, thus:

$$C_{gf} - C_g = r\,(V_L/Q) = V_L/Q\,(dC_T/dt) \quad (2)$$

$$C_g = C_{gf} - (V_L/Q)\,(dC_T/dt) \quad (3)$$

When the percentage of SO_2 removal [calculated as $\{(C_{gf} - C_g)/ C_{gf}\}$ x100%] is close to 100 %, the exit concentration of SO_2 is very small compared to the inlet concentration; therefore, C_g can be neglected. In general, SO_2 removals efficiencies close to 100% were obtained during the initial stage of absorption when the liquid phase contained abundant alkalinity. Assuming that the gas is well-mixed, the absorption rate is given by:

$$dC_T/dt = Q\,(C_{gf}/V_L) \quad (4)$$

The equation above suggests that if the volume of the liquid and the volumetric flow rate are fixed, initial absorption rate depends only on the concentration of SO_2 in the feed. This is demonstrated by the slopes of S(IV) concentration vs. time lines shown in Figure 8 (a), which are calculated by linear regression (equations and correlation coefficients given on the Figure), then plotted against the inlet SO_2 concentrations as shown in Figure 8 (b). The slope of the resulting line is 3.0 min^{-1} (also from linear regression), which is close to the ratio of Q/V_L= 6.5 $L.min^{-1}$/ (2L), or 3.25 min^{-1}. Furthermore, equation (4) suggests that as long as the SO_2 removal is close to 100%, the rate of absorption does not depend on the absorption medium. This conclusion is essentially confirmed by the values of the initial rates obtained from a number of representative experiments, which are presented in Table 3. It is important to note that these initial rates were obtained at high levels of solution pH which prevailed at the beginning of the experiments.

Table 3. Initial rates of SO_2 absorption for different media and conditions

SO_2 Inlet Concentration	Medium*	Initial Rate (mmol/L/min)
0.5 mol % (0.005 atm = 0.195 mmol/L)**	Pure water	0.76
0.5 mol %	Clear leachate solution	0.81
0.5 mol %	Suspension at 10 g/L	0.79
0.5 mol %	Suspension at 20 g/L	0.80
1.0 mol % (0.010 atm = 0.390 mmol/L)	Suspension at 10 g/L	1.52
1.5 mol % (0.015 atm = 0.585 mmol/L)	Suspension at 10 g/L	2.00

Other conditions were fixed* * Using ideal gas law*

3.6 The Role of pH

The values of pH during SO_2 absorption into ash suspensions are given in Table 4 at different ash suspension concentrations and SO_2 inlet concentrations. It can be seen that during the initial stage of absorption, there was a sharp drop in the pH which lasted for few minutes, after which the suspension pH stabilized at a value in the acidic range for the rest of the experiment. This relatively constant pH level is the resultant of the effects of the two concurrent processes of gas absorption and leaching of alkaline metals. The hydrolysis of absorbed (aqueous) SO_2 to bisulphite ions results in producing constant supply of hydrogen ions which will drive dissolution of alkaline metal oxides through reaction with hydroxide ions produced by the alkalinity leaching process. Maintaining a low pH throughout the absorption process is important to enhance and further the dissolution of alkaline species from the ash particles (chemical equations given below). The fact that the overall pH level is low eliminates any possibility of absorbing a fraction of SO_2 which is present in the actual power plant flue gas in 50-100 times as much as SO_2. Moreover, carbon dioxide may be absorbed in the scrubbing solution when the pH is higher than 7.0. In industrial scale scrubbing processes and in the presence of oxygen in the flue gas, lower pH will speed up the oxidation from sulphite to sulphate (Poullikkas, 2015; National Lime Association, 2003).

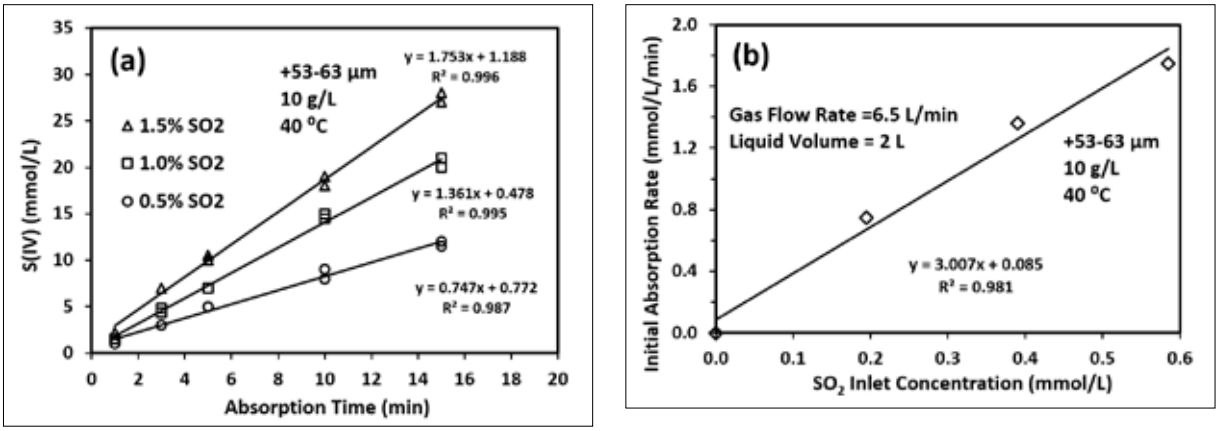

Figure 8. (a, b). Initial SO_2 absorption rates as a function of gas inlet concentration.

Table 4. Suspension pH during absorption into ash suspensions at different conditions

Time (min)	Suspension concentration (g/L) (SO_2 inlet concentration = 0.5%)			SO_2 inlet concentration (Suspension concentration = 10 g/L)		
	5	10	20	0.5%	1.0%	1.5%
0	9.6	9.9	10.3	9.9	9.75	10.1
1	7.0	7.1	7.35	7.1	6.6	6.8
3	3.7	3.7	3.8	3.7	2.9	2.7
5	3.55	3.5	3.7	3.5	2.8	2.6
10	3.4	3.35	3.55	3.35	--	2.5
15	--	3.25	--	3.25	2.75	--
20	3.2	3.35	3.4	3.35	--	2.5
30	3.1	3.3	3.4	3.3	2.6	2.45
45	3.0	3.3	3.3	3.3	2.6	2.4
60	3.0	3.25	3.35	3.25	2.65	2.45
75	2.95	3.25	3.35	3.25	2.5	2.5
90	3.05	3.2	3.4	3.2	2.5	2.5

3.7 Solution Chemistry

The results discussed earlier have demonstrated that after the initial drop from highly alkaline to acidic levels, the pH was never greater than 4.5 in any of the absorption experiments performed in this study. In this pH range, the predominance diagram of sulfur species (Beyad et al., 2014) shows that the only important species in the liquid phase are the aqueous molecular SO_2 and bisulphite ion. The sulphite ion does not exist in the solution during this period due to lower pH. Based on this, the following equations represent the reactions taking place in the mixed three-phase system

(Slack et al., 1972):

Gas Absorption by water:

$$SO_{2\,(g)} \leftrightarrow SO_{2\,(aq)} \quad (5)$$

Absorbed Gas Hydrolysis:

$$SO_{2\,(aq)} + H_2O \leftrightarrow HSO_3^- + H^+ \quad (6)$$

Metal Dissolution:

$$CaO_{\,(s)} + H_2O \rightarrow Ca(OH)_{2\,(aq)} \rightarrow Ca^{2+} + 2OH^- \quad (7)$$

$$MgO_{\,(s)} + H_2O \rightarrow Mg(OH)_{2\,(aq)} \rightarrow Mg^{2+} + 2OH^- \quad (8)$$

$$1/2z\ M_yO_z + 1/2\ H_2O \leftrightarrow y/2z\ M^{2+} + OH^- \quad (9)$$

Metal-Sulfur Reactions:

$$Ca^{2+} + HSO_3^- \rightarrow CaSO_3 + H^+ \quad (10)$$

$$Mg^{2+} + HSO_3^- \rightarrow MgSO_3 + H^+ \quad (11)$$

Acid-Base Neutralization:

$$OH^- + H^+ \leftrightarrow H_2O \quad (12)$$

In the chemical model above, it is assumed that alkaline ions other than Ca and Mg are negligible (Table 2). According to Uchida et al. (1975), the reaction between absorbed gas (SO_2) and dissolved solid species [$Ca(OH)_2$ or $Mg(OH)_2$], is fast and thus the overall absorption process rate is controlled by the slower step of diffusional mass transfer. The fast reactions among aqueous species (Equations 10 and 11) do enhance the solid leaching rate and accordingly the gas absorption rate. The total concentration of sulfur compounds in solution [S(IV)] at constant pH is the sum of the concentrations of molecular $SO_{2(aq)}$ and the bisulphite ions, HSO_3^-:

$$C_T = C_A + C_B \quad (13)$$

The solubility of SO_2 gas in a solution (Equation 5) can be expressed in terms of Henry's law constant, H, defined as C_A/p_{SO2}. Henry's law constant for SO_2 in water can be

calculated from the following equation at 40°C (Rabe and Harris, 1963):

$$H = \exp [(2851.1/T) - 9.3795] \quad (14)$$

For a pressure of 1 atm, the solubility is 763 mmol/L and for 0.005 atm it is only 3.8 mmol/L. Therefore, the main component of S(IV) is bisulfite ions, that is, $C_A << C_B$.

3.8 Stoichiometric Relationships

The constant pH after 10-15 minutes of absorption implies that the hydrogen ion concentration is constant. To satisfy the dissociation equilibrium constant of water (Equation 12), the concentration of the hydroxide ion should also be constant. Therefore, the rate of the generation of hydroxide ions by the dissolution of metal compounds from ash (Equation 9) is equal to the rate of the generation of hydrogen ions by the hydrolysis of the dissolved SO_2 (Equation 6). The latter rate is also equal to the rate of generation of bisulphite ions from the same reaction:

$$d[H^+]/dt = d[OH^-]/dt \quad (15)$$

$$d[H^+]/dt = d[HSO_3^-]/dt = dC_B/dt \quad (16)$$

$$d[OH^-]/dt = (y/2z)\, d[M^{2+}]/dt = dC_m/dt \quad (17)$$

From the abovementioned stoichiometric relations, the following relationship equation between the rates of metal leaching and bisulphite ions production is obtained:

$$dC_m/dt = (y/2z)\, dC_B/dt \quad (18)$$

Stoichiometric relations also indicate that the rate of SO_2 absorption from the gas phase by the liquid medium should be equal to the rate of increase in the total concentration of S(IV) in solution, C_T, and it is given by:

$$dC_T/dt = dC_A/dt + dC_B/dt \quad (19)$$

Substituting for the bisulphite term from equation (18):

$$dC_T/dt = dC_A/dt + (2z/y)\, dC_m/dt \quad (20)$$

Which can also be represented by:

$$R_{Absorption} = R_A + (2z/y)\, R_{Leaching} \quad (21)$$

R_A denotes the rate of transfer of molecular SO_2 from gas-liquid interface to bulk liquid (mmol $SO_{2(aq)}$/L/min). Both $R_{Absorption}$ and $R_{Leaching}$ were calculated based on the experimental data of S(IV) vs. absorption time [Figure 4] as well as dissolved calcium plus magnesium (leached out during SO_2 absorption) vs. leaching time [Figure 5 (a, b)].

The rates calculated using data obtained at different suspension concentrations of 5, 10, and 20 g/L are plotted according to the model expressed in equation 21 and the results obtained from linear regression are given in Table 5. The linear plots are shown in Figure 9, which indicates that gas absorption rates are strongly dependent on alkalinity leaching rates. In the special case of z/y = 1 (Equations 7-9) applicable to the leaching of calcium and magnesium only, the slope is 2, which lies in the above range of slopes. Other values for the slope may be obtained depending on the complexity of the mixture where other sources of alkalinity or acidity are involved. Figure 9 also indicates that the rate of transfer of molecular SO_2 from gas-liquid interface to bulk liquid, R_A, increased with the increasing of the suspension concentration. This can be explained by the fact that at higher alkalinity, hydrolysis reaction (Equation 6) is shifted to bisulphite formation and more $SO_{2(aq)}$ is needed to maintain the equilibrium. Overall, such a simple stoichiometric model developed in this work can be useful in evaluating the interdependency of gas absorption and alkalinity leaching rates on each other in ash-based scrubbing media.

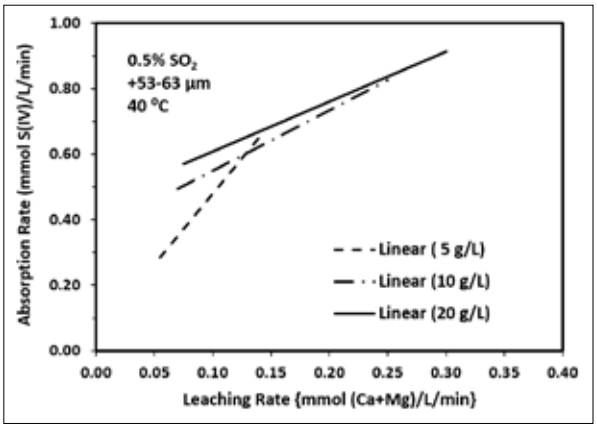

Figure 9. Correlation between SO_2 gas absorption and alkalinity leaching rates.

Table 5. Linear regression analysis of absorption- leaching rates correlations

Condition	Slope (2z/y)	Intercept (R_A)	Correlation Coefficient (R^2)
5 g/L	4.968	0.011	0.990
10 g/L	1.986	0.345	0.987
20 g/L	1.404	0.478	0.967

5. Conclusions

Several conclusions can be deduced from this study. Leaching of calcium and magnesium from ash particles constitute the effective soluble alkalinity for SO_2 absorption through neutralization reaction. Leaching rate depends on factors in the solid, liquid, and gas phases that determine the extent of Ca and Mg dissolution and hence subsequent gas absorption. In the initial stage of absorption (10-15 min), absorption rate is independent of the aqueous medium and function only of inlet gas concentration. The use of a solid/liquid suspension rather than a leachate or extract solution of ash is necessary to maximize the amount of alkalinity for higher SO_2 removal. Simultaneous alkalinity dissolution and gas absorption result in a constant pH that is maintained over most of the contact time between the three phases, and the value of which depends on the conditions prevailing in the reactor. The concentrations of total aqueous sulfur species, or S(IV) increased significantly with increasing the inlet concentration of SO_2 and suspension concentration not affected by suspension temperature or particle size within the tested period of contact time of ninety minutes. The overall conclusion is that fly ash-water suspensions are an attractive and cost-effective medium for SO_2 removal from low-sulfur fossil fuel flue gas.

Acknowledgements

This work was financially supported by the University of Jordan. The contribution of Dr. D. Berk is highly appreciated.

Nomenclature

C_{gf}: Feed concentration of gaseous SO_2, mmol/L of gas mixture,

C_g: Exit concentration of gaseous SO_2, mmol/L of gas mixture,

C_m: Concentration of metal ions ($Ca^{2+}$and Mg^{2+}) from dissolution of ash alkalinity, mmol/L,

C_A: Concentration of aqueous SO_2, mmol/L,

C_B: Concentration of bisulphite ion (HSO_3^-), mmol/L,

C_T: Concentration of total dissolved sulfur (IV), both $SO_{2\ (aq)}$ and HSO_3^-, in the bulk liquid, mmol/L,

K_{sp}: Solubility product, mol/L

p_{SO2}: partial pressure of SO_2 in the gas feed to the reactor, atm,

Q_g: Gas volumetric flow rate to the reactor, L/min,

R_A: Rate of transfer of molecular SO_2 from gas-liquid interface to bulk liquid, mmol $SO_{2(aq)}$/L/min,

V_L: Volume of liquid phase in the reactor, L.

References

Ahmaruzzaman, M. (2010). A review on the utilization of fly ash. Progress in Energy and Combustion Science 36: 327-363.

Al-Haj Ali, A. (1989). Characterization of the alkaline metal dissolution and sulfur dioxide absorption of fly ash slurries, Ph.D. Thesis, McGill University, Montreal, Canada.

Al-Harahsheh, A.M., Shawabkeh, R.A., Al-Harahsheh, M.S. Batiha, M.M. (2011). Removal of sulfur dioxide by a slurry of Jordanian oil shale ash. Energy Sources, Part A: Recovery Utilization, and Environmental Effects 34 (1): 90-98.

Back, S.K., Mojammal, A.H., Jo, H.H., Kim, J.H., Jeong, M.J., Seo, Y.C., Joung, H.T., Kim, S.H. (2019). Increasing seawater alkalinity using fly ash to restore the pH and the effect of temperature on seawater flue gas desulfurization. Journal of Material Cycles and Waste Management 21 (4): 962-973.

Baig, K.S. and Yousaf, M. (2017). Coal fired power plants: Emission problems and controlling techniques. Journal of Earth Science and Climatic Change 8 (7): 404.

Beyad, Y., Burns, R., Puxty, G., Maeder, M. (2014). A speciation study of sulfur (IV) in queous solution. Dalton Transaction 43 (5): 2147-2152.

Blissett, R.S. and N.A. Rowson. (2012). A review of the multi-component utilization of coal fly ash. Fuel 97: 1-23.

Lide, D.R. (Ed.). (2003). Solubility constants for compounds at 25°C. In "CRC Handbook of Chemistry and Physics", 84th Edition, National Institute of Standards and Technology, CRC Press, Boca Raton, USA.

Gao, R., Pan, W., Zhang, X., Xu, H., Ren, J. (2011). Dissolution rate of magnesium hydrate for wet flue gas desulfurization. Fuel 90 (1): 7-10.

Ge, J.C., Yoon, S.K., Choi, N.J. (2018). Application of fly ash as an adsorbent for removal of air and water pollutants. Applied Sciences 8 (7): 1116-1140.

Gitari, W., Fatoba, O., Petrik, L., Vadapalli, V. (2009). Leaching characteristics of selected South African fly ashes: Effect of pH on the release of major and trace species. Journal of Environmental Science and Health- Part A 44 (2): 206-220.

International Energy Agency, https://www.iea-coal.org/wet-scrubbers-SO2-control, visited on 31/05/2020.

Li., L., Fan, M., Brown, R.C., Kozeil, J.A., van Leeuwen, J. (2008). Reduction of SO2 in flue gas and applications of fly ash: A review. Power Plant Chemistry 10 (5): 291-301.

Liao, Y., Zhai, M., Li, F., Shi, W., Zhang, Y., Dong, P. Experimental study on desulfurization of fly ash slurry. Applied Mechanics and Materials 148-149: 487-490.

Ma, Y., Xu, L., Zhou, J., Yang, K., Li, G. (2019). Experimental investigation of seawater scrubbing of SO2 in turbulent contact absorbers and spray towers. Environment Protection Engineering 45 (3): 39-53.

National Lime Association (2003). Wet flue gas desulfurization technology evaluation, Report of Project No. 11311-000, NLA, Chicago, IL, USA, pp. 50.

Poullikkas, A. (2015). Review of design, operating, and financial considerations in flue Gas desulfurization systems. Energy Technology and Policy 2 (1): 92-103.

Rabe, A. E. and Harris, J. F. (1963). Vapour liquid equilibrium data for the binary system, sulfur dioxide and water. Journal of Chemical Engineering Data 8 (3): 333-336.

Ritter, S.K. (2016). A new life for coal ash. Chemical and Engineering News 94 (7): 10-14.

Slack, A.V., Falkenberry, H.L., Harrington, R.E. (1972). Sulfur oxide removal from waste gases. Journal of the Air Pollution Control Association 22 (3): 159-166.

Swanepoel, J. and Strydom, C. (2002). Utilization of fly ash in a geopolymeric material. Applied Geochemistry 17: 1143-1148.

Uchida, S., Koide, K., Shindo, M. (1975). Gas absorption with fast reaction into a slurry containing fine particles. Chemical Engineering Science 30: 644-646.

Yao, Z.T., Ji, X.S., Sarker, P.K., Tang, J.H., Ge, L.Q., Xia, M.S., Xi, Y.Q. (2015). A comprehensive review on the applications of coal fly ash. Earth-Science Reviews 141: 105-121.

JJEES

JJEES (2020) 11 (4) 290-301
ISSN 1995-6681

Jordan Journal of Earth and Environmental Sciences

Geological Mapping and Gemstones prospecting in Deformed Precambrian Rocks, East of Okemesi Fold Belt, Southwestern Nigeria

Olusiji Samuel Ayodele* and Isaac Ominyi Ajigo

Department of Applied Geology, School of Earth and Mineral Sciences, The Federal University of Technology P.M.B 704 Akure, Nigeria.

Received 21 March 2020; Accepted 1 July 2020

Abstract

The study area covered Ikogosi, Igbara odo, Ipole, Erijiyan and Araromi Ekiti respectively which are underlain by rocks that have undergone multiple episodes of tectonic deformation and formation of other deep-seated structures such as fractures, joints, veins, and foliations with steep-angle dips which are manifestations of the pervasive Pan African orogeny. The method adopted for this research includes field examination of the rocks, systematic sampling of the different rock units at a density of 100m-200m and petrographic studies of selected rocks samples using Binocular Polarizing Microscope with Topcam Digital Camera (3.1MP) and attached Computer software for taking snapshots of the rock slides for mineral indentification. Geological units of the area consist of migmatites, granites, granite-gneiss, quartzites (massive and schistose types) as well as pegmatites occurring as veins and dykes with varying lengths and sizes. The cross-sectional map of the area confirmed folding episodes which are polyphase in nature. The type of folds recognized are ptygmatic, asymmetrical, tight, and isoclinal to overturned antiformal folds. Other structures observed arose from brittle to ductile deformational events. However, the studied areas are enriched with gemstone mineralization such as garnets, blue and green tourmalines, and other specialty minerals which are hosted by the granite pegmatites in the study area. Gemstones are minerals, rocks, or organic matter that have been chosen for their beauty, durability, and rarity and are cut, faceted and polished to make jewelry or other human addornments This research also confirmed that the structural differentiation of the rocks in the studied area has contributed immensely to the ground preparation for the epigenetic mineralization (gemstones and other specialty minerals) discovered and mapped in the studied area.

Keywords: Lithologic Units, Structures, Deformation, Mineralization

1. Introduction

Gemstones are minerals, rocks, or organic matter that have been chosen for their beauty, durability, and rarity and are cut or faceted and polished to make jewelry or other human addornments. Gemstones are also known as mineral crystals of precious stones found underneath the earth. They are naturally formed as minerals or substances of beauty when cut and polished for jewelry and partly as alternative and complimentary medicine in prehistoric times (Adesoji and Stephanie, 2018). They are hosted by pegmatites especially the complex ones which normally exhibit zoning. In addition, there are many others for example, diamonds are hosted in volcanic rocks such as kimberlites and lamproites. These pegmatites are specialized types of rocks that occurred as late stage intrusive rocks (magmatic differentiates) London (2008); Simmons et al. (2012).

They intrude pre-existing rocks such as granites, migmatites, gneisses, schists etc in southwestern Nigeria. They are widely distributed in Precambrian terrains such as those in Southwestern Nigeria and Ekiti State in particular. The Precambrian Basement of Southwestern Nigeria has undergone several episodes of deformation and metamorphism Rahaman (1988). The general north-south trend of major fractures and foliations within the Basement complex occured as a result of deformation Odeyemi (1992). Odeyemi (1977) observed that the rocks in the basement complex of Nigeria display polyphase deformation with the plutonic episode of the Pan African Orogeny being the most evident. Rahman (1988) also noted that south western basement complex of Nigeria lies within the rest of the Precambrian rocks in Nigeria. He grouped the rocks in this region as migmatite – gneiss – quartzite complex comprised largely of sedimentary series with associated minor igneous rock intrusions which have been altered by metamorphic, migmatitic and granitic processes. Oluyide (1988) suggested that almost all the foliation exhibited by rocks of southwestern Nigeria excluding the intrusive are tectonic in origin, because pre-existing primary structures have been obliterated by subsequent deformation. Anifowose et al. (2006) also noted that joints ranging from minor to major ones are found in all the rock types, some of which are filled with quartz, feldspars or a combination of both which allign generally in the NE-SW direction, In addition, (Ajibade, 1986 and Rahman, 1988) suggested that the south western basement complex of Nigeria has been affected by two phases of deformation namely D1, D2. The first phase (D1) produced tight to isoclinals folds while the second phase (D2) is characterized

* Corresponding author e-mail: osayodele@futa.edu.ng; samuelayodeleolusiji@yahoo.com

by more open folds of variable style and large vertical NNE-SSW trending fault. Also, Oluyide (1988) gave evidence that within the basement complex, tectonic deformation has completely obliterated primary structures except in a few places where they survived deformation. Okonkwo (1992).. Adesoji and Stephanie (2018) examined each stage of the gemstone value chain, issues, and opportunities that abide in each stage as well as current future status each stage has in the economy of Nigeria. Nigeria is known to have over forty-four deposits of different solid minerals including gemstones in large quantity, and the sector contributes less than 0.3% to the Gross Domestic Product (GDP) of the nation. Leviski and Sims (1997) investigated the feasibility of surface geochemical techniques applied to exploration for coloured gemstones in the MAngare area, SE Kenya, and concluded that the most cost-effective approach would involve bulk-sampling over a loose grid to define ultramafic belts. Geological mapping has been carried out in the Erijiyan axis (northern segment) to map the quartzites and the quartz-schists (Ayodele and Ajigo, 2019); however, there is paucity of information or no information at all on the nature and type of pegmatite bodies in Ikogosi and its environment which is assumed to be mineralized. Therefore, this research is aimed at carrying out detailed geological mapping and prospecting of gemstones in the deformed Precambrian rocks of the study area.

2. Description of the Study Area

The study area covering Ikogosi, Ogotun, Apapolu, Erijiyan, Araromi, Ipole and Igbara-Odo, all in Ekiti Southwest local government area, is situated in the eastern part of Okemesi Fold Belt (Figure 1). It lies within longitudes +4°57'0" and +5°5'0" and latitudes +7°31'0" and +7°37'0", covering an estimated area of 48km². The study area is accessible through a major road network and footpaths.

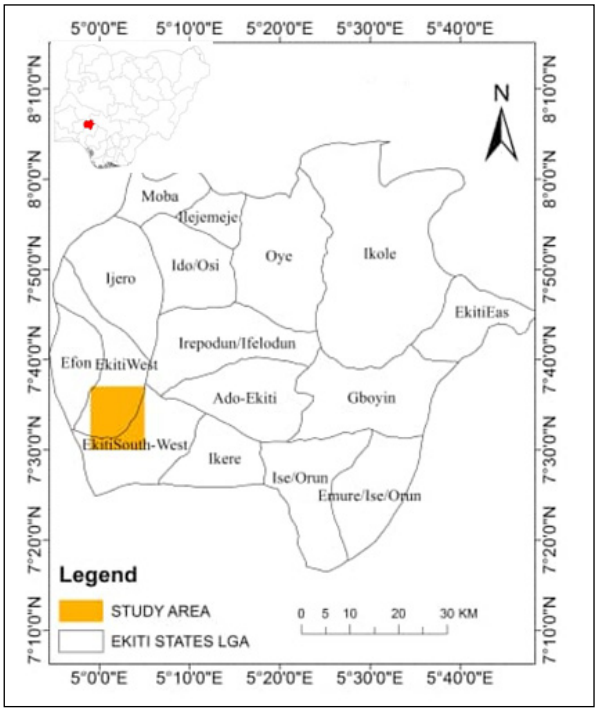

Figure 1. Map showing location of the study area. (Oyewumi, 2019)

Traversing the area was also made easy with the assistance of the local settlers who helped locate existing outcrops in initially inaccessible areas. Stream channels were also useful indicators.

The topographic map provided represents the entire study area (Figure 2) which also serves as the base map. The uneven topography is caused by the crystalline nature of the different rocks found in the area and their differential responses to weathering. The highest topographic height encountered was about 1800m above the average sea level. The study area is also characterized by relatively dense drainage which is of dendritic and trellis patterns.

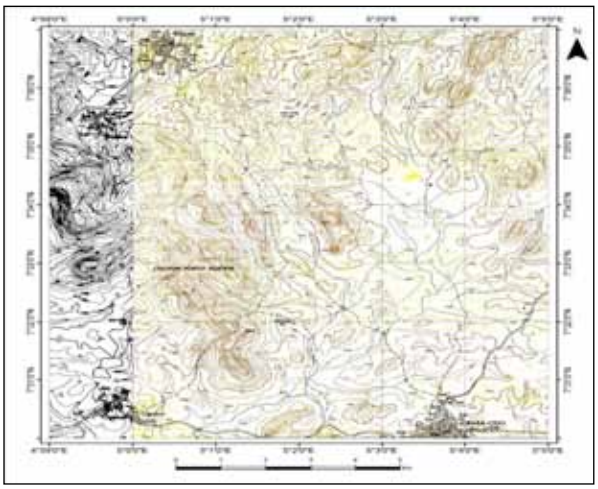

Figure 2. Topographic Map of the study area (Modified after NGSA, 2006)

3. Methods of Investigation

Geological mapping was carried out with the aid of the topographic (base) map of the study areas acquired at a scale of 1:25,000 (Figure 2). The rocks encountered in the area include quartzites (massive and schistose), migmatite-gneiss, granites, granite-gneiss and pegmatites which intruded majorly on the quartzites, granites and granite-gneisses as dykes and veins. Their accurate geographical positions were determined with the global positioning systems (GPS), and were recorded in the field notebook. The rocks were systematically sampled across the various locations and localities. The various sampling points were superimposed on the geology (Figure 3) to give a clearer synopsis of the terrain. Structures such as folds, fractures, joints were also mapped on the different rocks, and their orientations and atitudes were measured using the Compass clinometer. Fifty-two (52) bulk samples were collected for these investigation. The petrographic studies were carried out using the Binocular Polarizing Microscope with Toupcam Digital Camera (3.1MP), and Computer.

The laboratory analysis was carried out at the Petrology laboratory of the Department of Applied Geology, The Federal University of Technology, Akure. Twenty-two rock samples were carefully selected, and cut into thin sections using manual thin-section method, and were prepared as rock slides with necessary materials and reagents using the standard procedures and techniques.

Microscopic viewing with the aid of Topcam digital camera (3.1MP) under transmitted light was carried out to detect and study the mineral composition of the rocks. The purpose of the camera is to take snapshots of the slides, and produce the photomicrographs of the different slides, while analysis and identification have been carried out on the desktop computer attached to the camera to bring out the optical behavior and character of these minerals under plane polarized and crossed polarized light.

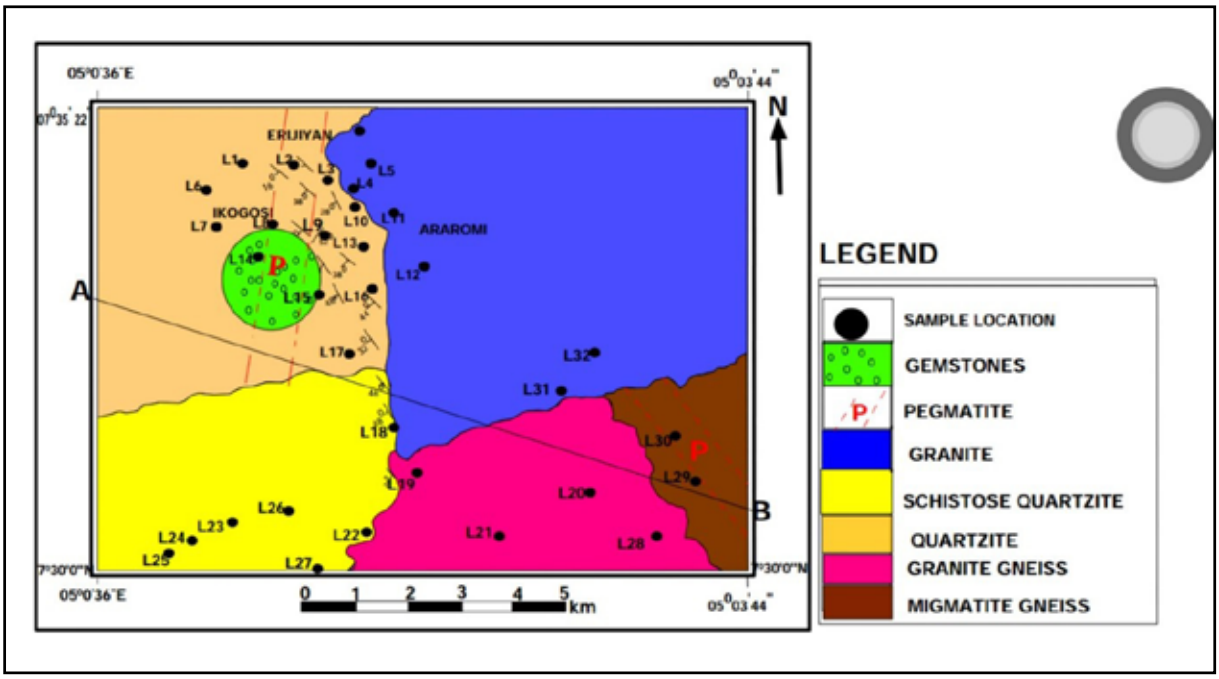

Figure 3. Sample location map of the study area superimposed on the geology.

4. Results and Discussion

4.1 Field Investigation

The geological map (Figure 4) presents the various rock units and their distribution patterns in the study area. Six major lithologic units were identified which includes the granite-gneiss to the pegmatite with well-delineated boundaries. Table 1 presents the geological field data collected which represented data from two different localities. The strike and dips were not measurd in most of the rocks because they were not foliated, some of the fabrics have been destroyed due to deformation while others have been intensely weathered occurring as boulders around the study areas (Table 1). The pegmatites are the late-stage intrusives occurring as dykes and veins on the pre-existing rocks which are products of the Pan African orogeny (Figure 4).

The cross-sectional maps confirmed folding in the study area. However, migmatite is absent from other areas because it was confined to certain locations and is not extensive like other outcrops as seen in Figure 5. In addition, some of the grantic bodies possess inclusions (xenolths) which are evidences of partial digestion of the intruding rocks. The folding episodes affected the schistose quartzites, granite gneiss, and the granite. This can be attributed to the compressive tectonics accompanying the behaviour and responses of the affected rocks to stress. (Figure 5). This also confirmed that fracturing postdated the folding episodes in the studied area. The various rock types mapped and their delineated boundaries and dipping angles were used to produce a geological and cross-sectional maps of the studied area (Figures 4 and 5).

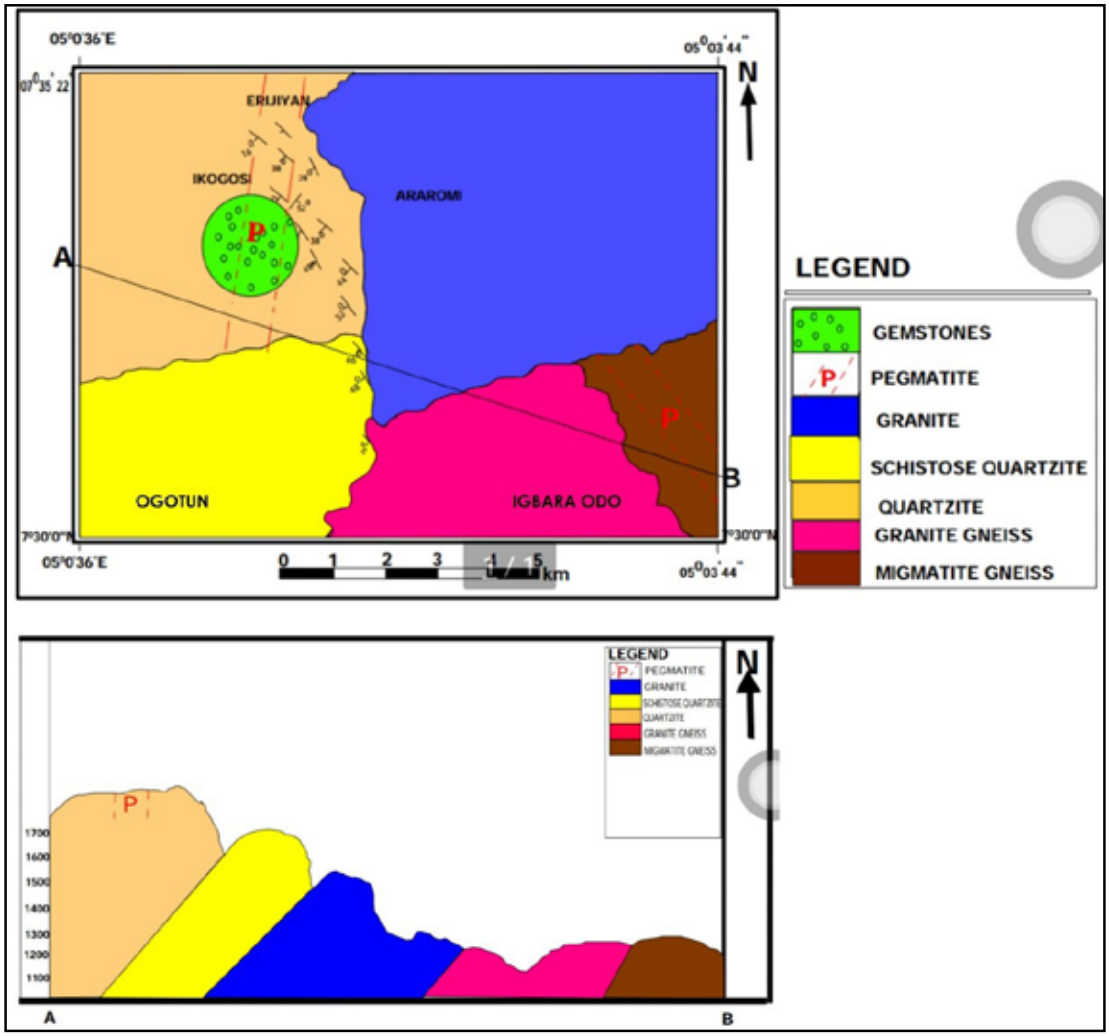

Figure 5. A cross section of symetrical fold profile generated from dip matching from other locations.

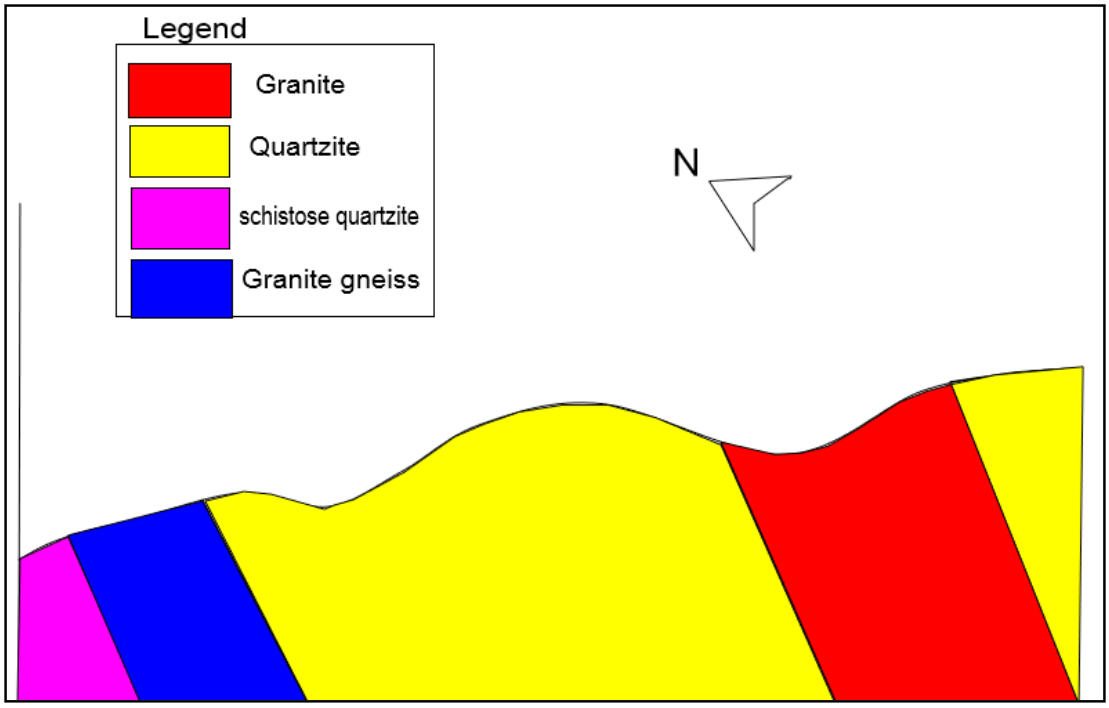

Figure 4. Geological map (above) and cross-section (below) of the study area.

Table 1. Summary of Field Data

Location	Latitude	Longitude	Rock Names	Strike and dip measurements	Joint and fractures orientations	Rock types
1	N 07^0 35’ 22’’	E 05^0 0’ 36’’	Schistose Quartzite	284^0 W, 30^0 E	Weathered	Metamorphic
2	N 07^0 35’ 22’’	E 05^0 0’ 38’’	Quartzite	-	Weathered	Metamorphic
3	N 07^0 35’ 10’’	E 05^0 0’ 53’’	Mine site for tourmaline; Quartzite with pegmatite intrusion.	-	Mining pit	Metamorphic
4	N 07^0 35’ 00’’	E 05^0 1’ 14’’	Quartzite	-	Weathered	Metamorphic
5	N 07^0 34’ 58’’	E 05^0 1’ 15’’	Quartzite	341^0 NW, 75^0W	Weathered	Metamorphic
6	N 07^0 34’ 43’’	E 05^0 1’ 16’’	Quartzite	-	Weathered	Metamorphic
7	N 07^0 34’ 44’’	E 05^0 1’ 17’’	Quartzite	-	Weathered	Metamorphic
8A	N 07^0 30’ 07’’	E 05^0 2’ 42’’	Granite	-	Pegmatite Veins	Igneous
8B	N 07^0 30’ 07’’	E 05^0 2’ 41’’	Granite	-	Joints and folds	Igneous
8C	N 07^0 30’ 05’’	E 05^0 2’ 41’’	Granite	-	Joints and folds	Igneous
9	N 07^0 30’ 08’’	E 05^0 3’ 30’’	Granite	-	Xenoliths folds and fractures	Igneous
10	N 07^0 30’ 08’’	E 05^0 2’ 41’’	Granite	-	Joints and folds	Igneous
11	N 07^0 30’ 11’’	E 05^0 3’ 30’’	Granite	-	Joints and folds	Igneous
12	N 07^0 30’ 24’’	E 05^0 3’ 38’’	Granite	-	Joints and fractures	Igneous
13	N 07^0 30’ 35’’	E 05^0 3’ 44’’	Contact of Granite and Migmatite Gneiss		315^0 NW, 313^0 NW, 308^0 NW, 311^0 NW, 321^0 NW	Igneous and Metamorphic
14	N 07^0 30’ 36’’	E 05^0 3’ 41’’	Contact of Granite and Migmatite-Gneiss	-	332^0 NW, 314^0 NW, 318^0 NW, 117^0 SE, 264^0 SW, 132^0 SE	Igneous and Metamorphic
15	N 07^0 30’ 45’’	E 05^0 3’ 35’’	Granite	-	Xenolith	Igneous
16	N 07^0 36’ 09’’	E 04^0 59’ 55’’	Quartzite	-	Weathered	Metamorphic
17	N 07^0 36’ 47’’	E 05^0 0’ 25’’	Quartzite	-	Weathered	Metamorphic
18	N 07^0 36’ 49’’	E 05^0 0’ 25’’	Quartzite	-	Weathered	Metamorphic
19	N 07^0 36’ 50’’	E 05^0 0’ 39’’	Quartzite	-	Weathered	Metamorphic
20	N 07^0 36’ 38’’	E 05^0 0’ 39’’	Granite	-	184^0 SE, 342^0 NW	Igneous
21	N $07^0$35’20.6’’	E 05^0 0’40.5’’	Schistose Quartzite	342^0 NE 68^0 E	Weathered	Metamorphic
22	N 07^0 36’ 15’’	E 04^0 59’ 57’’	Quartzite	-	Weathered	Metamorphic
23	05^0 0 40.5’’E	$07^0$35’20.6’’N	Schistose Quartzite	342^0 NE	68^0 E	Schistocity
24	05^0 0’38.1’’E	$07^0$35’22.3’’N	Schistose Quartzite	156^0, 148^0 SE	60^0, 48^0 E	Schistocity

Table 1. continued

Location	Longitude	Latitude	Lithology	Strike	Dip	Texture	Structure
25	05^0 0’36’’E	$07^0$35’22’’N	Schistose Quartzite			Schistocity	Veins, Joints
26	05^0 0’37.9’’E	$07^0$35’21.7’’N	Schistose Quartzite			Schistocity	Joints
27	05^0 0’38.8’’E	$07^0$35’21.7’’N	Schistose Quartzite	352^0 NE	52^0 E	Schistocity	Veins, Folds
28	05^0 0’39.8’’E	$07^0$35’21.0’’N	Schistose Quartzite	354^0	60^0 W	Schistocity	Veins, foliation planes, folds
29	05^0 0’44’’E	$07^0$36’25’’N	Granite			Fine to medium grained	Veins, solution holes, exfoliation
30	04^0 58’47.1’’E	$07^0$35’19.0’’N	Schistose Quartzite			Schistocity	Foliation planes, joints, folds
31	04^0 58’29.5’’E	$07^0$35’30.9’’N	Schistose Quartzite	290^0, 291^0 NW	38^0, 48^0 W	Schistocity	Fractures
32	04^0 58’30’’E	$07^0$35’33’’N	Schistose Quartzite	232^0, 230^0 NW	20^0, 24^0 W	Schistocity	Fractures
33	04^0 58’26’’E	$07^0$35’34’’N	Schistose Quartzite			Schistocity	Fractures
34	04^0 58’06’’E	$07^0$35’39’’N	Schistose Quartzite	336^0, 322^0 NW	16^0, 16^0 W	Schistocity	Fractures
35	04^0 55’42.7’’E	$07^0$33’56.0’’N	Quartzite			Gritic	Joints
36	04^0 55’42.6’’E	$07^0$33’55.1’’N	Quartzite	NE-SW	E		Fractures
3|7	04^0 55’43.2’’E	$07^0$33’19.4’’N	Quartzite	320^0 NW	52^0 E	Sugary	Fractures
38	05^0 00’16’’E	$07^0$36’47’’N	Quartzite			Fine to medium grained	Veins, joints
39	04^0 59’57’’E	07^0 36’15’’N	Quartzite			Fine to medium grained	Veins, joints
40	05^0 00’35’’E	07^0 35’23’’N	Quartzite	178^0,174^0, 168^0, 171^0 SE	38^0, 42^0, 44^0, 46^0 E	Fine to medium grained	Veins, joints
41	04^0 55’41’’E	07^0 33’05’’N	Quartzite			Fine to medium grained	Joints
42	04^0 55’40’’E	07^0 33’09’’N	Quartzite			Fine to medium grained	Joints
43	04^0 57’21’’E	07^0 34’26’’N	Granite gneiss				
44	04^0 57’53’’E	07^0 33’56’’N	Granite gneiss				Joints, folds
45	04^0 57’49’’E	07^0 33’56’’N	Granite				Joints, folds
46	04^0 57’46’’E	07^0 34’05’’N	Granite				Joints, folds
47	$04^0$57’19’’E	07^0 34’25’’N					Xenolith, folds, fractures
48	$04^0$58’08’’E	07^0 34’37’’N	Quartzite				
49	$04^0$57’11’’E	07^0 34’37’’N	Quartzite				
50	$04^0$00’06’’E	07^0 36’30’’N	Quartzite				
51	$04^0$00’36’’E	07^0 35’22’’N	Quartzite				
52	05^0 0’53’’E	07^0 35’10’’N	Quartzite				

4.1.1 Granite-gneiss

This rock type was found mostly in contact with the granites and occurred as flat-lying rocks. They display quartz and pegmatite veins and conjugate fractures because the fractures are parallel to the foliation plane followed by another fracture sets at angle to the other. Pegmatite dykes were also seen on the outcrop. They represent the oldest rocks in the investigated locations. There are series of folding observed on the outcrop which are superimposed which is suggestive of different folding episodes. Other observable features are veins and joints. The texture of the granite-gneiss ranges between medium grained to coarse- grained. The observable minerals in the rocks are biotite, quartz, and orthoclase feldspar with no accessory minerals identified.

4.1.2 Quartzite

This is another major rock type in the study area, occupying relatively a large portion than granite. Two types of quartzites (massive and schistose) dominate the studied area. They were discovered in the north eastern to the central part of the area. The massive ones are dark to reddish brown in colour due to alteration and are volumetrically extensive. Some road cut outcrops mapped are highly weathered and show the presence of muscovite foliations and pegmatite veins. Folding occurred on these outcrops based on the dipping angles of their limbs in opposite directions (Table 1). Such folds include ptygmatic and recumbent folds. However, the schistose quartzite dominated a larger part of the studied area. They are intensely weathered and crumble easily and are to be found in the North eastern part on the map. The quartzite is buried beside a farmland making it very difficult to see, but their presence is recognized by the quartz rubble seen along footpaths and ridges. It was highly weathered, and there were no observable features. Schistose quartzites occur as low-lying beside the road. The rock is highly weathered, though the foliation planes are still clearly observable. The dip directions of the outcrop suggest multiple folding episodes followed by numerous pegmatite intrusions occurring as veins.

4.1.3 Granites

Granites are the second most dominant rock type in the area. They are fine-grained, low-lying outcrops with fractures and joints. They occur in the form of dislodged boulders. They contain a dark brown colored weathered surface and minerals such as quartz, feldspar, and biotite. In addition, they consist of quartz and pegmatite veins with xenoliths showing relics of the oldest rock. The accessory minerals in the granites are zircon and Fe-oxides (such as magnetite).

4.1.4 Migmatite-gneiss

These were discovered in the western part of the study area, and occur as a low-lying outcrop and are extensive. Migmatite-gneiss is medium-grained with mineralogical banding of quartz, biotite and feldspar. It is the contact rock with the granite; structures mapped include a pegmatite intrusion in the form of veins, ptygmatic and chevron folds with fractures and solution holes.

4.1.5 Pegmatite

These are late stage intrusions in the studied area mostly as veins and not as massive as other rocks. In terms of their nature, both simple and complex types are present in the studied area. However, field observations revealed that complex pegmatite dominated areas outside the designated locations. This paved the way to extending sampling to abandoned pits and active mining sites; samples recovered from these sites revealed that the actual mining of gemstones is confined to certain locations where complex pegmatites are found. Remnants collected from these sites showed that they contain blue and green tourmaline, feldspar, and garnet.

Figure 6. (a and b) Granitic and migmatitic gneisses displaying gneissocity; (c and d) Hand specimen tourmaline inclusion in quartzite; (e and f) folded intrusive quartzo-feldspathic bodies on granite; (g and h) Occurrence and mining pit for tourmaline.

4.2. Laboratory Investigation

Petrographic investigations of the various rock units in the locations revealed the following rock forming minerals: biotite mica, muscovite mica, plagioclase feldspar, hornblende, microcline feldspar, (locations 1 and 2), quartz (showing angular shape), and opaque minerals such as iron oxide. The distribution of the different minerals is presented in Table 2. The photomicrographs of the different rocks are shown in slides Figures 6 a, b, and c. Observations were made under plane polarized light (PPL) and crossed polarized light (XPL). They displayed diagnostic minerals present in each slides. Generally, the minerals identified are typical of the major rock forming minerals such as quartz, feldspar (plagioclase, orthoclase and microcline), hornblende,

muscovite etc. Only locations Ik1, Ik2, and Ik3 slides have tourmaline and garneti-ferous minerals such as grossularite and almandine because the rocks in these areas are intruded by complex pegmatites. Petrographic studies of thin sections also revealed the distribution of minerals in the rocks (Table 2). It is observed that quartz is the most dominant mineral followed by biotite and muscovite, microcline, and other minerals which suggest that quartzite is the most prevalent rock in the study area.

Table 2. Mineral Assemblages of the Studied Samples for Rocks

Slide Number	Mineral(s)	Rock Name
L1	Muscovite Microcline Feldspar Quartz	Weathered Gneiss
L2	Quartz	Quartzite
L3	Quartz	Quartzite
L5	Quartz, Muscovite	Quartz-Mica Schist
L6	Quartz	Quartzite
L7	Biotite Opaque Mineral Muscovite Plagioclase	Biotite Schist
L8	Biotite Quartz Plagioclase	Granitic Gneiss
L8A	Biotite, Hornblende, Muscovite, Microcline, Feldspar, Quartz	Fine Grained Granite
L9	Biotite, Muscovite, Microcline Feldspar, Quartz	Gneiss
L13A	Biotite, Plagioclase, Quartz	Granite
IK1	Quartz, Tourmaline, garnets	Quartzite
IK2	Quartz, Tourmaline, garnets	Quartzite
IK3	Quartz, Tourmaline, Garnets	Complex Pegmatite
IK4	Quartz Muscovite	Weathered Quartz-Mica Schist
IK5	Quartz	Quartzite
IK6	Quartz	Quartzite
IK7	Quartz Muscovite	Quartzite
IK8	Quartz	Quartzite
IK9	Quartz	Quartzite
IK10	Muscovite, Quartz	Quartzite
IK13	Biotite, Muscovite, Quartz, Microcline, Feldspar	Weathered Granitic Gneiss

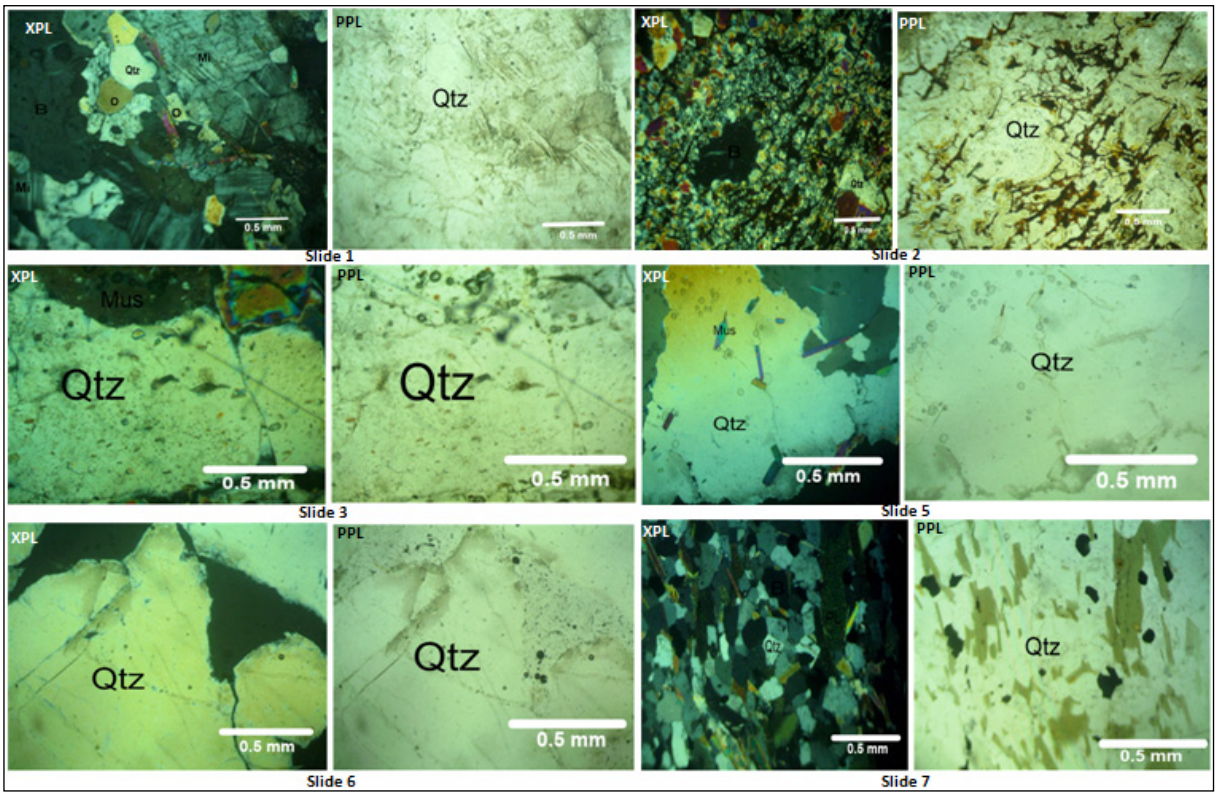

Figure 7. a. Photomicrographs from thin section of selected rock samples under PPL and XPL

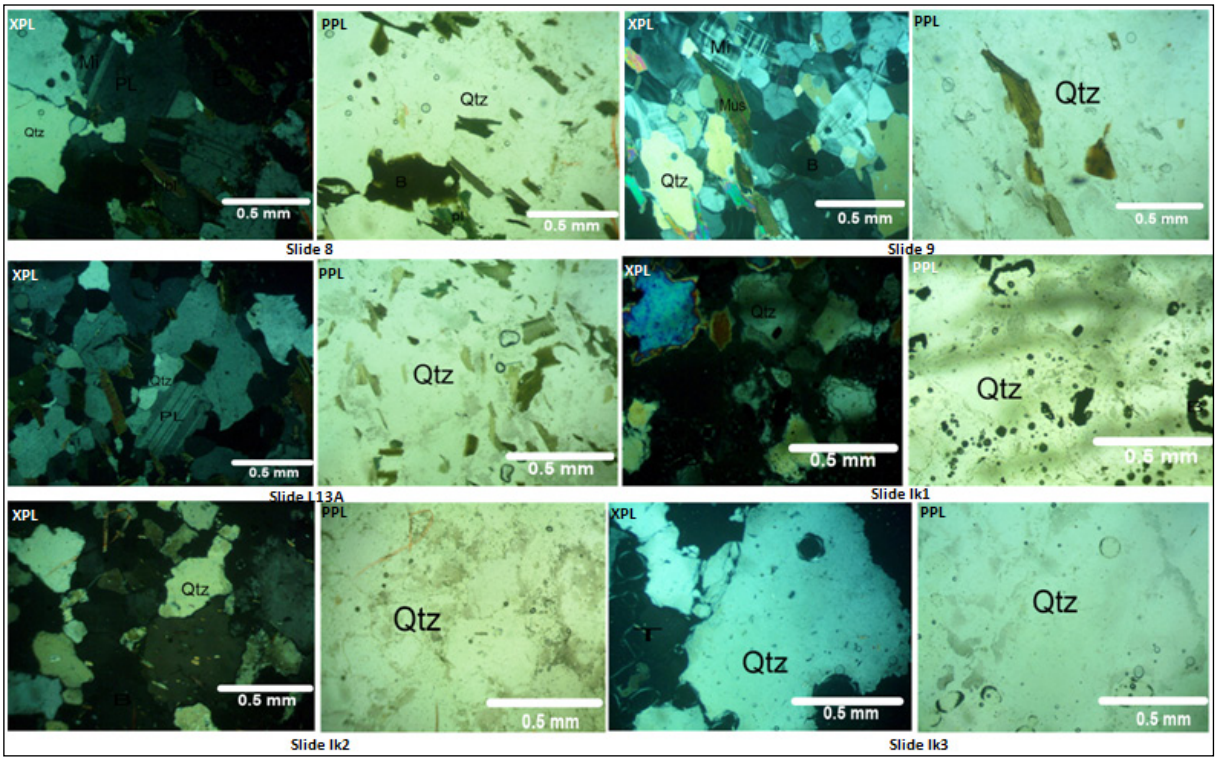

Figure 7. b. Photomicrographs from thin sections of selected rock samples under PPL and XPL

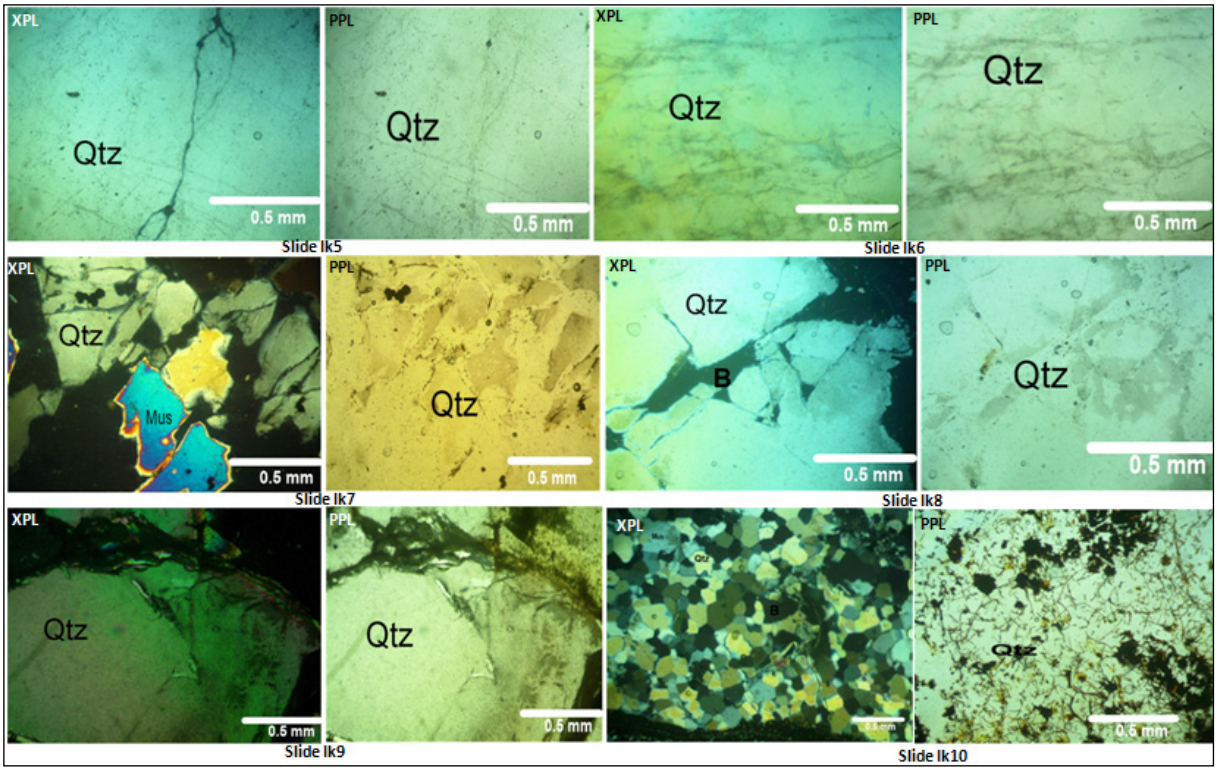

Figure 7. c. Photomicrographs from thin sections of selected rock samples under PPL and XPL

Microcline – Mi; Quartz- Qtz; Muscovite – Mus; Hornblende – Hbl; Orthoclase – O; Biotite – B; Tourmaline – T; Gt- garnets; MC- Mineral composition, XPL- Crossed Polarized light, PPL- Plane polarized light

4.3. Structural Analysis of the Study Area

Most of the basement complex rocks of Nigeria have been affected by polyphase deformation which has led to the re-orientation of the initial structural grain of the basement complex (Oluyide, 1988). These deformations left their imprints on the rocks affected which can be used to re-write the geological history of those rocks. Most of the quartzites and granites and gneisses in Nigeria have been affected by several orogenies; the latest being the Pan African orogeny 600±150 Ma (Burke and Dewey, 1972; Dada, 2006) resulting in the formation of structural features such as fold, fractures, and joints. Structural elements such as veins, fractures, folds, foliations, and faults were observed and mapped in the rocks of the study area. The structures occurred mainly in all rock types, but most prominently in the granite-gneiss. From the analysis of structural data collected, it can be inferred that at least three major orogenic cycles of deformation, metamorphism, and remobilization have affected the area followed by a last stage of tectonic jointing and faulting which led to the formation of the fractures and veins in the gneisses.

The outcrops of gneissic origin and the schistose quartzites exhibit folded surfaces from tight, ptygmatic and isoclinal folds to recumbent and overturn antiformal folds as revealed from field observations and measurements (Figure 9). In some of the outcrops mapped, it was observed that some of these folds are older than the joints that cut across, and some folds are younger than the fractures which also confirmed the three episodes of tectonic deformation proposed earlier. Most of the folds observed are composite, asymmetrical, parasitic, and isoclinal folds. These could be attributed to a series of deformation and several metamorphic episodes that have pervaded the studied area which led to successive restructuring of the inherent minerals in the rocks. In the process of the deformation and metamorphism, minerals which could not withstand the heat of metamorphism became decomposed or converted to less stable minerals, while others were resistant to the heat and deformation, thereby, forming secondary minerals or being altered to clay bodies or form a coat on other minerals. It could be inferred that the gneiss outcrops have been affected by three episodes of deformation denoted as D1, D2, and D3. The D1 deformation produces tight to isoclinals and asymmetrical folds. The second D2 phase produces ptygmatic and disharmonic folds, this is characterized by steep to moderately-inclined axial planes. Finally, the third D3 deformation produces refolded folds which are superimposed on the ptygmatic fold (Figure 6f).

Several fracture orientations were obtained from the rocks at different locations in the field, and their measurements were used to produce a rose diagram which indicated that the direction of the tectonic force is in the NW-SE. These fractures were clearly displayed and observed on the schistose quartzite, granite-gneiss and on most quartzite materials. However, some fractures are linked with mineralization especially the NW-SE, NE-SW, E-W, NNS and N-S fractures Wright, (1976). The granitic rocks are synonymous with N-S fractures and are mostly interconnected. Quartzites are commonly associated with E-W fractures known for gold mineralization Anifowose et al. (2006), while the schists and gneisses have paucity of fractures due to their ductile nature.

Joints are present in nearly all rock surfaces and are generally more toward the vertical than the horizontal. The most prevalent causes of jointing are tensional and shearing stress forces set up by crustal movement within the earth's crust. Although, they can occur individually, they most frequently occur as joint sets and systems. In some folded rocks, the joints that lie at the right angles to the fold hinges are known as cross joints. The joint orientations gathered on the field were used in plotting rose diagrams for the joint sets (Figure 8). Joints were mostly observed on the granitic gneiss outcrop. The veins present in the study area are majorly of pegmatite, quartz, and quartzo-feldspathic composition which are commonly associated with the gneiss unit as late intrusions (Anifowose et al. (2006). They are also can be continuous or discontinuous. Some of the veins are mutually cross-cutting each other; they are sometimes absent in individual outcrops. Quartz veins are most abundant. A majority of the veins are concordant to the trend of foliation of the rock in which they occur. Some are crosscutting and do not follow the general trend of the outcrops. On some outcrops, the direction of some veins cannot be easily deduced because of the fact that the rocks in which they form has undergone deformation, hence distorting the rocks' foliation and fabric and also the orientation of the veins present. However, it should be noted that a large percentage of all the veins are in the same direction as the general trend of foliation of the rocks on which they exist. The boundary between the veins and the rocks are sharp, though there are few exceptions on some of the rocks where the boundaries between the rocks and the veins are gradational. Some of the veins are very long, extending up to 15m throughout the length of the outcrops on which they occur, while some of them are short extending only a few centimeters. Also, some are relatively wide and some are thin. Most of the veins were formed after the rock was formed. While a few of them were segregated during the cooling of the rock. The formation of most of the concordant and discordant quartz veins are associated with the late faulting and fracturing in the area (Gandu et al., 1986). The foliation planes which are pervasive planar surfaces within a rock are well-developed in the gneisses, but due to extensive weathering conditions in the area, there is limited foliation surfaces for the measurement of strike and dip. However, strike and dip values were recorded at points of good foliation planes. The general dip direction is towards the east and is also slightly dipping to the west (Table 1). The strike direction is slightly varying depending on the position in the area. These structures are only observed as gneissosity and foliation in the shear zones of gneissic outcrops. This foliation appears to be the result of the pervasive parallel arrangement of the platy minerals in the studied rocks.

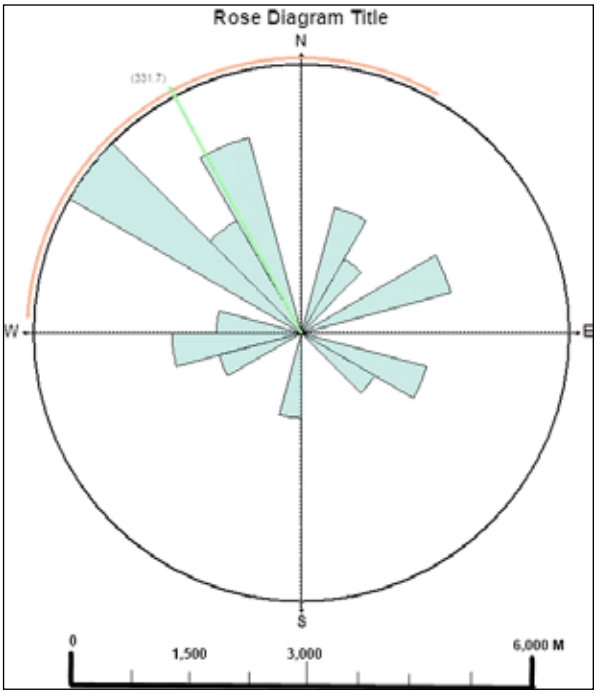

Figure 8. Rose diagrams plotted from joint orientations measured in the field.

Figure 8. Different generations of veins and folds as observed on the gneissic rocks of the study area

4.4. Gemstone Prospectng

Gemstones are formed in different geological environments in the earth, resulting in various types of deposits including magmatic, pneumatolytic, metamorphic, sedimentary (alluvial), hydrothermal, pegmatites, and greissen gems. For the formation of each kind of gem, a specific, and unique combination of five factors are required in their respective environments. These are: temperature, pressure, space, chemical elements, and time. In other words, gems are, in general, rare, but some are rarer than others (Nyako et al., 2014). For example, silicon and oxygen are the two most abundant elements of the earth's crust and the conditions for the formation of quartz (SiO2) are relatively common so it is understandable that quartz is found widely, while Axinite on the other hand, which is also a silicate gem requires (in addition to silicon and Oxygen) Ca, Fe, Mg, B, and Al for its formation, which makes such a gem considerably rarer than quartz, (Abaa, 1990). These rare conditions in cracks, fractures, faults, and shear zones where gemstones are formed which makes the latter very rare to find, and therefore quite precious. They are used for ornamentation and as jewelleries when cut and polished. Some traditions are connected with sentiments, beliefs, and superstitions associated with gems, to the effect that some gems carry the power of driving out evil spirits and providing all sorts of luck or fortune, (Aga and Ashano, 2008).

Geological exploration for gemstones and other specialty minerals was carried out in the study areas as part of the investigation. There are two types of pegmatite mapped in the locations which are the mineralized and non-mineralized types. The mineralized types are often the targets of local and artisan miners in the studied area because of the gemstones and other specialty minerals found in them. Many pits and mine sites were discovered in the process of mapping and traversing and as a result of this, sampling was extended beyond the initial locations to ensure wider coverage. This led to the discovery of the location of gemstone sites hosted by the quartzites and quartz schists intruded by the complex pegmatites. The coordinates of this location are (7^0 35' 10''N, 5^0 00 53''E). This location revealed the actual site of gemstones and other allied minerals in the study area which are promising sites for further exploration (Figure 4). The samples picked contain blue and green tourmaline crystals. On the contrary, the cadastral already acquired for gemstone prospecting is not economically viable for its intended purpose for the following reasons: (i) The rocks are entirely weathered and have turned into clay (ii) The underlying rocks are extremely fractured which enables water to gush out (iii) The sites has undergone intense deformation which affected the rocks and their fabric.

5. Conclusions

The study area forms part of the Precambrian basement complex of southwestern Nigeria that has been affected by multiple episodes of deformation. However, geological mapping and assessment of the rocks in the study area revealed various levels and phases of deformation. The various phases of these deformational events can be detected by the dipping angles of the rocks, orientations of the fractures and joints, and evidence of migmitization and granitization and gneissocity observed on the outcrops. Since the study area is located east of Okemesi fold belt, there are similarities regarding the rock types and folding patterns/ episodes to the belt with the limbs dipping in the same direction in some places and to the opposite direction in other places suggesting the superimposition of refolded folds on the earlier folded phases depicting polyphase patterns of deformation. Also, the search for gemstones has been made possible due to the ground preparation culminating to structural differentiation of the host rocks that provided pathways for the permeation of the mineralizing fluids and its eventual solidification. The type of gemstones discovered in the studied area are the blue and green types (aquamarine and Turquoise) and the blue and red tourmaline crystals.

However, research in the study area is still ongoing. We believe that further research will provide information on the gemstone type, minerals (name and composition), physical and optical features including colour, sizez, habits (purity, companion phases), mode of occurrence, and scale of deposit. In addition, the effects of tropical weathering accelerated by high humidity have altered most of the rocks into in-situ clay deposits and boulders. it is therefore impossible to carry out geochemical exploration in the studied areas; however, the petrographic study revealed the presence of some of the major rock-forming minerals such as quartz, feldspar, micas, and opaque minerals such as iron oxides etc. The rocks of the study area are fairly suitable for quarry activities.

Aknowledgements

I hereby acknowledge the efforts of Oyewumi Olusola, Omotoso Ayo Mike who are my project students and also served as technical partners on the field. Your immeasurable contribution to this project is highly commendable. I am grateful to the laboratory technologists of the Department of Applied Geology, The Federal University of Technology, Akure who assisted in the sample preparations for microscopic study. Also, I am grateful to the Chief Technologist in person of Mr, O.F Oladeji for his assistance in the laboratory also. I am highly indebted to the Deputy Chief Technologist in person of Mr. Mark, who devoted his valuable time to viewing the slides under the Petrological Microscope together with me. Thank you all.

References

Abaa, SI. (1990). Hydrothermal fluids responsible for the formation of precious minerals in the Nigerian Younger Granite Province. Mineralium Deposita 26: 34–39. https://doi.org/10.1007/BF00202362.

Adesoji, A. and Stephanie, H. (2018). Understanding the gemstone path and value chain in Nigeria. Journal of Scientific Research and Studies 5(7): 175-185.

Aga, T., and Ashano, EC. (2008). Enhancing the Value of Nigerian Gems through Lapidaries. Continental Journal of Earth Sciences 3:71 – 76.

Ajibade, AC. (1986). The Origin of Older granites in Nigeria. Some evidences from Zungeru region, Nigeria. Journal of Mining and Geology pp. 223-230.

Ayodele O.S, and Ajigo I.O. (2019). Reconnaissance geological and geochemical studies of the Precambrian Rocks in Erijiyan Area, Southwestern Nigeria. Implications for Mineral

Exploration. Global Journal of Earth and Environmental Sciences 4(1): 1-13. Geological Survey of Nigeria, 2006

Anifowose, A.Y.B, Odeyemi, I.B, Borode, A.M. (2006). The tectonic significance of the Ifewara- Zungeru Megalinear in Nigeria. Proceedings of the 1st International Workshop on Geodesy and Geodynamics, Centre for Geodesy and Geodynamics, Toro, Bauchi State, Nigeria.

Burke K.C., and Dewey J.F. (1972). Orogeny in Africa. In: Dessauvagie, T.F.J and Whiteman, A.J. (Eds.), African Geology-University of Ibadan, 1970, pp. 583-608.

Dada SS. (2006). Crust forming ages and Proterozoic crustal evolution in Nigeria. A re appraisal of current interpretations. Precambrian Research 8: 65-74.

Gandu A.H, Ojo S.B, Ajakaye D.E. (1986). A gravity study of the Precambrian in the Malufashi area of Kaduna State, Nigeria. Tectonophysics 126: 181-194.

NGSA (2006). Topographic Map Ado Ekiti SW Map Sheet 244.

Leviski, AG., and Sims, DH. (1997). Surface geochemical techniques in Gemstone exploration at the Rockland Ruby Mine, Mangare area, SE Kenya. Journal of Geochemical Exploration 59 (2): 87-98. https://doi.org/10.1016/S0375-6742(97)00009-5

London, D., (2008). Pegmatites. Canadian Mineralogist Special Publication 10, 347pp

Nyako AA, Ajigo IO, Ashano EC. (2014): Trace elements as pathfinders for gemstone deposits: a case study of Jarawa and eastern part of Shere Complex, North Central Nigeria. International Journal of Research in Earth and Environmental Sciences 1(3): 21-36.

Odeyemi I.B. (1977). On the Petrology of the basement rocks around Igarra, Bendel State, Nigeria. Unpublished Ph.D Thesis, University of Ibadan, Nigeria. 233pp.

Odeyemi, I.B. (1992). The Ifewara fault in Southwestern Nigeria, its relationship to fracture zone and seismicity along the Nigerian coast, Kluver Academic Publishers, Dordrecht, Netherlands

Okonkwo, CT. (1992). Structural geology of basement rocks of Jebba area, Nigeria. Journal of Mining and Geology 31 (1): 53-62.

Oluyide P.O. (1988). Structural Trends in the Nigerian Basement Complex. In: Oluyide, P.O, Mbonu, W.C, Ogezi, A.E., Egbuniwe, I.G, Ajibade, A.C. Umeji, A.C. (Eds.), Precambrian Geology of Nigeria, Geological Survey of Nigeria, Kaduna. pp. 93-98

Oyawoye, Mosobalaje Olaloye (1959) The petrology of the older granites around Bauchi, Nigeria, Durham theses, Durham University. Available at Durham E-Theses Online: http://etheses.dur.ac.uk/7220

Oyewumi, O.E., (2019). Geological Characterization of the Basement Rocks in Ikogosi and Igbara-Odo Areas, Southwestern Nigeria. Unpublished B.Sc Thesis, The Federal University of Technology Akure, Nigeria. 67pp.

Simmons, W.B., Pezzota F., Shigley, J.E., Beurlen H., (2012). Granitic pegmatites as sources of coloured gemstones, Elements V. 8, P.281-287.

Rahaman M.A. (1988). Recent Advances in the study of the basement complex of Nigeria. In: Precambrian Geology of Nigeria. Geological Survey of Nigeria. 11-43.

Wright J.B. (1976). Fracture systems in Nigeria and initiation of fracture zones in the South Atlantic. Tectonophysics. 34:143-147.

المملكة الأردنية الهاشمية

صندوق دعم البحث العلمي

الجامعة الهاشمية

المجلة الأردنية
لعلوم الأرض والبيئة

JJEES

مجلة علمية عالمية محكمة

المجلد (١١) العدد (٤)

http:// jjees.hu.edu.jo/

ISSN 1995-6681

المجلة الأردنية لعلوم الأرض والبيئة

مجلة علمية عالمية محكمة

المجلة الأردنية لعلوم الأرض والبيئة: مجلة علمية عالمية محكمة ومفهرسة ومصنفة، تصدر عن عمادة البحث العلمي في الجامعة الهاشمية وبدعم من صندوق البحث العلمي - وزارة التعليم العالي والبحث العلمي، الأردن.

ترسل البحوث إلكترونيا إلى البريد الإلكتروني التالي:

رئيس تحرير المجلة الأردنية لعلوم الأرض والبيئة
jjees@hu.edu.jo

لمزيد من المعلومات والأعداد السابقة يرجى زيارة موقع المجلة على شبكة الانترنت على الرابط التالي:
www.jjees.hu.edu.jo

المملكة الأردنية الهاشمية صندوق دعم البحث العلمي الجامعة الهاشمية

JJEES

المجلة الأردنية لعلوم الأرض والبيئة

المجلد (11) العدد (4)

مجلة علمية عالمية محكمة تصدر بدعم من صندوق دعم البحث العلمي

ISSN 1995-6681 jjees.hu.edu.jo كانون الأول 2020